Masterarbeit

Estimating global warming from anthropogenic heat emissions - conceptual and numerical modelling approaches

von

Peter Steiglechner

im StudiengangMaster of Science (M.Sc.) Physik
der UniversitätPotsdam

02.10.2018

Erstgutachter:	Dr. rer. nat. habil. Georg Feulner
Zweitgutachterin:	Dr. Maria A. Martin
Zeitraum:	Oktober 2017 – Oktober 2018

Institut für Physik und Astronomie Universität Potsdam	Erdsystemanalyse – Forschungsbereich 1 Potsdam-Institut für Klimafolgenforschung (PIK)

Abstract

The forcing from the anthropogenic heat flux (AHF), i.e. the dissipation of primary energy consumed by the human civilisation, produces a direct climate warming.

Today, the globally averaged AHF is negligibly small compared to the indirect forcing from greenhouse gas emissions. Locally or regionally, though, it has a significant impact. Historical observations show a constant exponential growth of worldwide energy production. A continuation of this trend might be fueled or even amplified by the exploration of new carbon-free energy sources like fusion power. In such a scenario, the impacts of the AHF become a relevant factor for anthropogenic post-greenhouse gas climate change on the global scale, as well.

This master thesis aims at estimating the climate impacts of such a growing AHF forcing. In the first part of this work, the AHF is built into simple and conceptual, zero- and one-dimensional Energy Balance Models (EBMs), providing quick order of magnitude estimations of the temperature impact. In the one-dimensional EBM, the ice-albedo feedback from enhanced ice melting due to the AHF increases the temperature impact significantly compared to the zero-dimensional EBM.

Additionally, the forcing is built into a climate model of intermediate complexity, CLIMBER-3α. This allows for the investigation of the effect of localised AHF and gives further insights into the impact of the AHF on processes like the ocean heat uptake, sea ice and snow pattern changes and the ocean circulation.

The global mean temperature response from the AHF today is of the order of $0.010 - 0.016\,\mathrm{K}$ in all reasonable model configurations tested. A transient tenfold increase of this forcing heats up the Earth System additionally by roughly $0.1 - 0.2\,\mathrm{K}$ in the presented models. Further growth can also affect the tipping probability of certain climate elements.

Most renewable energy sources do not or only partially contribute to the AHF forcing as the energy from these sources dissipates anyway. Hence, the transition to a (carbon-free) renewable energy mix, which, in particular, does not rely on nuclear power, eliminates the local and global climate impacts from the increasing AHF forcing, independent of the growth of energy production.

Deutsche Zusammenfassung

Das Forcing durch die Emission von anthropogener Abwärme (AHF), d.h. die Dissipation von konsumierter Primärenergie, stellt eine Beitrag zu einer direkten Klimaerwärmung dar.

Der global gemittelte AHF ist heutzutage vernachlässigbar klein im Vergleich zu dem indirekten Forcing durch Treibhausgasemissionen. Auf lokaler oder regionaler Ebene hat das Forcing jedoch einen signifikanten Einfluss. Die Energieproduktion hat in der Vergangenheit ein konstant exponentielles Wachstum aufgezeigt. Dieser Trend kann durch die Erschließung neuer CO_2-neutraler Energiequellen, wie zum Beispiel Fusionsenergie, weiter bestärkt und angetrieben werden. In solch einem Szenario führt das AHF Forcing zu einem auch global relevanten Beitrag zum menschengemachten Klimawandel abseits der Treibhausgasemissionen.

In dieser Arbeit sollen die Auswirkungen eines wachsenden AHF auf das Klima abgeschätzt werden. Im ersten Teil wird das zusätzliche Forcing in einfache und konzeptionelle, null- und eindimensionale Energiebilanzmodelle (EBM) eingebaut. Diese bieten schnelle Größenordnungsabschätzungen des Temperaturanstiegs. Im eindimensionalen EBM erhöht die Eis-Albedo-Rückkopplung die Temperatur signifikant im Verlgeich zum nulldimensionalen Fall aufgrund von verstärkter Eisschmelze. Zusätzlich, wird das AHF Forcing in das Erdsystemmodell mittlerer Komplexität CLIMBER-3α eingebaut. Dieses erlaubt eine Analyse des Effekts eines heterogenen AHF Forcings und gibt weitere Einblicke in die Einflüsse auf Prozessse wie den Wärmefluss in den Ozean, Veränderungen in Meereis und Schneebedeckung und die Ozeanzirkulation.

Der global gemittelte Temperaturanstieg für das heutige AHF Forcing beträgt $0.010 - 0.016\,\mathrm{K}$ in allen realistischen, getesteten Modellkonfigurationen. Ein transienter Anstieg des Forcings auf den zehnfachen Wert erwärmt die Erde um weitere $0.1 - 0.2\,\mathrm{K}$ in den vorgestellten Modellen. Weiteres Wachstum kann zusätzlich auch das Kippen von bestimmten Klimaelementen beeinflussen.

Die meisten erneuerbaren Energiequellen tragen nicht oder nur kaum zu der anthropogenen Abwärme bei, da deren Energie sowieso dissipiert. Daher beseitigt ein Wechsel auf einen CO_2-neutralen, erneuerbaren Energiemix, der explizit nicht auf nuklearen Brennstoffen basiert, unabhängig von dem Wachstum der Energieproduktion die lokalen wie auch globalen Auswirkungen des AHF Effekts.

Contents

Chapter 1

Introduction to the Anthropogenic Heat Flux (AHF)

The Great Acceleration. The increasing human activity on the planet has led many researchers to the conclusion that the Earth System has left the stable Holocene and entered a new geological epoch. This is called the Anthropocene, in which human activity has become a key pressure on the planet (Crutzen, 2002). In the most recent phase in the Anthropocene (roughly since the 1950s) many parameters, both in the environmental sphere, like the tropical forest loss, or in the socio-economic sphere, like the population size or the primary energy consumption, exhibit exponential growth behaviour. This period is often referred to as the 'Great Acceleration' (Steffen et al., 2015)[1].

One of the major threats to the civilisation in the Anthropocene is the accelerated emission of greenhouse gases, which has already caused a global warming of $0.85\,K$ compared to pre-industrial times (IPCC, 2013). Continuing these trends will not only further increase the global mean temperature but also lead to e.g. more frequent and stronger extreme weather events or rising sea levels, with presumably disastrous consequences for the human civilisation. In fact, the anthropogenic pressure on the Earth System can even lead to irreversible tipping-like behaviour of large parts of the climate system, thereby altering the living conditions on this planet substantially in a not too-far future (Steffen et al., 2018).

In an attempt to mitigate the danger from enhanced climate change, the political leaders of the world have negotiated the Paris Agreement in 2015 to limit global warming to 'well below $2°C$'. This, however, requires rapid and fast actions in order to reach a world with zero greenhouse gas emissions (Schellnhuber, Rahmstorf, and Winkelmann, 2016).

The Anthropogenic Heat Flux (AHF). Despite the existential threat from the greenhouse effect, in this thesis, a much smaller process is investigated that also contributes to global warming: The direct warming due to the anthropogenic heat flux (AHF). Especially if the energy production is completely decarbonised but scaled up in size, this might become a relevant climate impact.

The second law of thermodynamic demands that all energy eventually dissipates as heat on long enough time scales. This, of course, holds also for the consumption of energy by the human civilisation. Heat is produced e.g. during the conversion from primary to consumable energy as well as through combustion

---

[1] A comprehensive and illustrative overview of the Anthropocene and the Great Acceleration can be found on: `http://www.anthropocene.info/great-acceleration.php`.

of energy sources or due to friction and other efficiency losses when this energy is used. This is referred to as 'waste heat'.

An example is the waste heat released during the process of refining oil to produce fuel for cars, during combustion in the engine as well as during the motion of the car due to friction losses of the wheels, in the air and at the brake discs. Eventually, the whole potential energy of the raw oil is transformed into heat.

In principle, this of course applies to all processes in nature, as well. However, technological invention has enabled the civilisation to extract energy from sources that are not accounted for in the 'natural' equilibrium energy balance. E.g. the appropriation of fossil fuel resources for energy production inserts additional energy directly into the system (next to the indirect greenhouse effect). This energy then dissipates as heat into the atmosphere and thereby alters the climate conditions of the planet.

So far, this has often been neglected in the modelling of anthropogenic impacts on the climate due to the dominance of the indirect forcing induced by greenhouse gas emissions.

In summary, human activity causes the insertion of additional heat (the AHF) into the Earth System, which contributes to climate warming. This constraint of waste heat being an additional input applies to the vast majority of the total worldwide primary energy sources today, i.e., in particular, energy from fossil fuels, nuclear energy but also, partially, from other sources like solar radiation or geothermal energy[2].

In this thesis, the historic AHF forcing is derived from the total 'Primary Energy Production' (or 'Total Primary Power') data obtained from IEA (2014). It is assumed that this energy converts completely and instantaneously into heat.

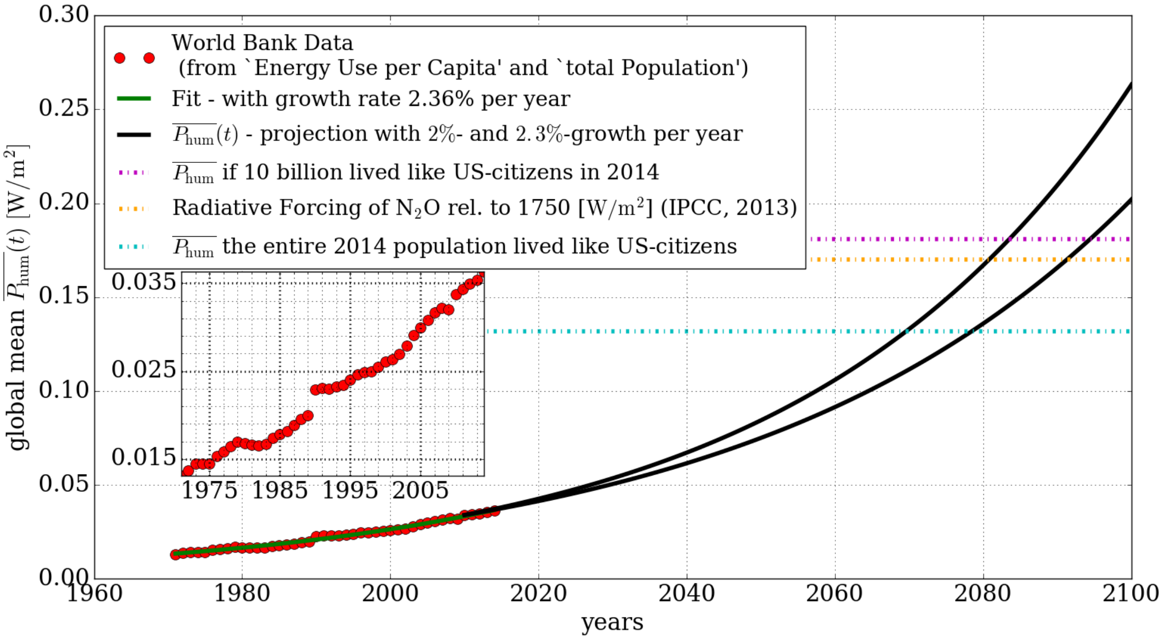

Figure 1.1: Globally averaged AHF $P_{\rm hum}$ $[\frac{\rm W}{\rm m^2}]$ (from IEA (2014) and The World Bank (2018)) and future projections of 2%- and 2.3%-growth per year. This is compared with the N_2O GWP100 forcing from the (IPCC, 2013) and simple order of magnitude estimates from energy use data of the US[3](IEA, 2014).

---

[2] A more elaborate differentiation of the energy sources is presented in Section 5.

[3] Disclaimer: AHF from US citizens is chosen as a reference here because the US lifestyle has often been referred to as desirable in the public. This figure does not mean to include any accusation to US citizens.

In the past decades, the AHF has increased exponentially with a growth rate of 2.36% per year (see Figure 1.1). The globally averaged AHF forcing, $\overline{P_{\mathrm{hum}}}$, in 2010 amounted to $\overline{P_{\mathrm{hum}}}(2010) = 0.034\,\mathrm{W/m^2}$ due to the total primary power consumption of roughly 17 TW.

For comparison, humans requires roughly 2000-3000 kcal of energy per day in order to sustain their general body functions, like the metabolism and physical activity. I.e. the world population today (~ 7.5 billion) needs a minimum power input of $0.7 - 1.1\,\mathrm{TW}$[4]. This helps to put the additional, much larger 17 TW (Figure 1.1) anthropogenic primary energy production that fuels our transportation, heating and consumption needs nowadays into context.

While this direct forcing from the AHF is only ca. 2% of the indirect radiative forcing from the anthropogenic CO_2 emissions (IPCC, 2013), a continued exponential growth would lead to a relevant impact on the global climate in a conceivable future. This is e.g. shown in Figure 1.1, where continued 2% and 2.3% growth per year are compared. In both cases the forcing from the AHF due to human activity reaches the same order of magnitude of the forcing from the increase in the N_2O concentration before the end of the century.

Research on the AHF. The AHF has already been subject to various studies. In his work introducing the Energy Balance Model in 1969, M. Budyko writes: ‘All the energy used by man is transformed into heat, the main portion of this energy being an additional source of heat as compared to the present radiation gain.’ He predicts that by continuing the energy growth at the current rate, ‘in the comparatively near future the possibility of glaciation expansion will be excluded and there will appear the reverse one of polar ice melting [...].’ (Budyko, 1969). On the other hand, 35 years later, P.J. Crutzen states that the AHF is a ‘relatively small term in Earth’s global energy budget. Regionally, however, energy production density can be much larger [... and] cause the so-called “urban heat island” (UHI) effect’ (Crutzen, 2004).

These statements, while implying contradictory views, show the two branches of the research in this field:

- On one hand, energy scenarios for the future beyond short-term developments are derived, which are based on theoretical models or very basic physical theories for the evolution of the civilisation on a global scale. The resulting impacts of the extreme AHF scenarios are estimated in very simple models or orders of magnitude calculations. Example studies for this research focus are Chaisson (2008) or Berg, Hartley, and Richters (2015).
- In a mostly unassociated, second research branch, the focus lies on local, current or near future impacts of waste heat and the AHF. In particular, this means that energy projections are either based on historical energy production data or projected to be reasonably close to today’s values. This is the much larger fraction of the research, including a vast amount of studies on the urban heat island effect on a regional level (as stated in Crutzen 2004) or e.g. Zhang, Cai, and Hu (2013) on a larger scale.

Furthermore, some effort has been put into providing data for the AHF (e.g. Yang et al. 2017, Flanner 2009 and Chen et al. 2016) in order to analyse regional and global impacts of this process in the future.

One approach to link the two branches has been made by Flanner (2009) by inserting an exponentially growing AHF over the next century into a globally coupled climate model. The conclusions, however,

---

[4] If this energy is released, it corresponds to a constant emission of roughly 100 W/person from the human bodies (or in terms of forcing $0.001\,\mathrm{W/m^2}$).

focus more on the direct impacts on local to continental scale, like temperature changes in highly urbanised regions or the seasonal cycle of the AHF impacts.

This thesis aims at contributing to and extending this by focusing more on the global, long-term effects of an increasing AHF forcing in the range of simple, conceptual climate models up to numerical climate models of intermediate complexity (EMIC). This helps to improve the understanding of the processes that drive the global warming from the AHF.

Future Energy Scenarios. Two future primary energy projections are used in this thesis to calculate the forcing from the AHF: Firstly, a (worst-case[5]) scenario from a complex Integrated Assessment Model (the Shared Socio-Economic Pathway framework developed in Vuuren and Carter 2014). However, most of the time the second scenario is assumed – a continuation of an exponential growth of energy production over the next century (as e.g. illustrated in Figure 1.1). This second approach results in a much higher primary energy production than most elaborate projections. It serves as a simple, first-guess business-as-usual assumption for the future energy production.

Such a scenario might become especially relevant when, at some point in the future, fusion power plants are able to sustain the global energy production. While fusion power, in principle, provides emission-free energy based on virtually unlimited resources, it clearly contributes to the additional heat in the AHF. Nevertheless, the development of fusion reactors is often accompanied by the ultimate strive to provide unlimited energy production in the public, media or even among scientists[6]. Thus, as a risk-averse approach, the continued growth scenario is investigated in this thesis in order to rather overestimate the growth of the AHF forcing than to underestimate it[7].

Structure of the thesis. The general idea of this thesis is to project the future amount of AHF given the assumptions mentioned above and then to insert it into climate models in order to calculate the corresponding response.

In Chapter 2 and 3, the forcing from the AHF is examined with simple zero-dimensional and one-dimensional Energy Balance Models (EBMs). These mainly serve the purpose of illustrating certain basic physical processes of the Earth System and of providing quick hands-on tools to estimate climate impacts. Notably, the one-dimensional EBM includes the ice-albedo feedback, which is investigated in detail e.g. with respect to the stability of the ice-cap.

Chapter 4 investigates the impact of the AHF in an Earth System Model of Intermediate Complexity (EMIC): CLIMBER-3α. This model includes more dynamically simulated processes, which leads to a more complete picture of the possible climate impacts of the AHF. Among others, this includes mainly the ice- and snow-albedo effect, or changes in the ocean heat flux or ocean circulation due to the AHF forcing. The 2D spatial resolution of CLIMBER-3α enables the simulation of heterogeneous AHF forcing. From this, an approach to determine the dependency of the location of the forcing on the global impact is pursued.

In these modelling chapters, the assumption holds that the AHF is represented by the total primary energy production. Chapter 5 looks into the actual contribution of each individual energy source to the additional heat input into the atmosphere more critically. Furthermore, approaches to estimate the maximum available energy of each energy source to meet the global energy demand are sketched.

---

[5] In terms of primary energy production, not in terms of climate impacts.

[6] Cf. a quick internet research on the keywords: ‘fusion unlimited energy’.

[7] More arguments supporting the use of higher energy production scenarios in this work are presented in Chapter 6.

Finally, in Chapter 6, the assumption of an exponential growth of the AHF is discussed especially with respect to socio-economic limits and to some degree justified by discussing consequences of a risk-adverse business-as-usual scenario as well as a theoretical model of the global economy based on physical laws adopted from (Garrett, 2014) .

A summary and potential political implications are presented in the conclusion in Chapter 7.

Code. A minimum working code is embedded in Chapters 2 and 3 to quickly reproduce the models and verify results. Any additional code (including the methods to plot most Figures) is stored in Masterthesis_public_code/ on a GitHub repository. The code is written in the Python programming language v2.7.14 (`http://www.python.org`) and makes heavy use of the packages 'Numpy' (`http://www.numpy.org/`), 'Matplotlib' (`https://matplotlib.org`) and 'Xarray' (`http://xarray.pydata.org/en/stable/`).

To reproduce the results in Chapter 4 is more complicated and requires access to the model code. Notes and Instructions can be found on: How_to_run_and_analyse_climber.

Chapter 2

The AHF in the Zero-dimensional Energy Balance Model (EBM-0D)

In this chapter, the most simple method to estimate the global mean temperature change and some further climate impacts due to the AHF is presented by using modified, conceptual Energy Balance Models (EBMs).

Energy Balance Models in General Energy Balance Models (EBMs) are simple climate models, which estimate the energy fluxes coming in and out of a system. These systems are usually either zero-dimensional, i.e. they consist of globally averaged variables (this chapter), or one-dimensional, i.e. longitudinally averaged variables (Chapter 3). Furthermore, EBMs can also include a multi-layered atmosphere (see e.g. Rose 2017), but this is not pursued here.

In equilibrium, the absorbed energy by the system is balanced by the emitted energy. I.e. at the top of the atmosphere (TOA) of the Earth System the following equation holds for an equilibrium climate state:

$$0 = \mathrm{INC} - \mathrm{OLR} \ , \tag{2.1}$$

where INC is the (absorbed) short wave (SW) **inc**oming solar energy in $\frac{\mathrm{W}}{\mathrm{m}^2}$ and OLR is the **o**utgoing **l**ong wave **r**adiation, also in $\frac{\mathrm{W}}{\mathrm{m}^2}$.

For this study, a second incoming energy source P_{hum}, representing the anthropogenic heat flux (AHF), is added as a direct additional heat input[1] from 'outside the system'[2].

The OLR is usually parametrised via a measurable variable like the temperature T_S at the surface. Hence, the surface temperature responds to changes in the net energy balance at the TOA via

$$C \cdot \frac{\partial T_S}{\partial t} = \mathrm{INC} - \mathrm{OLR}(T_S) + P_{\mathrm{hum}} \ , \tag{2.2}$$

where C is a heat capacity, until equilibrium is reached, i.e.

$$\frac{\partial T_S}{\partial t} = 0 \ . \tag{2.3}$$

---

[1] Other methods used to insert the AHF into a climate model are described in the Appendix A.1.

[2] 'Outside the system' can e.g. mean from coal stored below the surface of the earth.

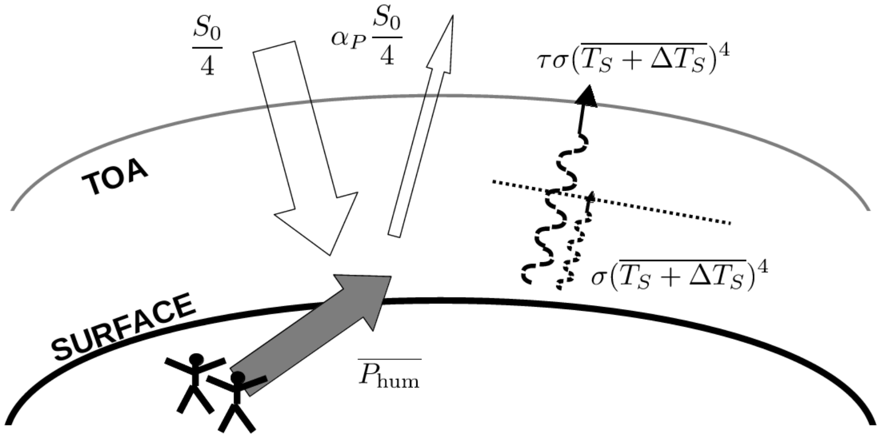

Figure 2.1: Sketch of the EBM-0D model used here. For long wave radiation the atmosphere acts as a semipermeable mirror (dashed), which blocks a fraction $(1 - \tau)$ of the outgoing long wave radiation. At the boundaries of the system the radiative fluxes are in equilibrium. The flux of P_{hum} is sketched from outside the system to symbolise its input character, but in reality it might just as well originate from within the system or 'below' the surface (e.g. if coal is extracted from the ground and burned).

2.1 Components of the EBM-0D

The most simple EBM is the annual mean, equilibrium, zero-dimensional EBM, as described by equations (2.2) and (2.3) with globally averaged, scalar variables. The components of the model are illustrated in the sketch in Figure 2.1 and described below:

- **Solar Radiation $\mathbf{INC_{solar}}$:** The net incoming solar power (per m^2) at the TOA can be approximated via

  $$\text{INC}_{\text{solar}} = \frac{S_0}{4} \cdot (1 - \alpha_P) \ , \tag{2.4}$$

  where $S_0 \approx 1361 \, \frac{\text{W}}{\text{m}^2}$ is the annual mean, globally averaged solar constant at the TOA (Kopp and Lean, 2011) and $\alpha_P = 0.3$ is a rough estimate for the planetary albedo at the current ice fraction, which accounts for the reflection of solar SW radiation (see e.g. Donohoe and Battisti 2011). Any approaches to incorporate the effects of ice- or cloud-feedback on the planetary albedo or solar and orbital variations are not carried out in this first step.

- **Outgoing Long Wave Radiation OLR:** The absorption of outgoing **l**ong**w**ave (LW) radiation from the surface by the atmosphere is modelled as a semipermeable mirror, which reduces the total amount of OLR reaching the TOA. Here, the OLR depends only on the global mean temperature $\overline{T_S}$ at the surface and the transmittance τ of the LW radiation through the atmosphere. The earth is typically assumed to be a blackbody. Hence, the radiation is described via the Stefan-Boltzmann-law (see e.g. Pierrehumbert 2010):

  $$\text{OLR}(\overline{T_S}) = \tau \cdot \sigma \overline{T_S}^4 \tag{2.5}$$

  The transmittance τ of OLR through the atmosphere is the crucial tuning parameter in this model. It is adjusted in such a way that a planet with a typical global mean surface temperature of $\overline{T_S} \approx 288 \, K$ is obtained.

  For some EBMs in the following sections, a CO_2-dependent parametrisation for the $\text{OLR}(\overline{T_S})$ is chosen which, for example, enables the simulation of changing greenhouse effect in the EBM. There-

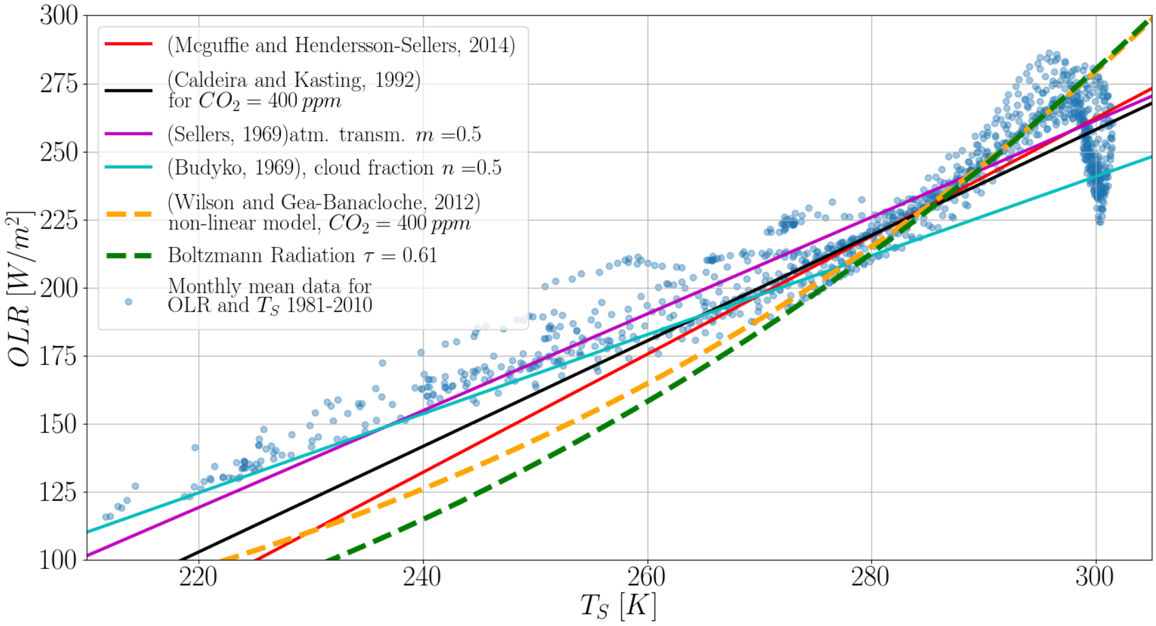

Figure 2.2: OLR($\overline{T_S}$): Linear approximations used in previous studies (Budyko 1969, Sellers 1969, Mcguffie and Henderson-Sellers 2014 and Caldeira and Kasting 1992), the more complex approach by Wilson and Gea-Banacloche (2012) and the simple Boltzmann law with tuned transmissivity $\tau = 0.61$ through the atmosphere. These parametrisations are compared to historic, monthly mean, longitudinally averaged OLR(latitude)-data plotted over T_{skin}(latitude)-data produced by NCEP Reanalysis 2 for the years 1981-2010 (NOAA ESRL PSD 2011a and NOAA ESRL PSD 2011b), which is partly adopted from Rose (2017)[3].

fore, a simpler OLR parametrisation is required. A widely used approach is to approximate the Boltzmann parametrisation by a linear curve:

$$\text{OLR}_{\text{Linear}}(\overline{T_S}) = A + B \cdot \overline{T_S}\ . \tag{2.6}$$

Figure 2.2 shows a comparison of multiple established parameter choices, including e.g. the approaches based on Budyko (1969) and Sellers (1969), which are not used here, or the approximation by Mcguffie and Henderson-Sellers (2014). Notably, Caldeira and Kasting (1992) have parametrised the impact of CO_2 on the OLR, i.e. $A(CO_2)$, $B(CO_2)$, which will be used later in this analysis as well. It should be stated clearly that the linear parametrisation of OLR in equation (2.6) obviously neglects important non-linear features. In particular, this leads to an underestimation of the OLR for higher temperatures and, hence, a stronger temperature response to forcings.

Another approach that also allows for adjustments in the CO_2-concentration is described by Wilson and Gea-Banacloche (2012) and also shown in Figure 2.2. In a nutshell, Wilson and Gea-Banacloche (2012) use a random-walk model to estimate the transmittance of LW radiation at a specific wavelength in the atmosphere given only the absorption spectrum of CO_2 and its density profile ρ (pressure p). However, the temperature at the tropopause and the greenhouse effect of

---

[3] Note, that in equator-near regions with the hottest temperatures, the large cloud cover causes a significant drop in the observed OLR-data in this region in this data. This drop would not occur if the cloud cover in warm regions were different. Hence, this correlation of T- and OLR-data does not necessarily imply the desired functional relation OLR(T) as the influences of cloud patterns, oceans, land masses etc. are neglected in this simple comparison.

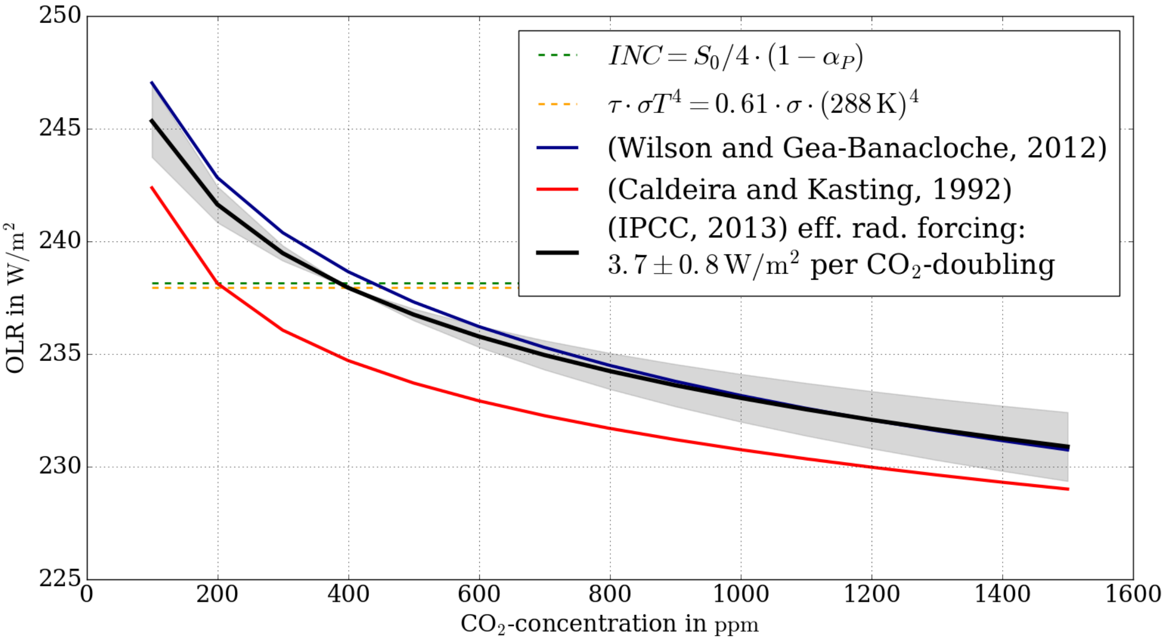

Figure 2.3: $\mathrm{OLR}(\overline{T_S}, CO_2)$: Caldeira and Kasting (1992)'s and Wilson and Gea-Banacloche (2012)'s approaches to model the CO_2-dependency of OLR. For comparison, the equilibrium radiative forcing (ERF) from the IPCC (2013) is shown. This is derived via $\mathrm{OLR}_{(\mathrm{IPCC,\,2013})} = \tau \cdot \sigma(288\,\mathrm{K})^4 + \mathrm{ERF} \cdot ln(\frac{CO_2}{400\,\mathrm{ppm}})/ln(2)$, where $ERF = 3.7 \pm 0.8\,\mathrm{W/m^2}$ per doubling of CO_2 (uncertainty range in grey region). The calculated equilibrium radiative forcings are $-3.0\,\mathrm{W/m^2}$ and $-4.2\,\mathrm{W/m^2}$ for Caldeira and Kasting (1992)'s and Wilson and Gea-Banacloche (2012), respectively.

non-CO_2 gases need to be tuned to obtain realistic values (e.g. $\overline{T_S} \approx 288\,\mathrm{K}$).

$$\mathrm{OLR}_{(\mathrm{Wilson\ and\ Gea-Banacloche,\ 2012})}(\overline{T_S}) = (1 - x_{\mathrm{non-CO_2}} - x_{\mathrm{CO_2}}) \cdot \sigma \overline{T_S}^4 \,, \tag{2.7}$$

where $x_{\mathrm{CO_2}}$ is the amount of radiation absorbed by CO_2, which is integrated over the wavelength spectrum, and $x_{\mathrm{non-CO_2}}$ is tuned to retrieve today's climate conditions. While this is a straight forward and easily understood approach, it is not computationally feasible for more complex models than the EBM-0D as the whole wavelength spectrum needs to be integrated in order to get the OLR for a given temperature at any point. Wilson and Gea-Banacloche (2012) also approximate the resulting equation for $\mathrm{OLR}(\overline{T_S})$, but using this approximation would both contradict the spirit of keeping the model transparent and low-level and perhaps give a false impression of accurate physical description of the radiation process.

The two different approaches to obtain a CO_2 dependent OLR parametrisation by Wilson and Gea-Banacloche (2012) and Caldeira and Kasting (1992) are compared in Figure 2.3.

- **AHF:** So far, the processes follow a standard set up of an EBM-0D. Now, though, the AHF term (in $\mathrm{W/m^2}$) is additionally added to the system as in equation (2.2).

  An estimate for global mean anthropogenic heat flux $\overline{P_{\mathrm{hum}}}$ today can be retrieved from the global primary energy production E (here derived from 'Energy Use per Capita' data by IEA (2014) and 'Population' data by The World Bank (2018)) and dividing this by the area of the planet $4\pi r_{\mathrm{earth}}^2$:

$$\overline{P_{\mathrm{hum}}}\,[\frac{\mathrm{W}}{\mathrm{m}^2}] = E\,[\frac{\mathrm{kg\ Oil}}{\mathrm{capita}\cdot\mathrm{yr}}] \cdot Pop\,[\mathrm{capita}] \cdot 11.63\,\frac{\mathrm{kWh}}{\mathrm{kg\ Oil}} \cdot \frac{1}{365\cdot 24\,\mathrm{h/yr}} \cdot \frac{1}{4\pi r_{\mathrm{earth}}^2} \,, \tag{2.8}$$

where 11.63 $[\frac{\text{kWh}}{\text{kg Oil}}]$ is the standard conversion between the energy units oil equivalent and kWh.

As stated before, the assumption that all primary energy production dissipates as additional heat is a simplification. However, the vast majority of this ($\geq 85\%$) does contribute to the AHF today. With this assumption the current P_{hum} (in 2010) can be approximated to 0.034 $\frac{\text{W}}{\text{m}^2}$ via equation (2.8). This corresponds to 2% of the radiative forcing from past CO_2-emissions (1.68 W/m^2 from IPCC 2013), which is in good agreement with the method used in other studies like Zhang and Caldeira (2015) or Berg, Hartley, and Richters (2015).

Flanner (2009) uses only non-renewable energy instead of the total primary energy, resulting in a slightly smaller forcing. However, this is deliberately not chosen in this thesis due to the more general definition of the AHF as additional heat, which can e.g. also come from geothermal or solar energy sources. A more detailed analysis of different energy sources and their impact on the AHF follows in Chapter 5.

2.2 Implementation

The code embedded in the following text shows the actual implementation of the EBM-0D. It is stored in EBM0D.py on the GitHub repository.

Listing 2.1: EBM0D.py

```python
import numpy as np
import matplotlib.pyplot as plt
```

In total, the equilibrium, zero-dimensional EBM from equation (2.2) and (2.3) (with the Boltzmann OLR parametrisation according to equation (2.5)) gives:

$$0 = \frac{S_0}{4} \cdot (1 - \alpha_P) - \tau\sigma\overline{(T_S + \Delta T_S)}^4 + \overline{P_{\text{hum}}}\,, \tag{2.9}$$

where $\overline{\Delta T_S}$ is the global mean (equilibrium) temperature change due to the AHF. Rearranging this equation gives:

$$\overline{\Delta T_S} = \left(\frac{\frac{S_0}{4} \cdot (1 - \alpha_P) + \overline{P_{\text{hum}}}}{\tau\sigma}\right)^{\frac{1}{4}} - \overline{T_S} = \left(T_S^4 + \frac{\overline{P_{\text{hum}}}}{\tau\sigma}\right)^{\frac{1}{4}} - \overline{T_S}\,. \tag{2.10}$$

With this equation, the free parameter τ is tuned to get $\overline{T_S} = 288\,\text{K} \approx 15°C$ for a pre-industrial climate state, i.e. $\overline{P_{\text{hum}}} = 0$ (and, hence, $\Delta T_S = 0$). The tuning yields $\tau = 0.61$, i.e. 61% of the LW surface emission reaches the TOA in this model.

```python
S0=1361. # W/m^2 Solar constant
alpha=0.3  # Albedo
T_goal=288. # K Temperature for tuning
sigma=5.67e-8 # W/m^2/K^4
# Tune tau
tau= S0/4 * (1-alpha) / (sigma * T_goal**4)
```

For the alternative linear OLR parametrisation (equation (2.6)), equation (2.10) becomes

$$0 = \frac{S_0}{4}(1 - \alpha) - (A + B \cdot \overline{T_S + \Delta T_S}) + \overline{P_{\text{hum}}} \tag{2.11}$$

and the change in temperature due to the AHF takes the handy linear formula

$$\overline{\Delta T_S} = \frac{\frac{S_0}{4} \cdot (1 - \alpha_P) - A + \overline{P_{\text{hum}}}}{B} - \overline{T_S} = \frac{P_{\text{hum}}}{B} \ . \tag{2.12}$$

2.3 Analysis of the Model

Global Mean Temperature (Boltzmann parametrisation). The calculation in equation (2.8) gives an estimate for the current (2010) annual mean, globally averaged AHF: $P_{\text{hum}} \approx 0.034\,\frac{\text{W}}{\text{m}^2}$. From equation (2.10) (with Boltzmann parametrisation as in equation (2.5)) a temperature increase of

$$\Delta\overline{T_S} = 0.010\,\text{K} \tag{2.13}$$

compared to pre-industrial times follows. This calculation is equivalent to previous approaches in the literature (e.g. Berg, Hartley, and Richters 2015 which only differs in the value of the solar constant or Chaisson 2008).

```
T0_B=(S0/4 * (1-alpha) / (sigma*tau))**0.25
P_hum_glob=0.034 # W/m^2 AHF today
dT_P_B=((S0/4*(1-alpha)+ P_hum_glob)/(tau*sigma))**0.25- T0_B
```

Hence, there's roughly two orders of magnitude between the warming from greenhouse gas emissions and the warming from the AHF since pre-industrial times.

As described in the Introduction (e.g. Figure 1.1), the global energy production has increased exponentially since the industrial revolution. Assuming a continued 2%- or 2.3%-growth per year of the total primary energy production over the next century (or centuries) and no significant changes in the fraction of 'renewable' (or more accurately: non-contributing) energy sources, the impact of the AHF is estimated to increase accordingly in this model, eventually becoming an important feature of climate change (see Figure 2.4).

The growth rates, which describe a very simplistic 'business-as-usual' scenario, are chosen according to previous studies (2%/yr as e.g. in Berg, Hartley, and Richters 2015) or from the fit to historic data (2.3%/yr, which is a bit more conservative than the fitted 2.36%/yr).

If these continued growth scenarios are extended for 200 years, the AHF would be responsible for 0.6 K global mean temperature change in this model, which is the same amount of warming as from today's total anthropogenic forcing since 1950 (IPCC, 2013), or 1 K, respectively.

Global Mean Temperature (Other Parametrisations). Using the linear approximation (equation (2.6)) instead of the Boltzmann parametrisation (equation (2.5)), which leads to the EBM equation (2.11), the temperature impact for the current $P_{\text{hum}} = 0.034\,\text{W/m}^2$ is nearly twice as large: $\Delta\overline{T_S} = 0.016\,\text{K}$ (for Mcguffie and Henderson-Sellers 2014) or 0.018 K (for Caldeira and Kasting 1992 with $\text{CO}_2 = 388\,\text{ppm}$).

```
# for (Mcguffie and Hendersson-Sellers, 2014)
A_M=-388.74
B_M=2.17
T0_M=(S0/4*(1-alpha)-A_M)/B_M
dT_P_M=(S0/4*(1-alpha)-A_M+P_hum_glob)/B_M - T0_M
# for (Caldeira and Kasting, 1992)
def xi(co2):  # needs CO2 concentration in ppm
```

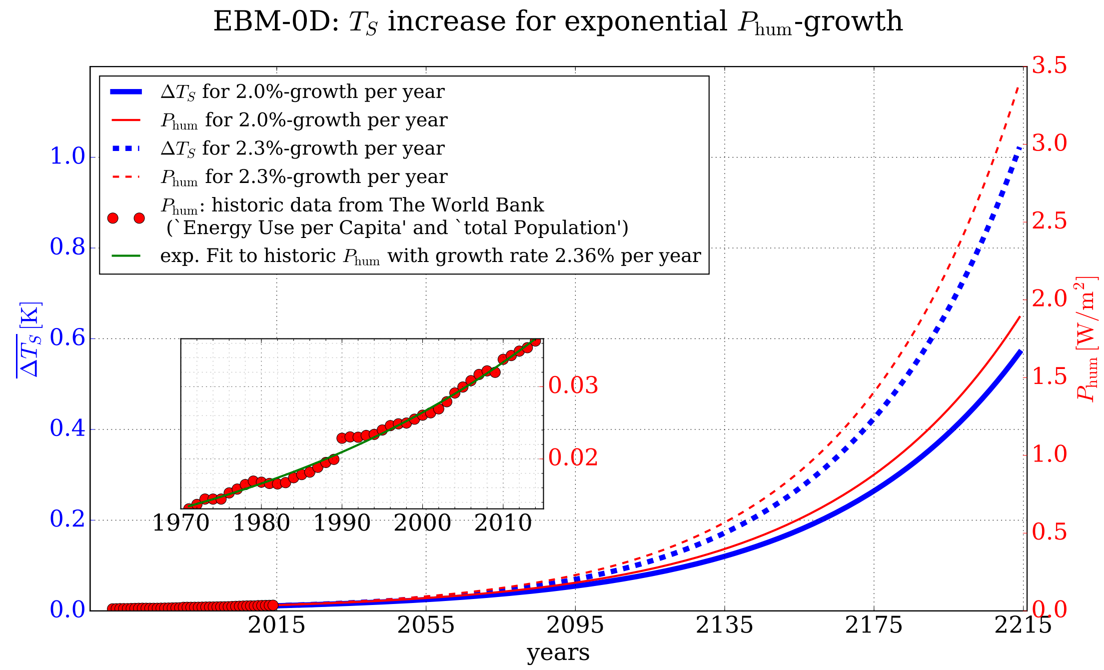

Figure 2.4: Future projections with 2% and 2.3%-growth per year and the resulting temperature impact in the EBM-0D model. The historic data for P_{hum} is derived from 'Energy Use per Capita'- (IEA, 2014) and 'Population'-data (The World Bank, 2018). An exponential fit is applied to these past values with a resulting growth rate of 2.36%/yr. Note that breaks in the time series occur due to revisions of methods and data by IEA (2014).

```
    return np.log(co2*1./300.)
def A_cald(co2):
    c=xi(co2)
    return -326.4 + 9.161 *c - 3.164 *c**2 + 0.5468* c**3
def B_cald(co2):
    c=xi(co2)
    return 1.953 - 0.04866 *c +0.01309* c**2 - 0.002577* c**3
CO2=388
A_C=A_cald(CO2)
B_C=B_cald(CO2)
T0_C=(S0/4*(1-alpha)-A_C)/B_C
dT_P_C=(S0/4*(1-alpha)-A_C+P_hum_glob)/B_C - T0_C
```

For the parametrisation in Wilson and Gea-Banacloche (2012) (for $\mathrm{CO_2} = 388\,\mathrm{ppm}$) the temperature impact is $\Delta\overline{T_S} = 0.011\,\mathrm{K}$, which is naturally more similar to the value retrieved from the Boltzmann parametrisation (equation (2.5)). The code to reproduce these results from Wilson and Gea-Banacloche (2012) can be found in EBM-0D_Wilson_and_Gea-Banacloche(2012).py.

Tenfold Increase of the AHF. Moreover, in Chapter 3, a simple tenfold increase of the AHF in 2010, i.e. $P_{\mathrm{hum}} = 0.34\,\mathrm{W/m^2}$, is investigated in order to obtain a benchmark result. This corresponds to a continued 2% increase for 116 years. For the EBM-0D, the tenfold forcing results in an additional

$$\Delta\overline{T_{S,\,\mathrm{tenfold}}} = 0.092\,K \tag{2.14}$$

compared to 2010 for the Boltzmann parametrisation[4].

---

[4] Alternatively, $\Delta\overline{T_S}_{\mathrm{tenfold}} = 0.14\,K$ and $\Delta\overline{T_S}_{\mathrm{tenfold}} = 0.16\,K$ for the linear approximations mentioned above.

$\mathbf{CO_2}$-amplification. This paragraph deals with non-linear effects in the EBM when CO_2 and the AHF increase simultaneously. Increasing the AHF leads to an increase of outgoing surface radiation in order to regain radiative equilibrium at the TOA. A higher CO_2 concentration, however, leads to increased absorption and emission of this outgoing radiation in the atmosphere. Therefore, there is an additional amplification of the temperature increase in the EBM-0D when CO_2-levels and P_{hum}-emissions rise simultaneously.

In this thesis, the effects of CO_2 are described by either the linear parametrisation of OLR by Caldeira and Kasting (1992) or the Boltzmann-like parametrisation by Wilson and Gea-Banacloche (2012). The analytical solution for this effect in the EBM-0D in the first case – the linear OLR parametrisation – is derived in Appendix A.2. The resulting equation for the temperature increase is:

$$\Delta T_{\mathrm{combined}} = \Delta T_{\mathrm{CO_2}} + \Delta T_P + \frac{\delta P}{B(\mathrm{CO_2} + \delta \mathrm{CO_2})} - \frac{\delta P}{B(\mathrm{CO_2})}\,, \tag{2.15}$$

where $B(\mathrm{CO_2})$ is the slope of the linear OLR approximation. $\Delta T_{\mathrm{CO_2}}$ and ΔT_P are the temperature impacts from separate growth simulations keeping the other variables constant ($\Delta T_P \hat{=} \overline{\Delta T_S}$ from before) and $\Delta T_{\mathrm{combined}}$ is the temperature impact from the simultaneous increase of P_{hum} and CO_2. The last two terms represent the 'amplification' or additional temperature increase, which is always positive for $\delta \mathrm{CO_2} > 0$. For example, the tenfold increase of P_{hum} to $0.34\,\mathrm{W/m^2}$ from today (2010) and a simultaneous doubling of the CO_2 concentration in 2010 (i.e. $\mathrm{CO_2} \rightarrow 776\,\mathrm{ppm}$) gives an additional $0.002\,\mathrm{K}$ warmer equilibrium temperature (roughly 2% of the temperature response due to the sole AHF increase in equation 2.14). Due to the higher CO_2 concentration, however, the total temperature change is roughly $1.76\,\mathrm{K}$ in this scenario, which makes the additional amplification a rather negligible side effect. Furthermore, since $B(\mathrm{CO_2})$, which decreases with CO_2, flattens for high CO_2 values, the amplification slowly vanishes (even further) under growing CO_2 concentrations.

Wilson and Gea-Banacloche (2012)'s approach also obtains an amplified warming for simultaneous P_{hum}- and CO_2-growth. However, the effect is even smaller (additional $0.0009\,\mathrm{K}$) due to the T^4-dependence of the $\mathrm{OLR}(T)$ in the Boltzmann-like parametrisation (equation (2.7)).

Chapter 3

The AHF in the One-dimensional Energy Balance Model (EBM-1D)

While the EBM-0D, described in the previous chapter, provides a rough estimate of the potential impact of growing energy production, its simple setup neglects various important processes. The one-dimensional EBM represents an extension by the latitude dimension ('from pole to pole') in order to calculate annual mean temperatures for different latitude bands. This enables the possibility of simulating horizontal heat fluxes in north-south-direction and the ice-albedo feedback. Also, the influence of a heterogeneous P_{hum}-distribution can be investigated. The full step-by-step code to reproduce this model is embedded in the text in this chapter in several cells and can be found in EBM1D_main.py on the GitHub repository.

Listing 3.1: EBM1D_main.py

```python
import numpy as np
import matplotlib.pyplot as plt
```

3.1 Components of the EBM-1D

Extending the basic EBM (equation (2.1) to (2.3)) to the EBM-1D reads:

$$0 = \mathrm{INC}(\theta) - \mathrm{OLR}(T(\theta)) + P_{\mathrm{hum}}(\theta) + h(\theta) \ , \tag{3.1}$$

with latitude θ, the so-called convergence of energy transport $h(\theta)$ (see e.g. Rose 2017), which accounts for the meridional transport (described in detail in the following), and the annual mean surface temperature profile, now simply denoted as $T(\theta)$. The respective terms of this equation are described below and also illustrated in the sketch in Figure 3.1:

- **Meridional transport $\mathbf{h}(\theta)$:** The contribution from the meridional energy transport $h(\theta)$ at a specific latitude band θ to the energy balance is a complex process and not easy to calculate (e.g. due to circulation of air masses). In order to parametrise this, the approach in this thesis is to use the surface temperature gradient in a latitude band θ to define the meridional transport $H(\theta)$

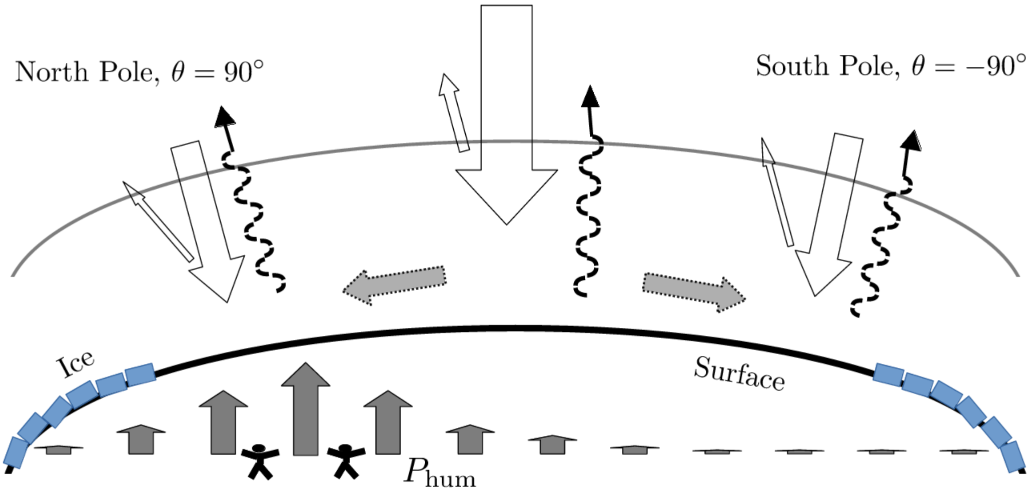

Figure 3.1: Sketch of the one-dimensional EBM. The AHF-input is concentrated on the Northern Hemisphere. New processes compared to the EBM-0D sketched in Figure 2.1 are the meridional transport (grey arrows) and the building of ice in cells near the poles.

across the boundary of this latitude band (cf. Lecture 15 in Rose 2017):

$$H(\theta) = -D \cdot 2\pi \cdot r_{\text{earth}}^2 \cdot \cos(\theta) \cdot \frac{\partial T(\theta)}{\partial \theta} \,. \tag{3.2}$$

With the area of a latitude band θ,

$$A_{\text{band}}(\theta) = 2\pi \cdot r_{\text{earth}} \cos(\theta) \cdot r_{\text{earth}} \, d\theta \,, \tag{3.3}$$

the total contribution to the local energy budget in equation (3.1) from the meridional transport both **in** ($H(\theta)$) and **out** ($H(\theta + \delta\theta)$) of the band yields:

$$\begin{aligned} h(\theta) &= \frac{H(\theta) - H(\theta+\delta\theta)}{A_{\text{band}}(\theta)} \\ &= -\frac{1}{2\pi \cdot r_{\text{earth}}^2 \cdot \cos(\theta)} \cdot \frac{H(\theta+\delta\theta) - H(\theta)}{d\theta} \\ &= -\frac{1}{2\pi \cdot r_{\text{earth}}^2 \cdot \cos(\theta)} \cdot \frac{\partial H(\theta)}{\partial \theta} \\ &= D \cdot \frac{1}{\cos(\theta)} \frac{\partial}{\partial \theta} \left(\cos(\theta) \cdot \frac{\partial T(\theta)}{\partial \theta} \right) \,. \end{aligned} \tag{3.4}$$

Hence, the meridional transport is parametrised here as a diffusion process, which is a common parametrisation for EBMs (see e.g. North 1975). Note that with this definition of $h(\theta)$, the boundary conditions for $H(\theta)$ are fulfilled: $H(0°) = H(90°) = H(-90°) = 0$.

By introducing a new variable x with $x = \sin(\theta)$ equations (3.2) and (3.4) become

$$H(x) = -D \cdot 2\pi \cdot r_{\text{earth}}^2 \cdot (1 - x^2) \cdot \frac{\partial T(x)}{\partial x} \tag{3.5}$$

and

$$h(x) = -\frac{1}{2\pi \cdot r_{\text{earth}}^2} \cdot \frac{\partial H(x)}{\partial x} = D \cdot \frac{\partial}{\partial x}(1 - x^2)\frac{\partial}{\partial x} T(x) \,, \tag{3.6}$$

respectively. Here, D acts as a diffusion constant or thermal conductivity of the climate system. It has units of $\frac{\mathrm{W}}{\mathrm{m}^2\cdot\mathrm{K}}$. However, as this diffusion term parametrises not only heat exchange by diffusion but also by advection, it is not useful to interpret D as a physical characteristic of the climate system or compare it to real physical values. Furthermore, D is the main tuning parameter in this model (described later). To prevent misunderstanding and emphasise the tuning character, D does not carry a unit and will be referred to as ‘meridional transport constant’ in this thesis.

```python
def get_D(Tf, D_type, OLR_type):
  # meridional transport constant
  # will be overwritten by a more complex function later
  # For now, choose globally assigned value e.g.:
  D=global_D
  return D
```

```python
def calc_diff(T, D):
  #returns the contribution from the meridional heat transport
  # x = grid for T(lat), x_star = grid for boundaries of lat band ... more details later
  dTdx=np.diff(T)/m.dx
  # boundary condition: South/North Pole dTdx=0
  dTdx=np.insert(dTdx,0,0.)
  dTdx=np.append(dTdx,0.)
  h=D*np.diff(dTdx*(1-m.x_star**2))/m.dx_star
  return h
```

Another common parametrisation for the meridional heat transport contribution is $h(\theta) \propto T(\theta) - \langle T(\theta)\rangle_\theta$ (e.g. in Budyko 1969). However, this does not fulfil crucial features of the transport such as the no-flux boundary conditions at the poles and the equator. Hence, the slightly more complex diffusion is chosen here. Anyway, a full physical description of the meridional transport would most importantly require a proper simulation of circulation patterns like the Hadley cell, which are hard to parametrise in simple mathematical equations.

- **Solar radiation in INC($\boldsymbol{\theta}$):** The latitude dependent solar irradiance can be approximated via the second order Legendre-Polynomial as e.g. in North (1975):

$$S(\theta) = \frac{S_0}{4}(1 - 0.477 \cdot \frac{1}{2}(3 \cdot x^2 - 1)) \tag{3.7}$$

```python
def get_S():
  # solar insolation (gridpoints x) in W/m^2
  return 1361./4*(1-0.477*0.5*(3*m.x**2-1))
```

- **Albedo in INC($\boldsymbol{\theta}$):** The (longitudinally averaged) planetary albedo is mostly constant throughout the latitude bands (roughly $\alpha_P \approx 0.3$) (Donohoe and Battisti, 2011). Only in regions close to the poles the planetary albedo increases to $\alpha_P \approx 0.6$, partly due to the high reflectivity of ice, partly due to different cloud patterns over the ice-covered areas. In order to account for this influence but keep the setup simple and understandable at the same time, the albedo in this model switches from 0.3 to 0.6 at the specific latitude where the annual mean temperature falls either below $T_f = -2°\mathrm{C}$ (the temperature at which sea water freezes (NSIDC, 2018)) or below the more commonly used $T_f = -10°\mathrm{C}$ threshold (e.g. Caldeira and Kasting 1992). This specific and variable latitude is referred to as **'iceline'** in this thesis:

$$\alpha(T(\theta)) = \begin{cases} 0.6 \ \text{ for } \theta \ > \ \text{northern iceline, i.e. } \theta \text{ s.t. } \mathrm{T}(\theta) < \mathrm{T_f} \\ 0.3 \ \text{ for southern iceline } < \ \theta \ < \ \text{northern iceline, i.e. } \theta \text{ s.t. } \mathrm{T}(\theta) \geq \mathrm{T_f} \\ 0.6 \ \text{ for } \theta \ < \ \text{southern iceline , i.e. } \theta \text{ s.t. } \mathrm{T}(\theta) < \mathrm{T_f} \end{cases} \tag{3.8}$$

```python
def get_albedo(T, Tf, a0, ai):
  # returns bipolar albedo array on x-grid depending on Tf
  alpha=np.array(a0+0*T)
  ind=np.where(T<Tf)
  alpha[ind]=ai
  return alpha[:]
```

```python
def get_iceline(alpha, ai):
  # returns the icelines (i.e. lat at which T(lat)<Tf) in NH and SH
  ice_index=np.where(alpha==ai)
  icelats=m.lats[ice_index[0]]
  if alpha[-1]!=ai:
    iceline_N=m.lats[-1] # ice free NH
  else:
    iceline_N=icelats[np.where(m.lats[ice_index]>0)[0][0]] # first pos icelat
  if alpha[0]!=ai:
    iceline_S=m.lats[0] # ice free SH
  else:
    iceline_S=icelats[np.where(m.lats[ice_index]<0)[0][-1]] # last neg icelat
  return [iceline_S, iceline_N]
```

It should be noted that in this model the iceline is crucial for the tuning of the meridional transport constant D: If no ice-building is allowed in the model (i.e. also no changing albedo), the global mean temperature is approximately the same regardless of the meridional transport constant D (shown later). As soon as the building of ice is allowed, though, and the albedo adjusts accordingly, the amount of heat transported from the equator to the ice regions, where it can shift the iceline, becomes crucial for the global mean temperature. In fact, there are often several stable states for a planet for a set of parameters depending on the initial temperature profile, including a hothouse state without any ice and a planet fully covered with ice (cf. North 1984 or Rose 2017).

In total, the incoming term in equation (3.1) reads:

$$\mathrm{INC}(\theta) = S(\theta) \cdot (1 - \alpha(T(\theta))) \tag{3.9}$$

- **OLR(θ):** Analogous to the EBM-0D, the OLR is parametrised either via Boltzmann's law (equation (2.5)) or its linear approximation (equation (2.6)). Hence,

$$\mathrm{OLR}(T(\theta)) = \begin{cases} A + B \cdot T(\theta) \\ \tau\sigma T(\theta)^4 \end{cases} , \tag{3.10}$$

where the parametrisations by Caldeira and Kasting (1992) (to account for changes in the CO_2 concentration) and by Mcguffie and Henderson-Sellers (2014) (serving comparison purposes) are used for A and B in this chapter.

```
def get_OLR(T, OLR_type, co2=400):
  if OLR_type==”B”:
    sigma=5.67e-8 # W/m^2/K^4,  Boltzmann const
    tau=0.61  # tuned atm transmissivity for OLR
    return sigma*tau*T**4
  elif OLR_type==”LM”:
    # Mcguffie and Henderson-Sellers (2014)
    A_M=-388.74 # W/m^2
    B_M=2.17  # W/m^2/K
    return A_M+B_M*T
  elif OLR_type==”LC”:
    # Caldeira and Kasting (1992)
    from EBM0D import A_cald, B_cald, xi
    A_C=A_cald(co2) #-324.03  # W/m^2 for 400ppm
    B_C=B_cald(co2) #1.94 # W/m^2/K for 400ppm
    return A_C+B_C*T
```

- **AHF $\mathbf{P_{hum}(\theta)}$**: Again, as in the EBM-0D, the most simple way to implement the impact of the anthropogenic heat flux is to add the global average $\langle P_{\text{hum}}\rangle_\theta$ (today $\langle P_{\text{hum}}\rangle_\theta \approx 0.034\,\frac{\text{W}}{\text{m}^2}$) to the energy balance in each latitude band and calculate the resulting change in global mean temperature. However, in order to explore the impact of heterogeneous AHF, this method is compared to a more complex approach, where the AHF is a latitude-dependent Gaussian function. Previous studies calculate the AHF with different proxies: E.g. Flanner (2009) uses energy consumption data for each country and, in order to get a higher 2D-resolution, weights this with the population density within these countries. Chen et al. (2016) uses binned, clear-sky, nighttime lights data from satellites.

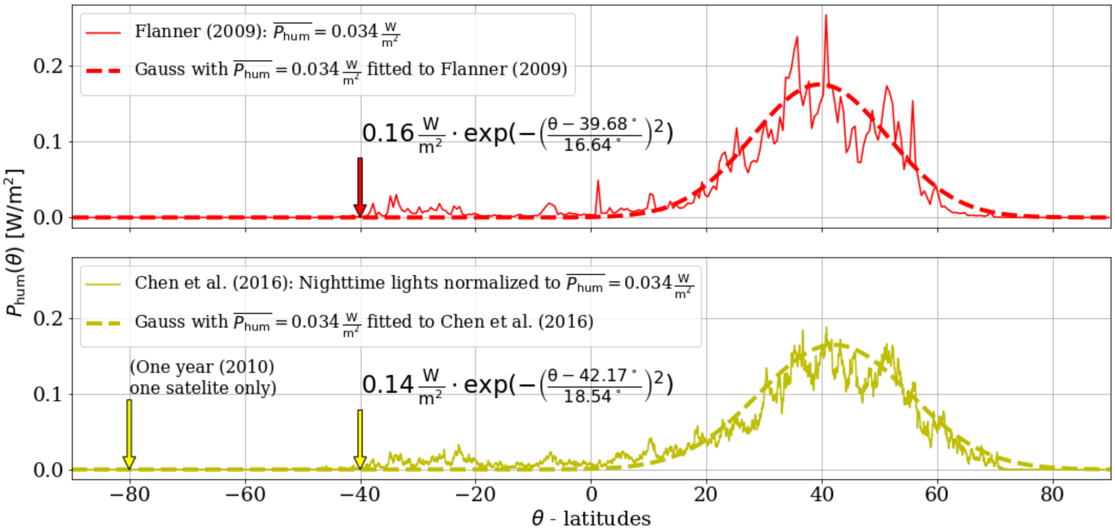

Figure 3.2: $P_{\text{hum}}(\theta)$: Flanner (2009) uses energy consumption data weighted by the population and in Chen et al. (2016) use nighttime lights (here: data from only one year and one satellite used) as a proxy for the AHF. For a simpler parametrisation in the EBM-1D, a Gaussian distribution is fitted to each curve. The upper Gaussian function fitted to the data in Flanner (2009) (later labelled as G_F) is used in the further analysis.

When averaging both of these metrics over all longitudes, a Gaussian distribution can be adequately fitted. Then, this fit needs to be renormalised to the global mean $\langle P_{\text{hum}}\rangle_\theta$, which – as before in the EBM-0D – is retrieved from global 'Energy Use per Capita' data (IEA, 2014) and 'Population' data (The World Bank, 2018). The resulting function for $P_{\mathrm{hum}}(\theta)$ is described by:

$$P_{\mathrm{hum}}(\theta) = \frac{\langle P_{\mathrm{hum}} \rangle_\theta}{N} \cdot e^{-\frac{(\theta-\theta_{\mathrm{mid}})^2}{2\sigma^2}} \quad , \tag{3.11}$$

where N is the normalisation factor.The resulting fitted Gaussian functions at a specific time t, shown in Figure 3.2, are similar for both proxies: The distribution is centred around $\theta_{\mathrm{mid}} \approx 40°$ in the Northern Hemisphere and quite tightly concentrated with a Gaussian width σ of only roughly 17°. Logically, the nighttime-based proxy (lower plot) yields a distribution slightly north of the energy-based proxy with roughly the same Gaussian width. This data set is also more detailed, higher-resolved and smoother than the approach in Flanner (2009) as the latter contains discrete jumps in energy consumption at the borders of countries. Nevertheless, the further analysis of this EBM-1D model uses the fitted Gaussian to Flanner (2009)'s AHF data (labelled as $\mathrm{G_F}$), because this proxy closer resembles the definition of the AHF in this thesis. Also, a similar method is used later in Chapter 4 to retrieve historical 2D data. For comparison, also the previously mentioned distribution (labelled as 'M'), with a global mean value in each cell independent of the latitude, is used.

```
def get_P_hum_distribution(P_glob, P_type):
  if P_type=="M":
    return P_glob+0*m.lats
  elif P_type=="G":
    # The parameters below are from the gaussian fit to the data in Flanner (2009)
    a=0.16180316; b= 39.67767011; c=16.63696653
    distr= a*np.exp(-(m.lats-b)**2/c**2)
    fit_normalized=P_glob/area_mean(distr, m.lats)*distr
    return fit_normalized
```

Flanner (2009) also includes a forecast of the energy production up to 2040. The longitudinally averaged projected distribution slowly shifts southward as the energy production per capita and population in regions around the equator increase. Here, in the analysis of this EBM-1D the distribution is held constant for future projections of global AHF in order to keep the setup simple and easy to reproduce. In Chapter 4, a more elaborate approach based on the SSP scenarios (Kriegler et al., 2017) is described for future projections.

3.2 Implementation

Full Differential Equation. The full (time-dependent) equation for the EBM-1D reads:

$$\begin{aligned} C \cdot \frac{\partial}{\partial t} T(x) \quad &= \quad \frac{S_0}{4}\left(1 - 0.477 \cdot \frac{1}{2}(3x^2-1)\right) \cdot \left(1 - \begin{cases} 0.6 \text{ for } \mathrm{T}|_\mathrm{x} < \mathrm{T_f} \\ 0.3 \text{ for } \mathrm{T}|_\mathrm{x} \geq \mathrm{T_f} \\ 0.6 \text{ for } \mathrm{T}|_\mathrm{x} < \mathrm{T_f} \end{cases} \right) + P_{\mathrm{hum}}(x) \\ &- \begin{cases} (A + B \cdot T(x)) \\ \tau \cdot \sigma T(x)^4 \end{cases} + D \cdot \frac{\partial}{\partial x}(1-x^2)\frac{\partial}{\partial x} T(x) \ , \end{aligned} \tag{3.12}$$

where $x = \sin(\theta)$ and C is a heat capacity, which does not impact the result for the equilibrium $T_{\mathrm{equ}}(x)$ but only influences the time to reach this equilibrium. Here, it is set to $C = 4 \cdot 10^7 \, \frac{\mathrm{J}}{\mathrm{m^2 \cdot K}}$, which could represent either the heat capacity of a 10 m-ocean in a water planet or roughly of the whole atmosphere (see Rose 2017).

```
m.C=4e7 # [J/m^2/K] heat capacity
##### MAIN RUN FUNCTION ####
def run(T_initial, OLR_type, T_f, a0, ai, D_type, P_type, P_mean, co2=400):
  Tf=T_f+273.15 # deg to C
  T=T_initial
  D=get_D(Tf,D_type, OLR_type)
  P_hum=get_P_hum_distribution(P_mean, P_type)
  S=get_S()
  for n in range(0,m.N):
    h = calc_diff(T, D)
    alpha=get_albedo(T, Tf, a0, ai)
    iceline=get_iceline(alpha, ai)
    dTdt=S*(1-alpha) - get_OLR(T, OLR_type, co2=co2)  + h + P_hum
    T=T+ m.dt/m.C * dTdt
  return T, iceline
```

FTCS-method and von Neumann's stability analysis. The diffusion equation (3.12) is numerically integrated via the forward-time-centred-space (FTCS) method. In order to implement the second order derivative, the equation needs to be evaluated at the boundaries of each of the 'original' N latitude bands, at which the temperature of each latitude band is defined. Therefore, an additional (N+1)-grid of the boundaries of the latitude band is initialised in between the original grid points (see Figure 3.3).

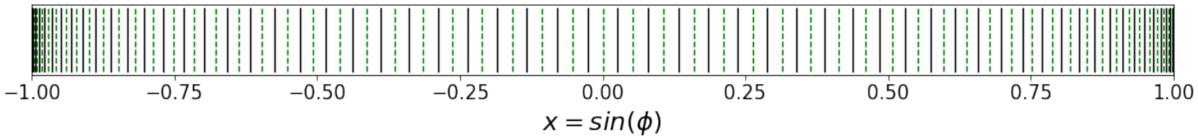

Figure 3.3: The grid for $x = \sin(\theta)$, with the equidistant latitudes θ, for the calculation of equation (3.12). The temperature is evaluated at the 180 black x positions ($-89.5°..89.5°$) and the meridional fluxes are calculated at the boundaries of these cells – the 181 green x^* grid points ($-90°..90°$).

```
  ###   Spatial Grid   ###
  m.Nlats=180    # Nr. of latitudes for T(phi)
  m.lats_star=np.linspace(-90, 90, num=m.Nlats+1) # latidue boundaries
  m.x_star=np.sin(m.lats_star*np.pi/180.)
  m.lats=(m.lats_star[:-1]+ m.lats_star[1:])/2     #latitude bands
  m.x=np.sin(m.lats*np.pi/180.)
  m.dx=np.diff(m.x)
  m.dx_star=np.diff(m.x_star)
```

Furthermore, the FTCS calculation implies a stability criterion. For a typical diffusion equation, $C \cdot \frac{\partial T}{\partial t} = D \cdot \frac{\partial^2 T}{\partial x^2}$, von Neumann's stability analysis indicates that a stable solution can only be found via the FTCS-method if the criterion is fulfilled[1]:

$$\Delta t < \frac{C \cdot \Delta x^2}{2 \cdot D} \tag{3.13}$$

More details of the FTCS-integration and the von Neumann stability analysis can be found e.g. in Press et al. (2007).

---

[1] In order to not let any mode k of the Fourier decomposition of the solution, i.e. $T_j^n = \rho^n \cdot e^{ikx_j}$, where n denotes the temporal and j the spatial index, grow over time, the condition $|\rho^{n+1} \,/\, \rho^n| \leq 1$ needs to be fulfilled. Inserting this into the differential diffusion equation gives a limit on the relation between the temporal Δt and the spatial resolution Δx.

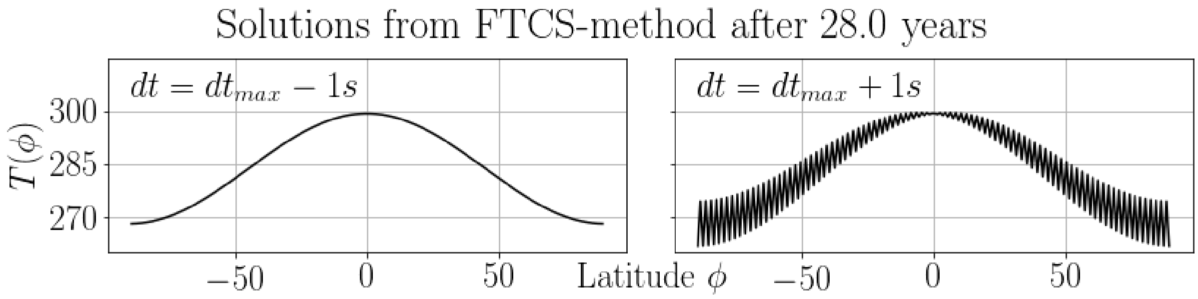

Figure 3.4: Examples for a solution for $T(\theta)$ with an integration time of 28 years that in the left plot fulfils ($\Delta t < \Delta t_{\max}$) and in the right plot breaks ($\Delta t > \Delta t_{\max}$) the von Neumann stability criterion: $\Delta t < \frac{C \cdot \Delta x^2}{D \cdot 2} = \frac{4e7 \cdot \Delta\theta^2}{2 \cdot 0.55} = 11077\,s = 3\,\mathrm{h},\ 4\,\mathrm{min}\,37\,\mathrm{s} = \Delta t_{\max}$.

A physical intuition of this limitation is that the criterion ensures that north- and southward fluxes at each latitude band need to be resolved such that the fluxes can not skip a latitude band in one time step.

The irregular x-grid of equation (3.12) is defined by the underlying regular grid of latitudes (θ) with $\Delta\theta = 1°$. It turns out that the same criterion with $\Delta x = \Delta\theta = const.$ $(= 1° = 1/360 \cdot 2\pi)$ holds for this inhomogeneous and irregular PDE: I.e. if $\Delta t < \frac{C \cdot \Delta\theta^2}{D \cdot 2}$ is broken, the solution $T(\theta)$ becomes instable and diverges after a certain integration time. With e.g. $D = 0.55\,(\mathrm{W/m^2/K})$ and $C = 4 \cdot 10^7\,(\mathrm{J/m^2/K})$ [2] the solution for $T(\theta)$ converges only for time steps $\Delta t \leq 3\,\mathrm{h},\ 4\,\mathrm{min}\,37\,\mathrm{s}$. This has been confirmed by model runs (without ice-albedo feedback) (see Figure 3.4).

```
 ###  Temporal Grid  ###
 m.dt=3600. *1. # [s]  time step for integration
 m.nr_years=15  # [years] integrated until equilibrium
 m.N=int(m.nr_years*3600*24*365 /m.dt) # [s] -"-
```

Furthermore, runs with a finer resolution, e.g. with $\Delta\theta = 0.5°$ and $\Delta\theta = 0.25°$, and accordingly smaller Δt have been performed. Obviously, these results are more distinguished and finer, but, in order to quickly reproduce the results, it was chosen to work with $\Delta\theta = 1°$ unless otherwise stated.

More elaborate approaches like the Runge-Kutta method or implicit methods like Euler backward time integration or the Crank-Nicolson method could be implemented to prevent instability. However, even for the rather fine spatial resolution with $\Delta\theta = 1°$, computation time is not really a limitation in this simple EBM and, therefore, the most simple and straight forward method – the FTCS – is chosen in order to keep up the spirit of quick reproducibility.

3.3 Analysis of the Model

This thesis aims at providing a global view on the effects of the AHF impact. Therefore, the temperatures or temperature changes due to AHF are often globally averaged via:

$$\langle T(\theta) \rangle_\theta = \frac{\sum_{\text{grid cells } \theta} \cos(\theta) \cdot T(\theta)}{\sum_{\text{grid cells } \theta} \cos(\theta)} \tag{3.14}$$

```
def area_mean(variable, lats):
  weights=np.cos(lats*np.pi/180)
  return sum(weights*variable)/sum(weights)
```

---

[2] Typical values for the tuning of the ice-free EBM-1D model (e.g. Rose 2017).

In the following an analysis of the results of the EBM-1D are presented: First, without the ice-albedo feedback, secondly with a variable iceline. In the latter case, the setup of the model requires a more complicated tuning process in order to obtain realistic climate states. The approach taken here and the indications for the stability of the climate state are described and discussed in the first part of Section 3.3.2 and followed with the results together with some sanity checks.

3.3.1 The EBM-1D Without Ice-Albedo Feedback

As a first step of the analysis of the EBM-1D, the ice-albedo feedback is not considered, i.e. the albedo is constant ($\alpha = 0.3$) throughout the latitudes for all times. In this paragraph, the temperature response to the AHF-input is derived and then compared and set in relation to the zero-dimensional EBM-0D from Chapter 2.

Without considering ice, the various EBM-1D configurations (and the corresponding temperature impacts due to the AHF) in this thesis only differ in their OLR parametrisation and in the chosen meridional transport strength D:

- Choosing the **linear OLR parametrisation** (equation (2.6)), the equilibrium global mean temperature of the ice-free model can be calculated analytically. For an equilibrium climate state, all (annual mean) time derivatives in equation (3.12) are zero and, in particular, the meridional transport contribution $h_{\text{equ}}(\theta)$ is constant. Then, the full equilibrium equations for the pre-industrial temperature $T_{\text{pre-industrial}}$ (with $P_{\text{hum}} = 0$) (equation (3.15)) and the 'perturbed' temperature $T'_{\text{linear}} = T_{\text{pre-industrial}} + \Delta T_{\text{linear}}$ (equation (3.16)) yield

$$0 = S(\theta) \cdot (1-\alpha) + h_{\text{equ}}(\theta) - (A + B \cdot T_{\text{pre-industrial}}(\theta))\,. \tag{3.15}$$

$$0 = S(\theta) \cdot (1-\alpha) + h'_{\text{equ}}(\theta) + P_{\text{hum}}(\theta) - (A + B \cdot T'_{\text{linear}}(\theta))\,, \tag{3.16}$$

  where h'_{equ} is the adjusted equilibrium meridional transport contribution to the energy budget. This varies for each cell. However, the global mean average has to vanish in order to maintain radiative equilibrium at the TOA:

$$\langle h_{\text{equ}} \rangle_\theta = \langle h'_{\text{equ}} \rangle_\theta = 0\,. \tag{3.17}$$

  Equivalent to equation (2.12) from the 0D-model before, the global mean temperature increase due to P_{hum} is then given by:

$$\langle \Delta T_{\text{linear}} \rangle_\theta = \frac{\langle\, P_{\text{hum}}(\theta)\,\rangle_\theta}{B}\,. \tag{3.18}$$

  $\langle \Delta T_{\text{linear}} \rangle_\theta$ depends only on the magnitude of the globally averaged P_{hum}, irrespective of both the distribution $P_{\text{hum}}(\theta)$ and the temperature profile (or the meridional heat transport constant D). Obviously, that does not hold for the local temperature changes at a certain latitude: If P_{hum} is inserted e.g. as a Gaussian function (G_F) instead of a constant global mean value (M) at each latitude band, the local temperature strongly depends on D. Exactly as in the EBM-0D, for today's $\langle P_{\text{hum}} \rangle_\theta = 0.034\,\frac{\text{W}}{\text{m}^2}$ the temperature response is $\sim 0.016\,\text{K}$ (for the OLR parametrisation of Mcguffie and Henderson-Sellers 2014). Neglecting numerical differences, this holds irrespective of D. For an increase of today's P_{hum} by a factor of ten, the temperature change is accordingly also ten times higher.

- For the **Boltzmann OLR parametrisation (B)** (equation (2.5)) in the ice-free EBM-1D, the following relations hold for the equilibrium pre-industrial and 'perturbed' climate state, similar to equations (3.15) and (3.16):

$$\begin{aligned}\tau\sigma T^4_{\mathrm{pre-ind.}} &= S(\theta)\cdot(1-\alpha)+h_{\mathrm{equ}}(\theta) &(3.19)\\ \tau\sigma(T_{\mathrm{pre-ind.}}(\theta)+\Delta T(\theta))^4 &= P_{\mathrm{hum}}(\theta)+\frac{S(\theta)\cdot(1-\alpha)}{4}+h'_{\mathrm{equ}}(\theta)\,. &(3.20)\end{aligned}$$

Combining these two equations gives an expression for $\Delta T(\theta)$:

$$\begin{aligned}\tau\sigma(T_{\mathrm{pre-ind.}}(\theta)+\Delta T(\theta))^4 &= P_{\mathrm{hum}}(\theta)+\tau\sigma T_{\mathrm{pre-ind.}}(\theta)^4-\Delta h_{\mathrm{equ}}(\theta) &(3.21)\\ \Delta T(\theta) &= \left(\frac{P_{\mathrm{hum}}(\theta)}{\tau\sigma}+T_{\mathrm{pre-ind.}}(\theta)^4-\Delta h_{\mathrm{equ}}(\theta)\right)^{0.25}-T_{\mathrm{pre-ind.}}(\theta)\,, &(3.22)\end{aligned}$$

where $\Delta h_{\mathrm{equ}}(\theta)=h_{\mathrm{equ}}(\theta)-h'_{\mathrm{equ}}(\theta)$ is the change in the meridional transport contributions due to the additional heat source $P_{\mathrm{hum}}(\theta)$. As in equation (3.17), this also obeys: $\langle\Delta h_{\mathrm{equ}}(\theta)\rangle_\theta=0$. Therefore, by expanding equation (3.22) for small[3] $\Delta h_{\mathrm{equ}}(\theta)$ and taking the global mean, the first order vanishes. I.e. one does not need to calculate Δh_{equ} explicitly in order to get $\langle\Delta T(\theta)\rangle_\theta$ up to first order. In total, the globally averaged temperature difference for the EBM-1D with Boltzmann OLR parametrisation and no ice-albedo feedback from equation (3.22) for small $\Delta h_{\mathrm{equ}}(\theta)$ is:

$$\langle\Delta T(\theta)\rangle_\theta = \frac{\sum_\theta \cos(\theta)\cdot\left(\frac{P_{\mathrm{hum}}(\theta)}{\tau\sigma}+T(\theta)^4\right)^{0.25}}{\sum_\theta\cos(\theta)}-\langle T(\theta)\rangle_\theta+\mathcal{O}(\Delta h^2_{\mathrm{equ}})\,. \qquad (3.23)$$

Imagine an extreme scenario where D is infinitely large, i.e. heat is immediately spread out across the globe. Then, the temperature would be constant over all latitudes. This would resemble the EBM-0D model and the temperature change would be the same as in the chapter before (equation (2.10)). In fact, however, smaller D values describe the climate system more appropriately[4]. In equation (3.23) the additional absolute $\frac{P_{\mathrm{hum}}(\theta)}{\tau\sigma}$ plays a relatively bigger role in colder latitudes than it does in latitudes with a higher temperature. Therefore, the total temperature change increases if the profile is sharper (i.e. small D) or if there is more P_{hum} in colder regions (i.e. for example the Gaussian ($\mathrm{G_F}$) instead of mean (M) P_{hum}-distribution)[5]. To get an idea of the numbers, the equilibrium temperature change that results from $P_{\mathrm{hum}}=0.34\,\frac{\mathrm{W}}{\mathrm{m}^2}$, a tenfold increase of today's value, in this model without ice-albedo feedback and the Boltzmann representation is shown below for different D-values and AHF distributions:

$$\begin{aligned} D=0 \qquad (G_F) \qquad &\rightarrow \Delta\langle T\rangle_\theta = 0.1067\,K &(3.24)\\ D=0.55 \qquad (G_F) \qquad &\rightarrow \Delta\langle T\rangle_\theta = 0.1038\,K &(3.25)\\ D=0.55 \qquad (M) \qquad &\rightarrow \Delta\langle T\rangle_\theta = 0.1032\,K &(3.26)\\ D=\infty \text{ (here } 5) \equiv EBM-0D \quad (M)/(G_F) \qquad &\rightarrow \Delta\langle T\rangle_\theta = 0.1028\,K &(3.27)\end{aligned}$$

These numbers clearly indicate that the above non-linear effects due to the Boltzmann parametrisation of the OLR are negligibly small on a global scale as long as the ice-albedo feedback is not

---

[3] Since P_{hum} is much smaller than all other variables e.g. $S(\theta)$ or $\mathrm{OLR}(\theta)$, the resulting change in h_{equ}, i.e. Δh_{equ}, is also relatively small.

[4] The annual mean temperatures in the Arctic and Antarctic are roughly −15°C and −40°C, which is far from tropical temperatures (see Figure 3.7 later).

[5] Consider the equation (3.23) for one latitude θ^* as a function of the temperature T at θ^*: $\Delta T(T)=(\frac{P}{\sigma\tau}+T^4)^{1/4}-T$ for $P>0$. Its derivative w.r.t. T is then $\partial/\partial T\ \Delta T(T)=(\frac{P}{\sigma\tau}+T^4)^{-3/4}\cdot T^3-1$. This is always negative and converges monotonically to zero. For small $\frac{P}{\sigma\tau}$ the first order of this derivative is $\partial/\partial T\ \Delta T(T)\propto T^{-4}$. I.e. the smaller the initial T at the latitude, the larger the temperature difference due to a small constant P. For large T (or P) this effect vanishes.

considered.

The results can be reproduced using the following code and adjusting D[6] and the model configuration[7]:

```
 T0_noIce=np.array([288 for theta in m.x])
 global_D=0.55
T,XX= run(T0_noIce, ”B”, 0, 0.3, 0.3, ””, ”G”, 0.00)
T_P,XX= run(T0_noIce, ”B”, 0, 0.3, 0.3, ””, ”G”, 0.340)
 print(”Run without ice-albedo-feedback: dT_mean=”+’%.5f’ % (area_mean(T_P-T, m.
   lats)))
```

3.3.2 The EBM-1D With Ice-Albedo Feedback

Having analysed the ice-free EBM-1D in the last section, the full model as given in equation (3.12) is now considered including changing albedos and a variable iceline. Due to this ice-albedo feedback, more thought needs to be put into the tuning process and the set-up of the model in order to obtain a realistic climate state.

Configuration of the Model. The EBM-1D gives range to multiple degrees of freedom: The choice of the OLR parametrisation via A, B (linear) or τ (Boltzmann), the albedo values for ice-free (α_0) and ice-covered cells (α_i) together with the freezing temperature T_f, the initial temperature T_0, which determines the initial ice extent, and, finally, the meridional transport constant D.

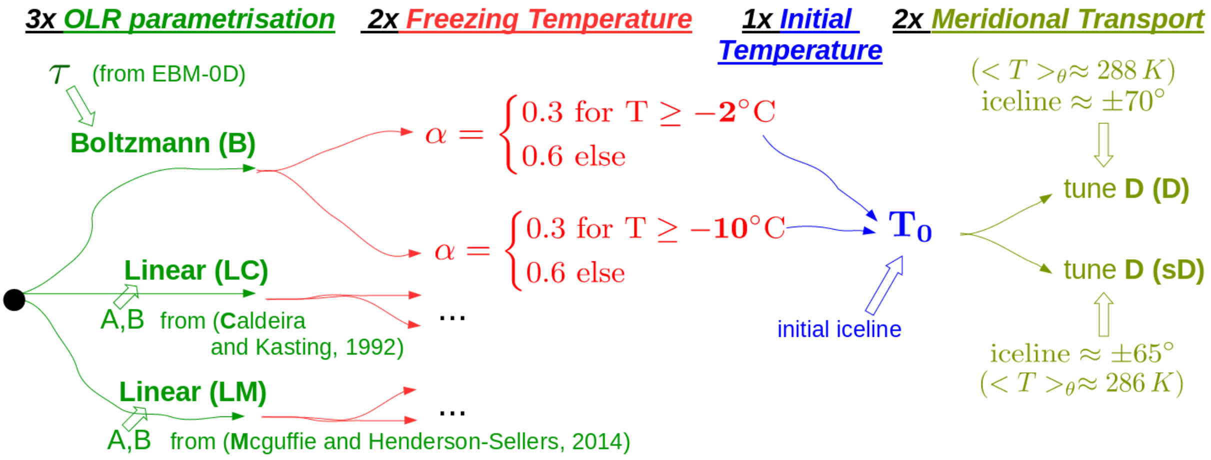

Figure 3.5: Decision tree of the tuning process used in this analysis. From left to right: Three choices for the OLR parametrisation, two for the freezing temperature (i.e. the definition of albedo), the fixed initial temperature profile, which ensures that the earth does not immediately settle in a hothouse or snowball state, and the final tuning of the meridional transport constant D to two different sets (normal (D) and small (sD)) of the variable(s) ‘iceline’ (and ‘global mean temperature’). In total twelve configurations of the EBM-1D are investigated here. Additionally, the distribution of the P_{hum}-input ((M) or (G_F)) can be chosen. For the CO_2-dependent parametrisation (LC) the concentration is fixed at 400 ppm for all runs.
An overview of all model configurations is given in Table 3.1.

One might try to tune the parameters in such a way that today’s climate conditions (e.g. the exact local temperature profile across the latitude bands) are sufficiently close to observations. However, such

---

[6] Note that for larger D values the step size needs to be adjusted to fulfil the stability criterion.

[7] Or simply by uncommenting lines 166-176 in EBM1D_main.py.

an over-tuning would perhaps imply a false accuracy in view of the simplicity of this model. In fact, depending on the control variables (like the global mean temperature), it can be impossible to retrieve today's climate conditions in equilibrium in this model with a given OLR and albedo parametrisation.

The approach in this thesis (described by the sketch in Figure 3.5) is to take reasonable and established values for the OLR parametrisation (as mentioned before: three choices) and the freezing temperature (two choices) together with the previously stated fixed albedo values. The initial temperature profile is chosen as a second order Legendre Polynomial $T_0 = T(t = 0) = (280 - 20 \cdot (\frac{1}{2}(3 \cdot \sin(\theta)^2 - 1)))\,\mathrm{K}$ [8] (fixed), which is chosen such that, without external influences, the equilibrium state results in neither the ice-free nor the hothouse state. The idea of the last step of the setup procedure is to tune the meridional transport constant in order to retrieve the state, whose global mean temperature and iceline are sufficiently close to $\langle T \rangle_\theta \approx 288\,\mathrm{K}$ and iceline $\sim \pm 70°$ in the equilibrium state (first choice for D). However, in most cases analysed here the global mean temperature of $\langle T \rangle_\theta \approx 288\,\mathrm{K}$ is only reached in a hothouse planet. To avoid this and to make iceline shifts in general better comparable, only the iceline variable is chosen as a tuning goal, irrespective of $\langle T \rangle_\theta$. Eventually, the final D value is picked 'by hand', given the information shown in Figure 3.6. This means that, if a different OLR parametrisation or freezing temperature is chosen, the tuning process results in entirely different equilibrium climate states, which can differ strongly e.g. in their equator-to-pole temperature gradient.
An overview of all model configurations used in this analysis is given later in Table (3.1).

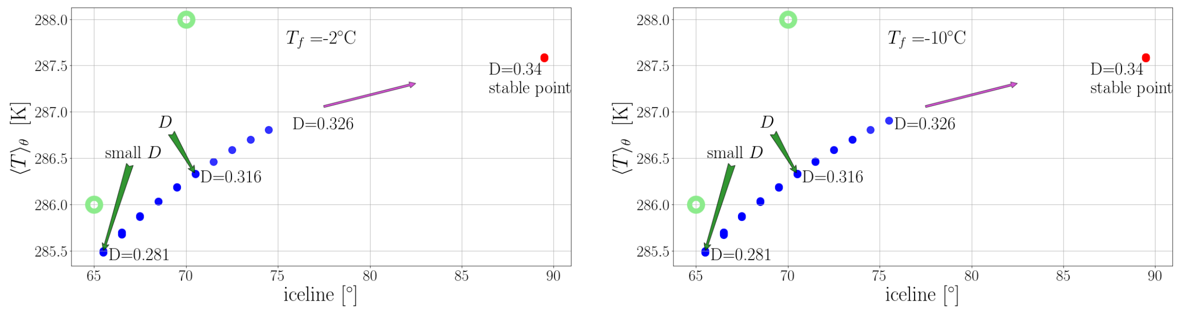

(a) $T_f = -2\,°\mathrm{C}$

(b) $T_f = -10\,°\mathrm{C}$

Figure 3.6: Tuning of the meridional transport constant D in the model with Boltzmann OLR parametrisation for different freezing temperatures T_f. None of the configurations can be tuned to have $\langle T \rangle_\theta = 288\,\mathrm{K}$ and iceline $= 70°$. Hence, the parameter setting with iceline $= 70°$ was chosen (green arrow with 'D'). For comparison, also a more stable model configuration with a smaller D value is analysed (green arrows with 'sD'), which is tuned to get iceline $= 65°$ (and roughly $\langle T \rangle_\theta = 286\,\mathrm{K}$). For very large D-values all settings result in a hothouse state (red dots in the upper right corner) without any ice.

It turns out that this method has a major flaw: Figure 3.6 shows the tuning step for a model with the Boltzmann OLR parametrisation for both freezing temperatures. The resulting states in both cases, which were tuned to an iceline $= 70°$ (and $\langle T \rangle_\theta \approx 288\,\mathrm{K}$), are relatively close to an instable state on the verge of becoming completely ice-free. In general, this is especially true for models with the higher freezing temperature $T_f = -2°\mathrm{C}$ (left plot), which are more sensitive to becoming a hothouse planet as the temperature profile is more flat and, therefore, temperatures near the poles are not much smaller than the freezing temperature in comparison to the models with $T_f = -10°\mathrm{C}$.

Therefore, an additional setting with a smaller meridional transport constant is investigated, in order to get a more stable system. Instead of tuning to the iceline $= 70°$, a new tuning goal, iceline $= 65°$

---

[8] Comparable to Rose (2017) but with different values.

(corresponding to roughly $\langle T \rangle_\theta \approx 286\,\mathrm{K}$), is chosen. Subsequently, also the meridional transport constant decreases (giving a second option for choosing D): For example for the Boltzmann OLR parametrisation, runs with $D = 0.665$ for $T_f = -2\,°\mathrm{C}$ and $D = 0.281$ for $T_f = -10\,°\mathrm{C}$ are additionally investigated here (see also Figure 3.6).

Another approach (e.g. in Rose 2017) would be to tune D such that the equator-to-pole temperature difference ($\Delta T_{\mathrm{equator-to-pole}}$) matches the observed $\sim 45\,\mathrm{K}$ and the maximum meridional heat flux $H_{\max} \approx 5.5\,\mathrm{PW}$. However, this is not pursued here.

An example of a full model configuration is shown in the following code segment with the values for D, which were picked in the previous tuning process for all configurations:

```
####    Choose Model Configuration    ####
# OLR
OLR_type=”B”  # ”B”,”LM” or ”LC”

# ALBEDO/ICE
T_f=-10      # -10 or -2
a0=0.3  # ice free albedo
ai=0.6  # ice albedo

# INITIAL CONDITION
T0=280-20*(0.5*(3*m.x**2-1))  # initial Temperature

# TUNED D VALUES for all (OLR_type, D-type+T_f)-combinations
D_type=”D”  # ”D” or ”sD”
def get_D(Tf, D_type, OLR_type): # overwriting the previous simple function.
    D_B={”D-2”:0.69 , ”sD-2”:0.665 , ”D-10”:0.316 , ”sD-10”:0.281 }
    D_LM={”D-2”:0.7985, ”sD-2”: 0.791, ”D-10”:0.418 , ”sD-10”:0.395 }
    D_LC={”D-2”:0.792, ”sD-2”:0.787 , ”D-10”:0.433 , ”sD-10”:0.415 }
    if OLR_type==”B”:
        return D_B[D_type+str(T_f)]
    if OLR_type==”LM”:
        return D_LM[D_type+str(T_f)]
    if OLR_type==”LC”:
        return D_LC[D_type+str(T_f)]

# AHF DISTRIBUTION
P_type=”M”  # ”G” or ”M”
```

If the resolution of the grid cells is increased (e.g. $\Delta\theta = 0.5°$ instead of $\Delta\theta = 1°$) the resulting climate states differ and a new tuning of the model would be required in order to meet the tuning target. However, this represents a new model configuration and, hence, models with different resolutions can not be directly compared.

Overview of Model Parameters Used. In total, this tuning process gives twelve different model setups which are investigated in this thesis:

Name	OLR	T_f [°C]	merid. transp. const. D		P_{hum}
			D	sD	distribution
(B (D/sD) $_{-2}$)	$0.61 \cdot \sigma T^4$	-2	0.69	0.665	(M), (G$_{\text{F}}$)
(B (D/sD) $_{-10}$)		-10	0.316	0.281	(M), (G$_{\text{F}}$)
(LC (D/sD) $_{-2}$)	$-324.03\,\frac{\text{W}}{\text{m}^2} + 1.94\frac{W}{m^2K} \cdot T$	-2	0.792	0.787	(M), (G$_{\text{F}}$)
(LC (D/sD) $_{-10}$)		-10	0.433	0.415	(M), (G$_{\text{F}}$)
(LM (D/sD) $_{-2}$)	$-388.74\,\frac{\text{W}}{\text{m}^2} + 2.17\frac{W}{m^2K} \cdot T$	-2	0.7985	0.791	(M), (G$_{\text{F}}$)
(LM (D/sD) $_{-10}$)		-10	0.418	0.395	(M), (G$_{\text{F}}$)

Table 3.1: Overview of model parameters used in this analysis. The parameters $\alpha_0 = 0.3$, $\alpha_i = 0.6$ and the initial condition T_0 are the same for all runs. The chosen parameters for the linear OLR parametrisation are taken from Mcguffie and Henderson-Sellers (2014) (LM..) and Caldeira and Kasting (1992) (LC..) (with fixed $CO_2 = 400\,\text{ppm}$ for all runs). The Boltzmann (B..) representation includes the tuned atmospheric transmissivity $\tau = 0.61$ from the previous chapter. Additionally, to the first D-value (..D), a **s**maller meridional transport constant D (..sD) is evaluated.
The AHF is inserted either as global **m**ean value for all latitudes (M) or as a latitude dependent **G**aussian distribution (G$_{\text{F}}$) (fitted to Flanner 2009's data as described above).

All model configurations behave differently in response to the AHF input, with some being more realistic for our current climate than others. However, as stated before, the EBM-1D is only a conceptual model to better understand feedbacks and processes and its implications for real world climate remains limited. Figure 3.7 shows a comparison of $T(\theta)$ in the (LMD/sD$_{-10}$) model for the different D values and further compares this with the annual and longitudinal mean temperature $SST_{\text{skin}}(\theta)$ from NCEP Reanalysis 2 data for the years 1979-2017. But again, due to the crudeness of the model, good agreement with measured data is not necessarily an indicator for a good model or a good parameter setting.

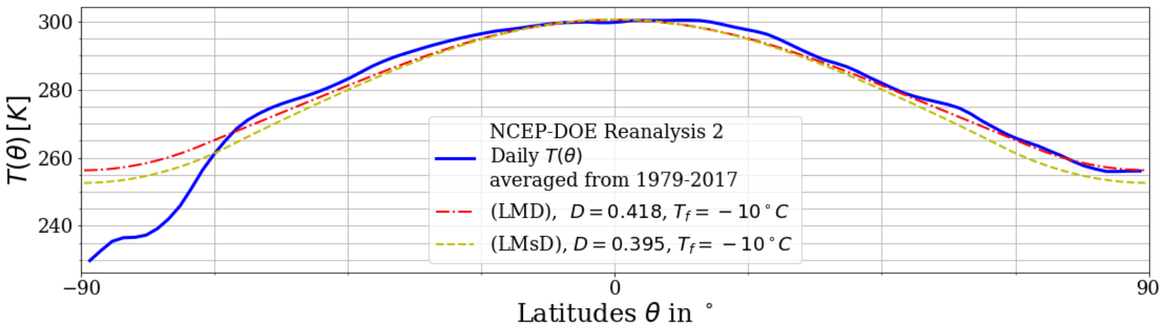

Figure 3.7: Annual mean temperature $T(\theta)$ of a model (including ice-albedo feedback) with Mcguffie and Henderson-Sellers (2014)'s linear OLR parametrisation with tuned D (LMD$_{-2,\,-10}$) and smaller D (LMsD$_{-2,\,-10}$) (see Table 3.1) in comparison with the mean sea-surface skin temperature‘ SST_{skin}’ from NCEP Reanalysis 2 from 1979 to 2017 (NOAA ESRL PSD, 2017).

To What Degree Can the Numbers in These Models Be Trusted? In the following, a simple test is performed to get a sense of the relevance/trustworthiness of these model configurations. The additional P_{hum}-term in equation (3.1) is now interpreted as the total radiative forcing due to human activity. This forcing is of course mainly governed by the increase of CO$_2$-concentration in the atmosphere, but up to first order this greenhouse effect is also simply a positive net radiative forcing originating from human activity. Hence, by inserting $P_{\text{hum}} = 2.6\,\text{W/m}^2$ or $P_{\text{hum}} = 4.5\,\text{W/m}^2$ (both as a global mean distribution (M)) into equation (3.12) and integrating until equilibrium is reached, one can compare the temperature responses to the ones retrieved from GCM-simulations for the same values of radiative forcing since pre-industrial times. According to the IPCC (2013), these forcings give rise to a temperature change of $\Delta T_{2.6\,\mathrm{W/m^2}} = 1.0\,\mathrm{K}\,(\pm 0.7\,\mathrm{K})$ and $\Delta T_{4.5\,\mathrm{W/m^2}} = 1.8\,\mathrm{K}\,(\pm 0.7\,\mathrm{K}))$ until 2100 (not in equilibrium), respectively.

For nearly all configurations in the EBM-1D these (high) forcings trigger the earth to become completely ice-free. If this happens, the temperature response is around $2 - 4.5\,^\circ\mathrm{C}$ for the $2.6\,\mathrm{W/m^2}$-forcing and $2.5 - 5.5\,^\circ\mathrm{C}$ for the $4.5\,\mathrm{W/m^2}$-forcing depending on the model configuration. Only in the configuration (BsD_{-10}) some latitude bands still have temperatures smaller than the freezing temperature $T_f = -10\,^\circ\mathrm{C}$ for both forcings[9]. The temperature response for this setting is $1.30\,^\circ\mathrm{C}$ (with a 3°-shift of the icelines ($\pm 65.5^\circ \rightarrow \pm 68.5^\circ$)) for the $2.6\,\mathrm{W/m^2}$-forcing and $2.62\,^\circ\mathrm{C}$ (with a 9°-shift of the icelines ($\pm 65.5^\circ \rightarrow \pm 74.5^\circ$)) for the $4.5\,\mathrm{W/m^2}$-forcing, respectively. Hence, this test reveals the quite unsurprising conclusion that the most conservative configuration of the EBM-1D in this thesis (BsD_{-10}) agrees the most with standard climate models. Especially the high freezing temperature of $T_f = -2\,^\circ\mathrm{C}$ and too high D-values produce a very instable system that easily settles in a hothouse state and yields in strongly exaggerated temperature responses to external forcings like P_{hum}.

Note though, the assumption in this test – that radiative forcing can be inserted as additional anthropogenic heat – is definitely oversimplified[10].

The Impact of the AHF Under a 2%-Growth Scenario. The previous analysis of the EBM-1D without the ice-albedo feedback in Section 3.3.1 suggests that there is not much difference between the one-dimensional and the zero-dimensional EBM with respect to the global mean temperature impact. However, the crucial change to the EBM-0D in this one-dimensional extension, as already shown in the description of the tuning process, is, in fact, the ice-albedo feedback, which is investigated in the following.

Figure 3.8 shows the time series of the global mean temperature and the iceline (South/North) in the (LMD_{-10})-model due to a 2%-increase per year of P_{hum} ($\mathrm{G_F}$). The spatial resolution in all following models is 1°.

It should be noted again, that this model configuration is quite instable w.r.t. turning the earth into a hothouse planet as shown in Figure 3.6. Therefore, the rate of ice melting might be strongly exaggerated. Initially, the system is in an equilibrium state with $P_{\mathrm{hum}}(\theta) = \mathrm{normalised\_gaussian}(\theta) \cdot 0.034\,\frac{\mathrm{W}}{\mathrm{m}^2}$, where the normalised_gaussian(θ) is the distribution from ($\mathrm{G_F}$) from equation (3.11). The system then adjusts dynamically to the increasing AHF, i.e. there is a loop of (1) increasing the AHF by a factor of 1.02 and (2) integrating for one year[11] (referred to as ‘Transient run’). The model adjusts quickly to changes in P_{hum} and the iceline. Additionally, an ‘Equilibrium run’, where, after each (1) jump of the AHF, (2) the system is integrated until it reaches equilibrium (here 15 years are chosen), is shown in transparent colours in Figure 3.8. However, this ‘Equilibrium run’ does not give significantly different results compared to the ‘Transient run’, except for a sharpening of the curves and a significant deviation in the response in the case, when the Northern Hemisphere becomes completely ice-free (year 120), since there is no instable state in the ‘Equilibrium run’.

After 130 years, which is randomly chosen, the AHF is set to zero in order to test reversibility. One might e.g. imagine that after that time the civilisation has found a way to dump all anthropogenic heat to space

---

[9] Reproduce these numbers by running EBM1D_main.py but adjusting the model configuration and P_hum_glob variable accordingly.

[10] So is the EBM-1D itself.

[11] Again, there are only annual mean values and no seasonal differences, i.e. the time of integration does not have a physically relevant meaning.

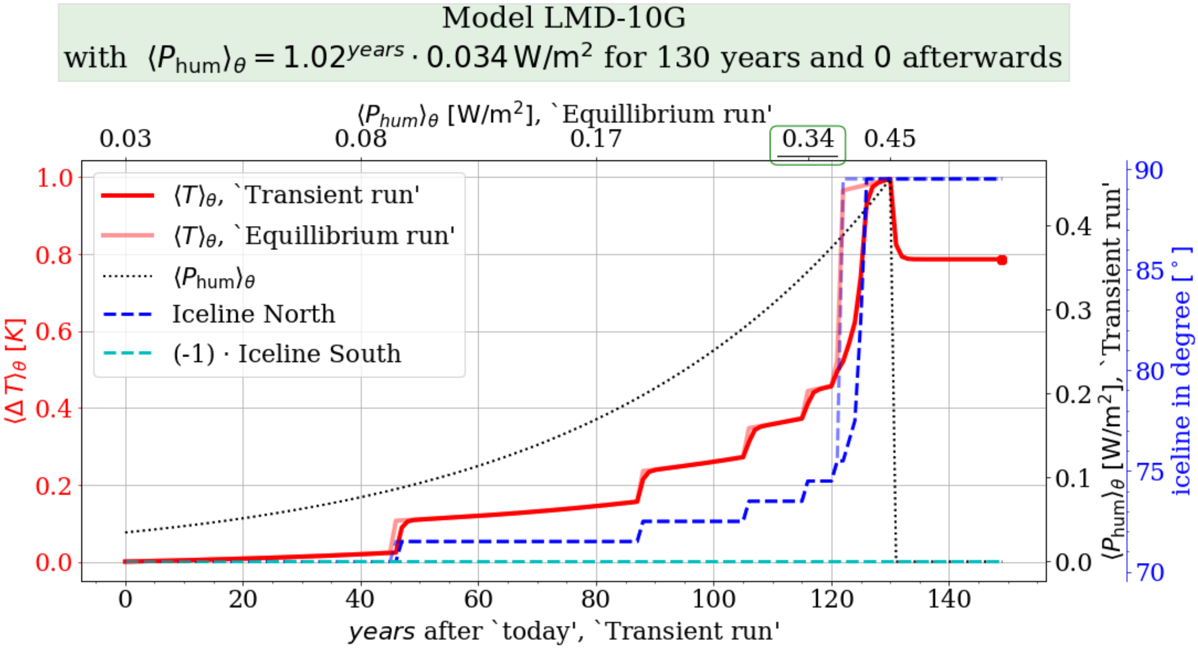

Figure 3.8: Change of global mean temperature and iceline (South/North) for the model (LMD$_{-10}$). The AHF is inserted according to the fitted Gaussian distribution (G$_\mathrm{F}$). Initially, the system is in equilibrium with $\langle P_{\mathrm{hum}}\rangle_\theta = 0.034\,\frac{\mathrm{W}}{\mathrm{m}^2}$ in year 0. Then, P_{hum} increases dynamically with 2% per year ('Transient run'). After roughly 125 years, the ice disappears completely in the Northern Hemisphere (i.e. iceline = 89.5°). After 130 years P_{hum} is set to zero in order to show the irreversibility of the ice melting effects of P_{hum} in the EBM-1D. Also shown in transparent colours is an 'Equilibrium run' of the same model, in which each of the previous P_{hum} jumps is brought into equilibrium (the top x-axis shows the P_{hum} values; these correspond to the ones shown in the 'Transient run' with the time axis at the bottom). Note, this method is later used to compare all model configurations for the given $P_{\mathrm{hum}} = 0.34\,\mathrm{W/m^2}$ (indicated by the green box).

directly without warming the atmosphere[12]. The simulation can be reproduced via EBM1D_timeseries.py.

After ca. 45 years of increasing P_{hum} the iceline in the Northern Hemisphere shifts one latitude band (1°) northwards due to the increased local temperature. Through the positive ice-albedo feedback, the global mean temperature jumps whenever the iceline changes.

A finer grid would smooth the iceline curve and, therefore, also the temperature changes. However, next to the previously mentioned problem of comparing different models due to different D values from the tuning, this would also require a much longer computation time due to the stability criterion of the diffusion equation (see equation (3.13)) and yield qualitatively the same result.

When the anthropogenic heat emissions stop for whatever reason ($\langle P_{\mathrm{hum}}\rangle_\theta = 0$ after 130 years here), which implies a negative net energy balance at the TOA, the global mean temperature in the models that do not consider ice-albedo feedback (EBM-0D and EBM-1D with fixed albedo), would drop back to pre-industrial values. Here, considering the ice-albedo feedback, the temperature drops by the exact amount that accounts for the *direct* heating from the AHF (here: $\sim 0.2\,\mathrm{K}$). However, the ice melting process is irreversible because at the initial iceline the local decrease in albedo creates a new equilibrium state for this multi-stable latitude band. The whole Earth System in this model has therefore settled into a new equilibrium state itself and a net change in global temperature (in Figure 3.8: $\Delta\langle T_{\mathrm{equ}}\rangle_\theta \approx 0.8\,°\mathrm{C}$) is maintained even though $P_{\mathrm{hum}} = 0$ at that time.

---

[12] Or humankind is dead.

For a certain large P_{hum}-input the system turns into a hothouse planet. This is known as the 'small ice cap instability' and is a feature of this specific setup of the EBM-1D (e.g. North 1984). In the time series in Figure 3.8 the Northern Hemisphere ice disappears after roughly 120 years. Then, an entirely new global climate equilibrium is generated that inhibits ice-building even via a (moderate) artificial global cooling process.

Comparison of Results From Models With Different Configurations for a Tenfold Increase of the AHF. In the following, equilibrium runs of different model configurations for a given fixed P_{hum} are investigated instead of the full time series, i.e. one value at a specific $\langle P_{\mathrm{hum}}\rangle_\theta$ (green box) of the more transparent red curve, the 'Equilibrium run', in Figure 3.8. As in Chapter 2 before, a tenfold increase for today's AHF is chosen: $\langle P_{\mathrm{hum}}\rangle_\theta = 0.34\,\frac{\mathrm{W}}{\mathrm{m}^2}$, i.e. $10 \cdot P_{\mathrm{hum}}$ (2010).

ΔT(θ) - Temperature Response Over Latitudes. In Figure 3.9 the local equilibrium temperature changes over all latitudes θ due to the (instantaneously) increased $\langle P_{\mathrm{hum}}\rangle_\theta$ are plotted for different configurations of the model[13]. Initially, the system is again in equilibrium with $\langle P_{\mathrm{hum}}\rangle_\theta = 0.034\,\frac{\mathrm{W}}{\mathrm{m}^2}$ ($\mathrm{G_F}$). The data in Figure 3.9 can be obtained by running EBM1D_T_profiles.py for the different configurations.

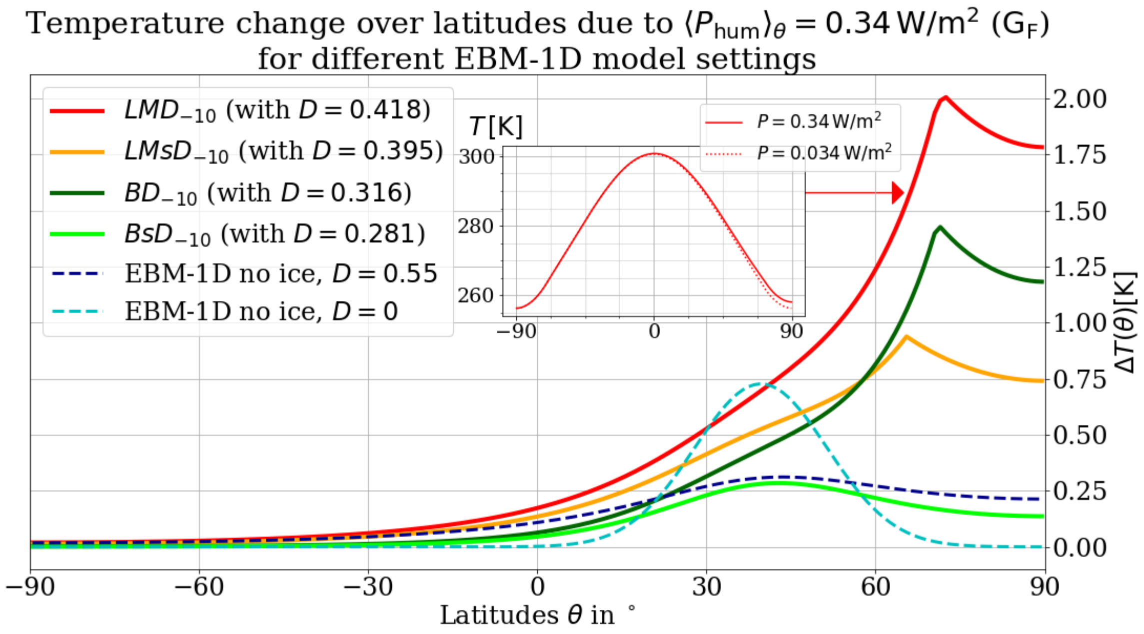

Figure 3.9: Equilibrium-$\Delta T(\theta)$ for different models and parameter settings due to the AHF with a Gaussian distribution ($\mathrm{G_F}$) and $\langle P_{\mathrm{hum}}\rangle_\theta = 0.34\,\frac{\mathrm{W}}{\mathrm{m}^2}$. The reference is the equilibrium temperature profile with $\langle P_{\mathrm{hum}}\rangle_\theta = 0.034\,\frac{\mathrm{W}}{\mathrm{m}^2}$ (also ($\mathrm{G_F}$)). The blue dashed lines are model runs without ice (i.e. constant $\alpha = 0.3$) with different D's, the green lines use the Boltzmann parametrisation (BD_{-10} and BsD_{-10}), the red and yellow (LMD_{-10} and $LMsD_{-10}$) the linear OLR parametrisation with Mcguffie and Henderson-Sellers (2014)'s A and B values. For the yellow and light green line a smaller meridional transport constant was chosen. As shown later, for BsD_{-10} the iceline remains constant and, hence, $\Delta T(\theta)$ resembles the characteristics of a model without ice. Also shown in the subplot are the initial (dashed) and final (solid) actual temperature profiles for the setting (LMD_{-10}) in the red curve.

One can clearly observe that the temperature increases strongly around the North Pole, where ice is melting and, therefore, more solar radiation is absorbed due to the decreased albedo. The maximum of

---

[13] Again, this is equivalent to holding anthropogenic heat emissions constant after 116 years of 2%-growth in the time series of the equilibrium run in Figure 3.8.

the temperature difference is **not** at the peak of the P_{hum}-input, but instead at the latitude of the most recent iceline.

If a system results in an ice-free Northern Hemisphere due to the anthropogenic heat emissions, the temperature increase is much higher and strictly monotonically increasing until the North Pole because the jump of the albedo no longer exists in this case (not shown here).

$\langle \Delta \mathbf{T} \rangle_\theta$ - Global Mean Temperature Changes. Similar to the ice-free analysis in Section 3.3.1, the change in equilibrium, global average temperature due to the tenfold increase of AHF $\langle P_{\text{hum}} \rangle_\theta = 0.34 \, \frac{\text{W}}{\text{m}^2}$ is simulated. The model is again initialised in equilibrium for today's $\langle P_{\text{hum}} \rangle_\theta = 0.034 \, \frac{\text{W}}{\text{m}^2}$. The full results showing the temperature impact and the shifting of the icelines for all model configurations of Table 3.1 are summarised in the Appendix A.3 in Table 7.2, which can be reproduced via the following code:

```
# RESULTS WITH ICE
OLR_type=”B”; T_f=−10; D_type=”sD”; P_type=”G”; P_glob_today=0.034
T_today,iceline_today= run(T0, OLR_type, T_f, a0, ai, D_type, P_type, P_glob_today)
print(OLR_type+D_type+str(T_f)+” (”+P_type+”, P_glob=”+str(P_glob_today)+”): <T>_theta=
    ”+’%.4f’ % area_mean(T_today, m.lats) +”, icelines:”+str(iceline_today[0])+”, ”+str(
   iceline_today[1]))
P_glob_10x=0.34
T_10x,iceline_10x= run(T_today, OLR_type, T_f, a0, ai, D_type, P_type, P_glob_10x)
print(OLR_type+D_type+str(T_f)+” (”+P_type+”, P_glob=”+str(P_glob_10x)+”): <T>_theta= ”
  +’%.4f’ % area_mean(T_10x, m.lats) +”, icelines:”+str(iceline_10x[0])+”, ”+str(
   iceline_10x[1]))
print(”Difference <T_10x − T_today>_theta = ”+’%.6f’ % area_mean(T_10x−T_today, m.lats)
   )
```

To run all configurations at once, another program is provided on GitHub (EBM1D_table_tenfoldP.py).

Depending on the choice of OLR parametrisation and the setting of the parameters, the icelines in the Northern and Southern Hemisphere can

- stay constant: When the iceline does not change, there's no ice-albedo feedback and the temperature responses are very similar to the results from the ice-free EBM-1D or the EBM-0D. Examples are ($\text{BsD}_{-10}\text{G}_\text{F}$/M)) in Table 7.2 or Figure 3.9. In general, this is the case for very small meridional transport constants D and, hence, more stable systems. Also, the Boltzmann parametrisation (B..) tends to have less shifting of the iceline compared to the linear approach, due to the sub-linear temperature response as described before.

- shift in one or both hemispheres: Via the direct AHF-effect the local temperature can rise such that it exceeds the melting threshold at the specific latitude of the iceline. Here, the distribution of the AHF input ((G_F) or (M)) can play a crucial role. For the localised Gaussian P_{hum} this effect sets in earlier but only for the Northern Hemisphere, leading to an initially larger global mean temperature increase. However, the temperature response of the mean P_{hum}-distribution (M) 'catches up' in this model since it melts ice on both sides of the planet simultaneously, which leads to a large temperature change at later times (e.g. ($\text{BsD}_{-2}(\text{G}_\text{F})$) vs. ($\text{BsD}_{-2}$(M)) or ($\text{LMD}_{-10}(\text{G}_\text{F})$) vs. ($\text{LMD}_{-10}$(M))). In general, though, the global mean temperature changes for different P_{hum} distributions are quite similar, as long as the ice itself does not completely vanish in any of the hemispheres.

- disappear in both or one hemisphere: Depending on the stability of the system and the OLR parametrisation the AHF input can even trigger the previously mentioned small ice-cap instability in these models. If the iceline exceeds ca. ±75°, the ice disappears completely in this hemisphere (see also Figure 3.5). In the runs with $T_f = -2\,°\mathrm{C}$ and linear OLR parametrisation (L(C/M)(D/sD)$_{-2}$(G$_\mathrm{F}$/M)), the ice disappears on both sides leading to a temperature change of roughly 2 to 3 K. Even if P_hum is inserted as a Gaussian in the Northern Hemisphere the ice in the south melts in most of these cases due to the large global mean temperature increase from the ice-albedo feedback in the northern polar region. For the Boltzmann parametrisation with a large D value (BD$_{-2}$(G$_\mathrm{F}$)), only the ice in the North Hemisphere disappears completely, but the temperature increase arising from this does not trigger the ice in the south to tip over but shifts this iceline by 'only' 1° (one latitude band). If P_hum is inserted evenly in the same configuration (BD$_{-2}$(M)), however, the ice covered areas disappear on both sides and the temperature change is 0.5 K larger than in the (G$_\mathrm{F}$)-run. In contrast to this, in the (LCD$_{-10}$(G$_\mathrm{F}$))-run the ice in the north melts due to the localised P_hum, whereas for the (LCD$_{-10}$(M)) in both hemispheres the iceline shifts by 'only' 3° (just below the tipping point), leading to a smaller temperature change (by roughly 0.5 K).

Is the complete disappearance of the ice in general a realistic climate scenario? The 'ice' in the EBM-1D is an annual and bimodal parameter that adjusts quickly to temperature changes. Its real world analogy could perhaps be a parameter that states whether sea ice exists during more than 50% of the year and in more than half of the latitude band.

The tipping of the Arctic sea ice has been subject to a large debate in the climate science (e.g. Lindsay and Zhang 2005 and Holland, Bitz, and Tremblay 2006). Most GCMs do not show a complete disappearance of the Arctic sea ice in the 21st century even under business-as-usual scenarios (Lenton et al., 2008). However, Lenton et al. (2008) conclude that 'a *summer* ice-loss threshold, if not already passed, may be very close and a transition could occur well within this century'. Staying under the 2 °C-threshold of the Paris Agreement might prevent the tipping of summer sea ice in the Arctic (Schellnhuber, Rahmstorf, and Winkelmann, 2016). Note that the ice sheets in Greenland or Antarctic or the winter sea ice in the Arctic have much higher (local) warming thresholds for tipping than the Arctic summer sea ice (Schellnhuber, Rahmstorf, and Winkelmann, 2016).

The direct temperature impact of the increase in the AHF simulated in the EBM-1D here is much smaller than these thresholds. Still, especially in configurations with the linear OLR parametrisation (L..) and a high melting temperature ($T_f = -2\,°\mathrm{C}$), which are in general very sensitive to the insertion of the AHF, the ice vanishes completely due to the tenfold increase of P_hum (see Table 7.2) [14] . These models clearly overestimate the instability of the system.

Again, as in the simple test before and somehow consistent with common sense, the most plausible configurations are unsurprisingly the (conservative) ones with Boltzmann parametrisation and/or small freezing temperature $T_f = -10\,°\mathrm{C}$ (especially (BsD$_{-10}$) and (BD$_{-10}$)). The results indicate again that the tuning and, hence, the stability of the system towards changes in the iceline is crucial for the temperature response. Here, the global mean temperature increase for plausible configurations ranges from roughly 0.10 K (BsD$_{-10}$) to 0.46 K (LMD$_{-10}$) depending on how much the iceline is shifted.

Later in this thesis, the results from the climate model of intermediate complexity are compared to the

---

[14] Anyway, the time-scale of such a complete ice-loss would also be much larger than in the simulations of the EBM-1D above especially in regions with glaciers or ice-sheets due to their inertia.

scenarios ($\mathrm{BsD}_{-10}(\mathrm{G_F})$) and ($\mathrm{BD}_{-10}(\mathrm{G_F})$)). Therefore, these results are extracted from Table 7.2 and shown here:

Model Configuration	$\langle\mathbf{\Delta T}\rangle_\theta$	**initial →final iceline [south, north]**
($\mathrm{BD}_{-10}(\mathrm{G_F})$)	$\mathbf{0.219}\,°\mathrm{C}$	$[-70.5, 70.5] \to [-70.5, 72.5]$
($\mathrm{BsD}_{-10}(\mathrm{G_F})$)	$\mathbf{0.096}\,°\mathrm{C}$	$[-65.5, 65.5] \to [-65.5, 65.5]$

Table 3.2: Some especially relevant results from the EBM-1D with variable iceline extracted from Table 7.2 in the Appendix A.3.

So far, the spatial resolution of these runs has been $\Delta\theta = 1°$. If the spacing is decreased to $\Delta\theta = 0.5°$, keeping the same parameter choices, i.e. the initial iceline is not necessarily near its tuning target but the model configuration remains the same, the results are as follows[15]

Model Configuration	$\langle\mathbf{\Delta T}\rangle_\theta$	**initial →final iceline [south, north]**
($\mathrm{BD}_{-10}(\mathrm{G_F})$)	$\mathbf{0.203}\,°\mathrm{C}$	$[-71.75, 72.25] \to [-71.75, 74.25]$
($\mathrm{BsD}_{-10}(\mathrm{G_F})$)	$\mathbf{0.140}\,°\mathrm{C}$	$[-65.25, 65.25] \to [-65.25, 65.75]$

Table 3.3: The same relevant EBM-1D model configurations with variable iceline as in Table 3.2, but now with a smaller spatial resolution (0.5°). However, the parameter D is kept constant and is **not** tuned to obtain an iceline of 70° or 65° in contrast to the models with $\Delta\theta = 1°$ resolution.

The iceline of the most conservative configuration, ($\mathrm{BsD}_{-10}(\mathrm{G_F})$), which was constant in the model with 1° resolution, now shifts by 0.5° (one grid cell) in the Northern Hemisphere under a tenfold increase of the AHF. The temperature change is accordingly slightly higher. For ($\mathrm{BD}_{-10}(\mathrm{G_F})$) the initial icelines deviate from the previous model. The shift in the northern iceline is still 2°, however.

Amplification for Simultaneous $\mathbf{CO_2}$-Increase Again, as in Chapter 2, the last step of the analysis deals with the simultaneous increase of CO_2 and AHF and a potential feedback process.

The CO_2-dependency of the OLR parametrisation by Caldeira and Kasting (1992) is used to investigate the amplification of the temperature response for simultaneous P_{hum}- and CO_2-growth. Because of the high initial instability of the ice in the model, the runs with smaller D values and $T_f = -10\,°\mathrm{C}$ (LCsD_{-10}) are chosen for this amplification analysis. Doubling the CO_2 concentration still leads to a hothouse planet in those more conservative model configurations. Therefore, 'only' a 50% increase of the CO_2 concentration in 2010 is simulated:

Nr.	$\mathbf{CO_2}$	$\langle\mathbf{P}_{\mathrm{hum}}\rangle_\theta$	$\langle\mathbf{\Delta T}\rangle_\theta$	**initial →final iceline [south, north]**
(0)	388 ppm	$0.034\,\mathrm{W/m^2}$	–	$[-65.5, 65.5] \to [-65.5, 65.5]$
(1)	582 ppm	$0.034\,\mathrm{W/m^2}$	2.3 K	$[-65.5, 65.5] \to [-72.5, 72.5]$
(2)	388 ppm	$0.34\,\mathrm{W/m^2}$	0.3 K	$[-65.5, 65.5] \to [-65.5, 67.5]$
(3)	582 ppm	$0.34\,\mathrm{W/m^2}$	3.3 K	$[-65.5, 65.5] \to [-73.5, 89.5]$

Table 3.4: Different ($\mathrm{LCsD}_{-10}(\mathrm{G_F})$)-runs (as described in Table 3.1) with $T_f = -10\,°\mathrm{C}$ and $D = 0.415$ for (1) a 50%-increase of CO_2 run, (2) a $P_{\mathrm{hum}} = 10 \cdot P_{\mathrm{hum}}$ (2010)-run, and (3) a run with simultaneous increases of CO_2 and P_{hum}[16]. Initial conditions are: $CO_2 = 388\,\mathrm{ppm}$ (const. in run (2)), $\langle P_{\mathrm{hum}}\rangle_\theta = 0.034\,\frac{\mathrm{W}}{\mathrm{m^2}}$ (const. in run (1)). The temperature differences are with respect to this reference run (0).

---

[15] Reproduce this by running EBM1D_table_tenfoldP.py with the parameters Nlats = 360 and dt decreased by a factor of 4.

These results can be reproduced by running the code in EBM1D_co2_amplification.py.

Table 3.4 shows that the simultaneous growth of CO_2 and $P_{\rm hum}$ leads to a much larger global mean temperature ($\approx 0.7\,$K) than the sum of both impacts individually due to the ice-albedo feedback. As discussed before in equation (2.15) and Appendix A.2, the amplification from simultaneous CO_2 and $P_{\rm hum}$-increase is tiny and, hence, cannot explain this result. The reason for the large amplification here is of a different nature: The growth in CO_2 concentration can push the (initially stable) climate system to a more and more instable state, where the additional forcing from the heterogeneous $P_{\rm hum}$ impact transgresses a threshold and triggers the ice in the Northern Hemisphere to melt, thereby, amplifying the global mean temperature increase through the ice-albedo feedback.

In this special case, the effect of the simultaneous increasing $P_{\rm hum}$ leads to a large-scale global climate change, that a model without the AHF forcing cannot simulate.

3.4 Comparison of the EBM-0D and EBM-1D, Summary, and Discussion

EBM-0D. The simple EBM-0D presented in this thesis in Chapter 2 gives a rough, but analytical estimate for the impact of the AHF. The current global mean equilibrium temperature increase for the AHF produced by the human civilisation in 2010 is 0.010 K according to this basic model. If the Boltzmann parametrisation is replaced by a simpler, linear approximation, the impact grows to roughly 0.016 K. Given continued exponential growth of the AHF, this temperature impact consequently rises exponentially, too. E.g. a tenfold increase of the AHF leads to a temperature increase of 0.092 K in the EBM-0D with Boltzmann parametrisation (equation (2.14)).

The model itself as well as the assumptions of future AHF projections in this chapter certainly do not aim to forecast a realistic quantitative temperature increase. However, the calculation still gives a quick orders of magnitude estimation of the potential temperature increase from anthropogenic heat emissions. It makes the case that the AHF can become a relevant process on a global to consider when thinking about future energy growth scenarios.

EBM-1D. More elaborately, the one-dimensional EBM, discussed here, describes a latitude-dependent climate system with the possibility to include the ice-albedo feedback arising from the anthropogenic forcing.

Without ice, the model mostly resembles the EBM-0D. However, if the AHF changes the amount of ice-cover in one or both hemispheres the temperature impact is strongly amplified. The two most realistic model configurations investigated here are ($\mathrm{BsD}_{-10}(\mathrm{G_F})$) and ($\mathrm{BD}_{-10}(\mathrm{G_F})$), which yield a temperature rise of 0.096 K (without a shift of the iceline) and 0.219 K (with 2° shift of the iceline in the Northern Hemisphere), respectively, for a tenfold AHF forcing, where the spatial resolution is $\Delta\theta = 1^\circ$. If the spatial resolution is increased to $\Delta\theta = 0.5^\circ$, the ($\mathrm{BsD}_{-10}(\mathrm{G_F})$)'s iceline in the Northern Hemisphere shifts by 0.5°, resulting in a global mean temperature increase of 0.14 K.

The EBM-1D presented here is relatively instable with respect to turning the system into a hothouse planet. This instability depends on the strength of the meridional transport, the OLR parametrisation

---

[16] Strictly speaking, since a smaller CO_2 concentration was chosen here (388 instead of 400 ppm) than in the previous analysis of the EBM-1D, the tuning process should have been repeated for the new OLR parametrisation. However, the small difference does not seem to affect the iceline of the initial run (0), which is still ±65.5°.

and the freezing temperature. For some of the model configurations presented here – especially those with the linear OLR parametrisation, a large meridional transport constant, or a warm freezing temperature – a tenfold increase of the AHF-forcing leads to a complete disappearance of ice in one or both hemispheres. Hence, a careful interpretation of the results presented here is required.

When CO_2 is increased simultaneously to the AHF, a negligible positive feedback enhances the temperature impact. More importantly, though, the AHF can 'push' the system, which is already destabilised through the growing greenhouse effect, over a threshold and trigger, for example, the disappearance of the ice in certain circumstances.

In summary, a simple model like the EBM-1D emphasises that the ice-albedo feedback is crucial for estimating limits of the global mean temperature response of future energy production scenarios.

While certainly describing the Earth System in more detail than the EBM-0D, the EBM-1D still lacks important features like a proper simulation of the radiation transfer in a (vertically resolved) atmosphere, circulation (i.e. a physically more accurate description of the meridional heat transport), cloud feedbacks and the influence of land and ocean, vegetation (to name a few). Especially the ocean as a long-term heat sink is an important feature not considered in this analysis.

The EBM-1D, presented in this chapter, nevertheless expands the understanding of the main processes of the climate system when an external heat source is introduced and helps to better estimate the nature of its impact.

Chapter 4

The AHF in the Earth System Model of Intermediate Complexity CLIMBER-3α

So far in this thesis, the climate impact of the AHF has been estimated through conceptual Energy Balance Models, that can easily be reproduced in a few lines of code. In the following, the AHF is investigated in a climate model of intermediate complexity, in particular, 'CLIMBER-3α' (CLIMBER in the following) developed by Montoya et al. (2005).

4.1 Components and Setup of CLIMBER-3α

The structure of the model is illustrated in Figure 4.1. It consists of a statistical-dynamical atmosphere module, 'POTSDAM-2', with a grid resolution of 22.5° in longitude and 7.5° in latitude. The details of the calculation are similar to the predecessor model CLIMBER-2, which is described in (Petoukhov et al., 2000). In a nutshell, the model assumes universal vertical temperature and humidity profiles, while the dynamic and radiative fluxes of the atmosphere are calculated at certain height levels (10 or 16 layers, respectively). Hence, the atmosphere is referred to as '2.5-dimensional'. The calculation includes many processes of GCM-calculations (Montoya et al., 2005) but cannot e.g. explicitly calculate phenomena on a synoptic scale.

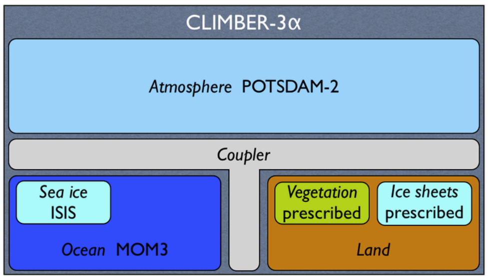

Figure 4.1: The different modules of 'CLIMBER-3α' adopted from `https://www.pik-potsdam.de/research/earth-system-analysis/models/climber/climber3`.

CLIMBER's 3D modular ocean general circulation model, 'MOM3', has a resolution of 3.75° in longitude and latitude and 24 vertical layers. The manual in Pacanowski and Griffies (1999) provides details about the calculation of the ocean dynamics. The specific setup is described in Montoya et al. (2005). Furthermore, another module, 'ISIS' (Fichefet and Maqueda, 1997), calculates the dynamics of sea ice (one layer) and snow (one layer) .

In CLIMBER, each cell of the surface layer of the atmosphere, which is based on the Biosphere-Atmosphere Transfer Scheme (BATS) (Dickinson et al., 1986), contains fractions of the following surface types (labelled as 'ntp'): open water, sea ice, trees, grass, desserts, glaciers.

Model Initialisation and Forcing. The model is forced via yearly solar irradiance input (i.e. through fluctuations of the solar constant at the TOA, the influence of volcanic or anthropogenic aerosols on the incoming short-wave radiation, and land-use changes) as well as the yearly concentration of the global greenhouse gases CO_2, N_2O and CH_4. In the following, the forcing from this will be called CO_2-equivalent- or, simply, CO_2-forcing. The exact derivation of the radiative forcings arising from these two contributions and the sources for external data are described in Appendix A.4.

For all following results, a simulation run from Feulner (2011) is used. At first, that run has been initialised and brought into equilibrium for base conditions of $CO_2 = 277\,\text{ppm}$ and a solar constant of $S_0 = 1361\,\frac{\text{W}}{\text{m}^2}$. Furthermore, with historic forcing reconstructions for the last millennium a pre-industrial state (here the year 1810) is obtained. In this section the new forcing from anthropogenic heat flux AHF is added to CLIMBER as an additional forcing term after the year 1810. The derivation of the data used for this additional forcing in each grid cell is explained below in Section 4.2 for both historic data and future projections. A description of the implementation of the AHF in CLIMBER follows in Section 4.3 and, finally, the results especially regarding the surface temperature impacts and the ice-albedo-feedback are presented in Section 4.4.

4.2 Preparation of the AHF Data

In the analysis of the EBMs in Chapters 2 and 3, the AHF-forcing is inserted either as a simple global mean estimate or – in the one-dimensional case – as a Gaussian distribution depending on the latitude. Since CLIMBER is a spatially-resolved 2D model, the heterogeneity of the energy production and consequent heat emissions across the planet can be taken into account.

Main Assumptions. Due to this thesis' strive for simplicity and reproducibility as well as the availability of data, simple methods and estimates need to be chosen to retrieve the AHF input data. In particular, the following assumptions are made:

- Energy is produced and used only in the surface types grass, desserts and trees (not on sea-ice, ocean, or glaciers).
- Energy is used and dissipates as heat at the same location where it was produced.
- Energy use density is homogeneous in the specific world regions, which will be defined later. Hence, every square meter with a potential for AHF-emission (grass or tree land or dessert) within a specific region emits the same amount of forcing in W/m^2.

- All primary energy production immediately results in *additional* heat input into the atmosphere (irrespective of the energy source). As before, this is of course strongly simplified[1]. A discussion follows in Chapter 5.
- Before 2010, historical data is used for both the CO_2 concentration and aerosol concentration as described before. Afterwards, the projected future energy production only increases the AHF forcing but does not change the GHG or aerosol concentrations, except for the last paragraph, in which the amplification due to simultaneous CO_2 increase is investigated.

4.2.1 Historic Data

World Regions. The World Bank and the IEA provide estimates of the total population (The World Bank, 2018) and the annual primary energy production per capita (in oil equivalent units) (IEA, 2014), respectively, in several world regions: 'Europe and Central Asia' ('eca'), 'Middle East and North Africa' ('mena'), 'Sub-Saharan Africa' ('ssa'), 'South Asia' ('sa'), 'East Asia and Australia' ('eap'), 'North America' ('na'), 'Latin America and Carribean' ('lac') and the whole 'World' ('w'). Via the previously used calculation in equation (2.8), these data sets are converted to yearly 'Primary Energy Production' data for all regions. Most estimates for the primary energy production are available from 1971 up to 2014 (at the moment). Each cell containing a non-zero land fraction (which is not covered by glaciers) in the CLIMBER grid is assigned by hand to one of these world regions (see Figure 4.2a). Due to the coarse resolution of 22.5° in longitude and 7.5° in latitude, this method is somewhat arbitrary, but for the purpose of this study it is not necessary to capture all details of the heterogeneity of the AHF.

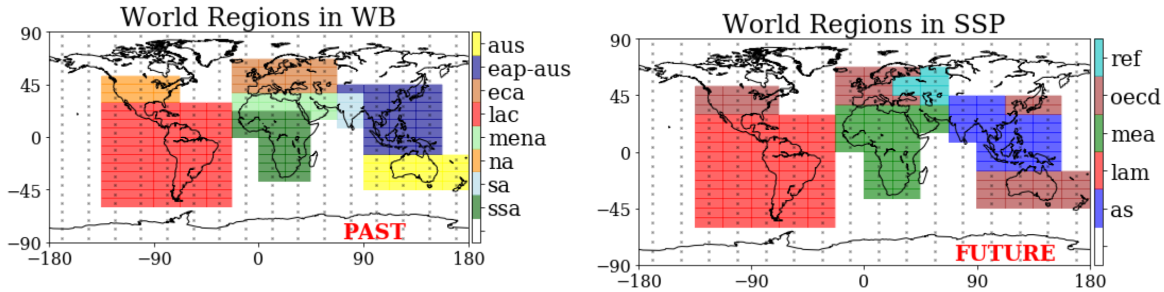

(a) Defined 'region matrices' in the data in IEA (2014) and The World Bank (2018) (WB) used for the past AHF reconstruction.

(b) Defined 'region matrices' in the data in the SSP-scenario used for future AHF projection.

Figure 4.2: 'region_matrix': The chosen allocation of the cells in CLIMBER to the world regions, which are defined, firstly, by IEA (2014) and The World Bank (2018) (left) and, secondly, by the SSP scenario (Kriegler et al., 2017) (right), which is later used for future projections. By multiplying the power used in these areas divided by the total size of the land fraction of the region, the P_{hum} input for every cell is generated. In the CLIMBER simulation, the constant P_{hum} values in each cell are weighted by the land fraction Fr_{land} (see also Figure 4.4). Here, the artificial adjustments of the region_matrix that are described in the main text like the additional separation of Australia from East Asia are already in place.

Calculation of the Forcing Map. After defining the regions on the CLIMBER grid, the total primary energy produced in each year is evenly 'spread out' across the assigned land of the region. The following equations give the AHF forcing (in W/m^2) in each cell (with latitude *lat* and longitude *lon*) for the CLIMBER simulation runs. The full code can be found in create_historic_Phum_files.py.

---

[1] E.g. cooling water from power plants is usually discharged into rivers, which then directly heat up the ocean near the estuary area and not the atmosphere.

For all regions, 'reg', a matrix describing the fraction of potential P_{hum} emission in every cell is defined and calculated via:

$$\text{potential\_P}_{\text{hum}}\text{\_area\_matrix}_{\text{reg}}\,(lat,\ lon) = \text{region\_matrix}_{\text{reg}}\,(lat,\ lon)\ \cdot\ \text{Fr}_{\text{land}}\,(lat,\ lon) \cdot (1 - \text{glacier\_fraction}\,(lat\,,lon))\ , \tag{4.1}$$

where $\text{region\_matrix}_{\text{reg}}\,(lat,\ lon) = \begin{cases} 1 \text{ if cell is assigned to region reg} \\ 0 \text{ else} \end{cases}$ (compare with Figure 4.2a). The land fraction Fr_{land} multiplied by $(1 - \text{glacier\_fraction})$ gives the fraction of trees, grass, and desserts in each cell. As none of the cells, where P_{hum} is potentially emitted has a significant glacier fraction, this will just be called land fraction Fr_{land} in the following.

Finally, the $\text{potential\_P}_{\text{hum}}\text{\_area\_matrix}\,(lat,\ lon)$ and $\text{region\_matrix}(lat,\ lon)$ are then used to get the forcing for the cells in the region:

$$P_{\text{hum, reg}}\,(lat, lon) = \frac{\text{region\_matrix}_{\text{reg}}\ \cdot\ P_{\text{reg}}\,[\text{W}]}{\sum_{\text{lat, lon}} \text{potential\_P}_{\text{hum}}\text{\_area\_matrix}_{\text{reg}}\ \cdot\ \cos(lat)\ \cdot\ \delta lat\ \cdot\ \delta lon\ \cdot\ r^2_{\text{earth}}\,[\text{m}^2]}\ , \tag{4.2}$$

where the denominator is the size of the region in m^2, in which the AHF is emitted (with the earth radius $r_{\text{earth}} = 6371\,\text{km}$), and P_{reg} is the primary power in the specific region calculated from the yearly data in W as described above. Applying this mechanism to all regions and summing up the contributions gives a P_{hum}-matrix for the whole world, in which the $P_{\text{hum}}\,(lat,\ lon)$ values are the same in all cells of a specific regions (which looks similar to Figure 4.2). Averaging this matrix, together with the land fraction Fr_{land} yields the same global average as used before in Chapters 2 and 3: $\overline{P_{\text{hum}}(2010) \cdot \text{Fr}_{\text{land}}} = 0.034\,\text{W/m}^2$.

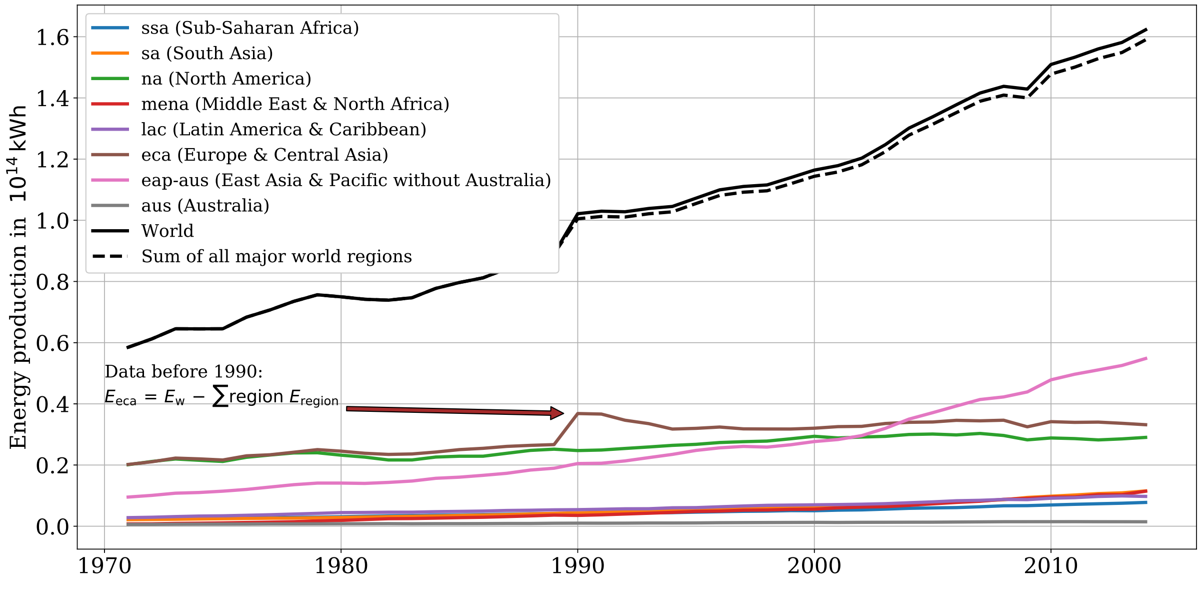

Figure 4.3: Historic primary energy production data for several world regions from IEA (2014) and The World Bank (2018).

Additional Assumptions. At some points additional adjustments are necessary in order to make this method more realistic:

- The energy produced in the region 'Europe and Central Asia' is assigned only to Europe and East

Central Asia, i.e. all heat emission inputs from cells east of $67.5°E$ longitude are set to zero and the energy production of 'Europe and Central Asia' is distributed evenly on the land fraction in the reduced area.

- The energy produced in the region 'North America' is assigned only to USA and South Canada, i.e. all heat emission inputs north of $52.5°N$ latitude are set to zero and the energy production of 'North America' is distributed evenly on the land fraction in the reduced area.
- During the 2000s energy production in 'East Asia and Australia' increased strongly, especially due to developments in China and East Asian countries. Hence, the aggregation 'eap' overestimates the AHF in Australia. This is solved, by subtracting the Australian energy usage from the given data of the region 'eap' and creating separate world regions 'Australia' ('aus') and 'East Asia without Australia' ('eap-aus').

The data retrieved from The World Bank for all world regions is shown in Figure 4.3 as a function of time. For the world region 'Europe and Central Asia' there is no data available until 1990 after the dissolution of the UdSSR. Hence, the data before 1990 for this world region is derived by subtracting the sum of all other region's energy production from the data of the total 'World'. Furthermore, note that the sum of all world regions (after 1990) (covering the whole world population) adds up to only $\sim 98\%$ of the world primary energy production. The remaining 2% are most likely invalid or insufficient data, which gives rise to uncertainties in the 'Energy per Capita' data. Therefore, the P_{hum} values in all cells are multiplied by a 'renormalisation' factor in order to obtain the global value for P_{hum} in the code (or equation (4.2)).

For the years before 1971, where data is not or only partially available, a simple growth of 2% per year of the energy production is assumed and the distribution between the world regions is kept constant at the 1971 shares.

The Resulting $\mathbf{P_{hum}}$ Forcing Map. Figure 4.4 shows the heterogeneous input of P_{hum} forcing (multiplied by Fr_{land}) in the year 2010. The three main contributions are from Northern America, Europe and Central Asia and the East Pacific region (especially since the 2000s).

Note, though, that every m^2 of land in a specific world region emits the same forcing. For comparison, the longitudinal mean of this data is plotted in the right part of Figure 4.4 together with the Gaussian distribution (G_F) from the EBM-1D in Section 3 that was fitted to data from Flanner (2009). Except for some deviation around the equator, where the simple Gaussian function underestimates the AHF, the two distributions contain the same features. This justifies the simplification of the Gaussian distribution for the longitudinally averaged, one-dimensional EBM in equation (3.11) in Chapter 3.

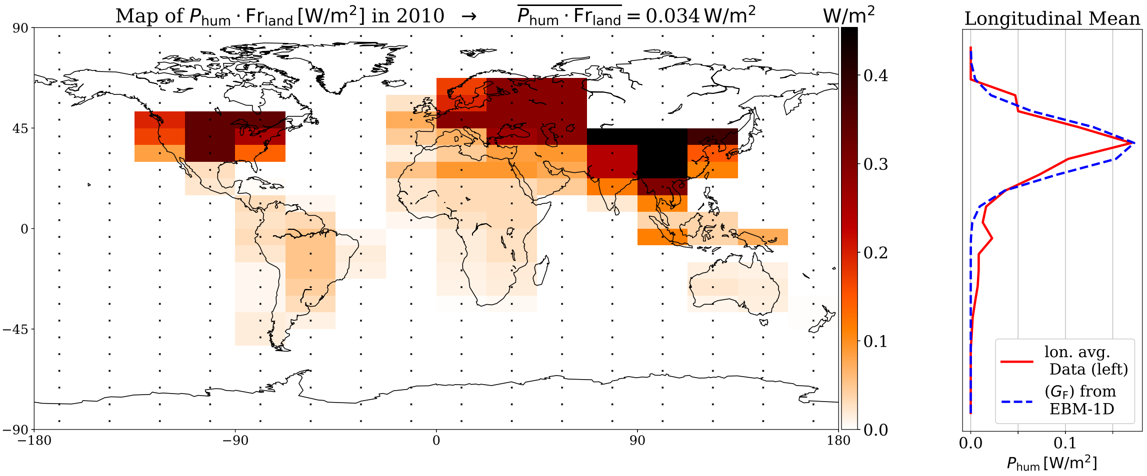

Figure 4.4: Example of the heterogeneous P_{hum} input in the year 2010 from the data in IEA (2014) and The World Bank (2018). The P_{hum} forcing is defined on land only. Therefore, the forcing is weighted with the land fraction $\mathrm{Fr}_{\mathrm{land}}$ in this plot in order to illustrate the actual forcing contribution to the energy balance in each cell. In the right plot, the longitudinal mean of this data is compared to the previously used Gaussian distribution in the one-dimensional EBM, which is fitted to data from Flanner (2009).

4.2.2 Future Projections

Trying to estimate future anthropogenic heat flux is challenging for two reasons: Firstly, the (heterogeneous) energy production of future civilisations is subject to a lot of discussion (see Chapter 6), but also the non-trivial relation between additional heat injection and the share of energy sources is debatable. Again, Chapter 5 will go into more detail and distinguish between different energy sources. Here, the same assumption as in the EBMs in Chapters 2 and 3 is made, i.e. that all energy produced is emitted as additional energy into the atmosphere. Here, two scenarios for the evolution of the total primary energy production are investigated:

- **2% - growth:**
  As before, the continuation of a 2%-growth in energy production can be assumed as a first-guess, ‘business-as-usual’ scenario. For further simplicity, the energy share among the world regions is kept fix at the 2010 values derived from the data in IEA (2014) and The World Bank (2018). This approach serves the purpose of quickly illustrating the impact of continued energy production growth without having to think about complex interrelationships like the co-evolution of human societies, population size and energy production, which is discussed further in Chapter 6.

- **SSP5**:
  The Shared Socio-Economic Pathway scenarios[2] provide more elaborate estimates for future energy production as well as emissions of greenhouse gases, population size, etc. based on current socio-economic factors. Here, the most energy-intensive scenario family, i.e. SSP5, is chosen in order to investigate a ‘worst-case scenario’ with respect to the AHF. The SSP5 scenario is characterised by ‘rapid and fossil-fueled development with high socio-economic challenges to mitigation and low socio-economic challenges to adaptation’ (Kriegler et al., 2017) and is associated with strong economic growth, which is supported by energy intensive production. Here, the ‘baseline’ scenario without any climate policy is investigated[3]. Among other developments, the global energy demand, as well

---

[2] The data set can be downloaded from `https://tntcat.iiasa.ac.at/SspDb/dsd?Action=htmlpage&page=welcome`

[3] However, policies, which solely regard the reduction of greenhouse gas emissions but not the amount of energy pro-

as the CO_2-concentration, triple in this scenario until the end of the century and the radiative forcing reaches up to $8.5\,\mathrm{W/m^2}$. Population peaks at 8.6 billion around 2055 and falls back to 7.4 billion by 2100, which drives the saturation of energy production by the end of the century. For the purpose of this first study, however, only the primary energy production is used, while all other concentrations or parameters (except for the solar constant) are kept at their 2010 levels as described before in Section 4.2. This specific extraction of the SSP5-baseline scenario is called the $\widetilde{\text{SSP}}$5-baseline in this thesis.

The SSP-data uses a different aggregation of countries to world regions than in the previously used data from The World Bank (2018) and IEA (2014): ‘Asia’ (‘as’), ‘Latin America’ (‘lam’), ‘Middle East & Africa’ (‘mea’), ‘OECD’ (‘oecd’), and ‘Reforming States’ (‘ref’). The assignment of the SSP-world regions to the climber cells is shown in Figure 4.2b and can be compared with Figure 4.2a. The data of historic and future primary energy consumption in the past and future is illustrated in Figure 4.5.

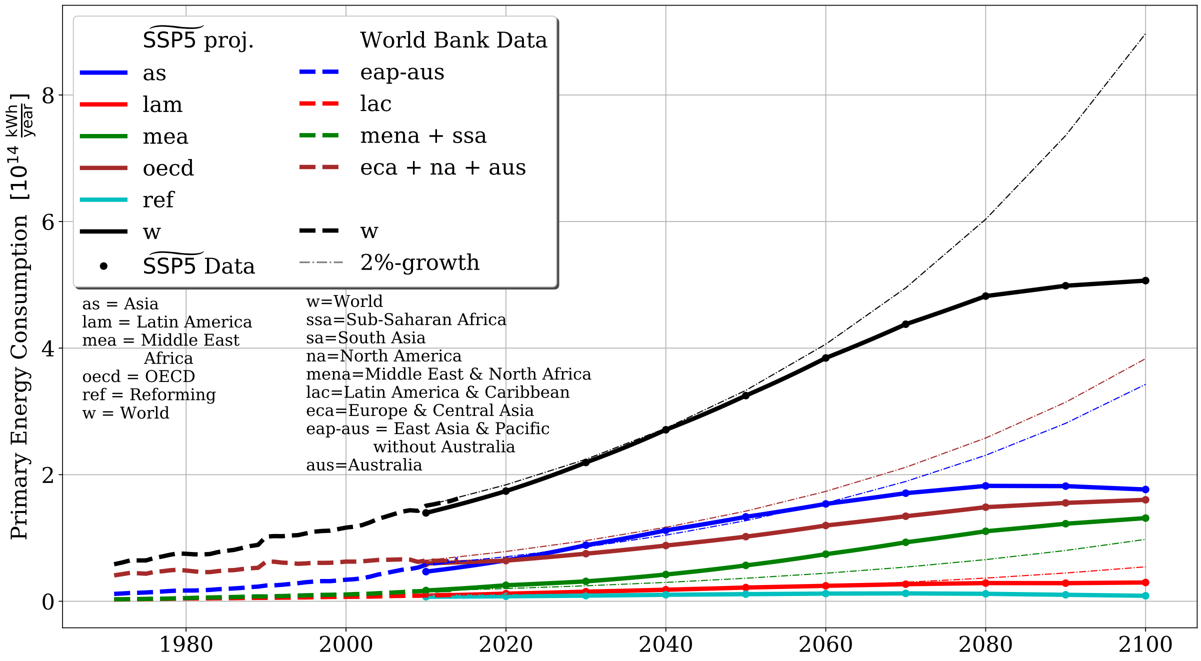

Figure 4.5: Primary Energy Production over time for different world regions. Historic data from IEA (2014) and The World Bank (2018) and future projections of (1) a 2%-growth per year in all regions or (2) the $\widetilde{\text{SSP}}$5-baseline scenario (Kriegler et al., 2017) (only the dots; lines in between are interpolated). Some of the regions from the World Bank data have been aggregated for this figure in order to compare the data with the $\widetilde{\text{SSP}}$5-baseline scenario. However, the regions plotted in the same colours are not necessarily the same (e.g. Japan is missing in ‘eca’+‘na’+‘aus’ compared to ‘oecd’).

Due to the differences in the aggregation of the regions the transition from one data set to the future projections in the year 2010 is not trivial in this case:

- Method **‘direct’**: First, one can use the ‘real’ $\widetilde{\text{SSP}}$5-baseline data and accept jumps in the local data between 2010 and 2011. Large P_{hum} jumps occur especially in the ‘Reforming States‘(‘ref’), which is distinguished from Europe in the SSP-aggregation, in ‘Australia’ (‘aus’) and Japan, which are clustered together with other ‘oecd’-states in SSP, and in ‘South Asia’ (‘sa’), which is incorporated in ‘Asia’ (‘as’) in SSP. Furthermore, as shown in Figure 4.5, the

---

duction or the share of ‘non-contributing’ energy sources, e.g. a switch to nuclear power dominated energy mix, would not change the AHF contribution of SSP5, of course.

global energy production differs slightly between the two data sets in 2010 (P_{hum} in the World Bank data for region 'w' (world) is roughly 0.003 $\frac{W}{m^2}$ larger than in the SSP data).

- Method **'growth'**: In a second approach only the yearly growth rates of the energy production for all regions are derived from the $\widetilde{\text{SSP5}}$-baseline projection. These growth rates are then multiplied to the data from the The World Bank in 2010. This results in a smooth transition. However, one disadvantage of this method is that all the data after 2010 is neither properly attributable to IEA (2014) and The World Bank (2018) nor to the $\widetilde{\text{SSP5}}$-baseline scenario. For example, in the IEA and World Bank setup the 'Reforming States' and the EU are combined in 'Europe and Central Asia' with the same high energy production per area unit until 2010. This method, however, predicts a higher growth rate for the 'Reforming States' than for the 'EU' until 2020 and, thereby, makes the already exaggerated contribution of the 'Reforming States' to the global AHF even larger.

Both of these methods have been investigated. The code to reproduce the data sets can be found on GitHub in the file create_SSP5baseline_Phum_files.py. A comparison between the P_{hum} inputs derived from the two methods (for the year 2050) is shown in Figure 7.1 in the Appendix A.5. However, the deviations on a global-scale are so small that the differentiation between both methods does not play a further role in this analysis. The only exceptions are the jump in 2010 and consequently the slightly lower global energy production for the method 'direct'. However, this also barely influences the global mean temperature. All future results in this analysis use the 'growth' method unless otherwise stated.

4.3 Implementation

After preparing the forcing data as described in the last section, the process of the AHF forcing itself needs to be implemented in CLIMBER.

The following bits of code of the POTSDAM-2 module were added/adjusted in order to incorporate the forcing from the AHF. The method is similar to the calculation in the EBMs in Chapters 2 and 3, where the AHF is added to the net energy uptake in each cell at the surface of the atmosphere grid.

First of all, though, the AHF needs to be stored into the field 'P_hum' in each year. Here, this is implemented via two new subroutines 'read_P_hum' in 'exp.F', which is called in 'ini.F' (in the beginning of the simulation), and 'get_current_P_hum', called in 'potsdam2.F' (for each year). The code used for both subroutines can be found in the Appendix A.6.

The crucial part of the process, though, takes place in the subroutine 'SURFLX' (computation of surface fluxes) in the program 'svat.F', which is called in the subroutine 'SVAT' for all land surface types (tree, grass, dessert, glaciers). The relevant parts of the subroutine 'svat' and the subroutine 'surflx' are shown below, in order to get a feeling for the code. The changes are indicated in red. Additional comments after '#' are added to clarify the meaning:

```
SUBROUTINE SVAT
# [...]
 do  100 i=1,IT    # latitude loop
     COSZ(i)=COSZM(i,NJUL) # cos(lat) accounts for the size of the latitude band.
     do 100 n=1,NS        # longitude loop
```

```
          do 10 ntp=1,NST         # surface type loop
              if (NEXT(ntp).eq.1) then  # if there is any land fraction > 0 in the cell.
                  # [...]
                  if (ntp.gt.2) then        # i.e. if surface type is tree, grass, bare soil or glac
                      call SURFLX
                  endif
              endif
          10     continue
call AVEFLX  # averages over the surface types
# [...]

 *******************************************************************
                       subroutine SURFLX
 *******************************************************************
# [...]
      COMMON /current_P/ P_hum(1:16, 1:24) # loads the P_hum Matrix for the current year.
# [...]

c...6) Net energy flux
        QNET(i,n,ntp)=
     >    SABST(i,n,ntp)-FLWRDST(i,n,ntp)-FLWRST(i,n,ntp)-FHST(i,n,ntp)
     >    - CLE*! Modified by M Montoya (1.-FRSNW(i,n))*
     >    (EVPST(i,n,ntp)+ETRNSST(i,n,ntp)+PRCINTST(i,n,ntp))
c Modified by M Montoya      >    - FRSNW(i,n)*CLS*EVPSNST(i,n,ntp)
     >    - CLS*EVPSNST(i,n,ntp)
     >    + P_hum(n,IT+1-i)
```

The variables in the last equation represent radiative fluxes and the heat fluxes from precipitation, evaporation or snow melting. Together with the P_{hum} input this gives the net energy flux QNET in each cell for each land surface type. Similar equations are evaluated for sea ice and ocean surfaces (without the AHF, of course).

Afterwards, in the subroutine 'AVEFLX', these energy balances are weighted via the fractions of the surface type and averaged to get an update of the surface temperature in the specific cell[4].

The commands needed to make a CLIMBER run are summarised in How_to_run_and_analyse_climber. However, as the code for CLIMBER as well as the data of the spin-up runs are on the PIK-internal servers, this can only be reproduced by PIK members with an account on the computing cluster so far.

4.4 Analysis of the Model

This section presents the results of the AHF impact in the CLIMBER model focusing on the global mean temperature (Section 4.4.1), the ice-albedo feedback (Section 4.4.2) and the ocean heat uptake (Section 4.4.3). All these forcings are summarised in Section 4.4.4. Furthermore, the dependency of the

---

[4] Hence, the energy balance in a cell with a relatively large sea ice or ocean fraction is changed much less by the P_{hum}-term than in a cell in the same region with a larger land fraction, even though the P_{hum} values inserted are the same in both cells.

impact on the location of the heat emission is analysed in Section 4.4.5. Some further implications of the AHF forcing are briefly discussed, e.g. with respect to the reversibility of the impacts (Section 4.4.6), the Atlantic Overturning Circulation (Section 4.4.7) and the simultaneous increase of CO_2 and the AHF (Section 4.4.8).

4.4.1 Temperature Impact

Transient and Equilibrium Temperature Change due to the AHF. In the following, two CLIMBER simulation runs are presented: One with all forcings implemented as described above (perturbed run) and one with all forcings except for the AHF term (reference run). The global mean (transient) temperature difference due to the P_{hum} forcing is calculated and shown in Figure 4.6.

Until 2010, the temperature increase follows an exponential curve with a growth rate of 1.7% per year – consistent, but slightly smaller, than the growth of the historic P_{hum} data in these decades. After 2010, in Figure 4.6, the AHF-forcing grows with 2% per year. So does the temperature response due to the AHF. All other parameters or variables follow the trajectories described before (e.g. CO_2 stays constant after 2010, the solar constant follows the CMIP-recommended future projections) in both runs. However, the actual global mean temperatures of the reference and the perturbed run (lower graph in Figure 4.6) still grow significantly after 2010 due to long-term effects of these historic forcings.

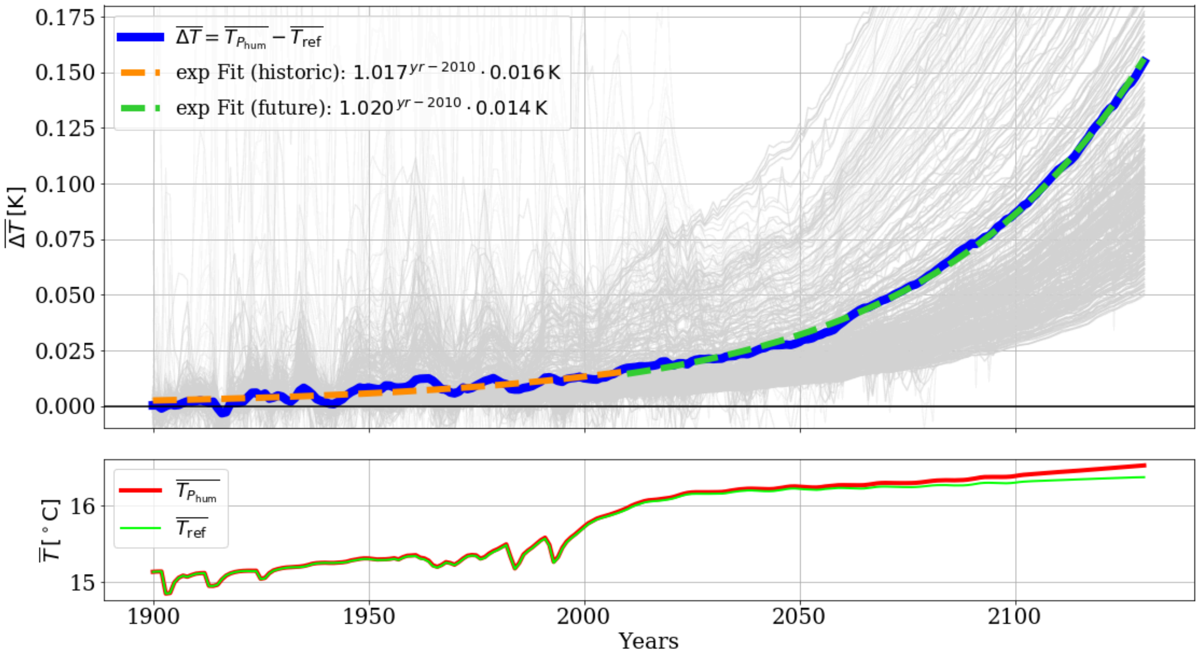

Figure 4.6: Global mean temperature (lower graph) of a perturbed run, $T_{\mathrm{P_{hum}}}$, i.e. with P_{hum} input, and a reference run without P_{hum} forcing, T_{ref}, and their difference (upper graph) over time. After 2010, the AHF forcing of the perturbed run grows with 2% per year. The grey lines show the local temperature changes in every cell. In some cells (in the area of the North Atlantic), large fluctuations occur until roughly 2025. A possible reason for this is the interplay of ocean circulations and sea ice in the North Atlantic as discussed in the text. Exponential functions can be adequately fitted to the global mean temperature change with growth rates of 1.7% and 2.0% per year for the historic data and future projections, respectively.

The equilibrium temperature response for a given P_{hum} forcing can be obtained by increasing the P_{hum} variable to the desired value and then integrating for a relatively long period of time keeping all forcings constant until a saturation is reached. In this thesis, 120 years are chosen for the integration time, although, of course, there are still small temperature changes by then in all scenarios. One example, of the equilibrium temperature response is shown in Figure 4.7, where the AHF is increased by 2% per year until 2130 and then kept constant at $P_{\text{hum}} = 0.36\,\text{W/m}^2$.

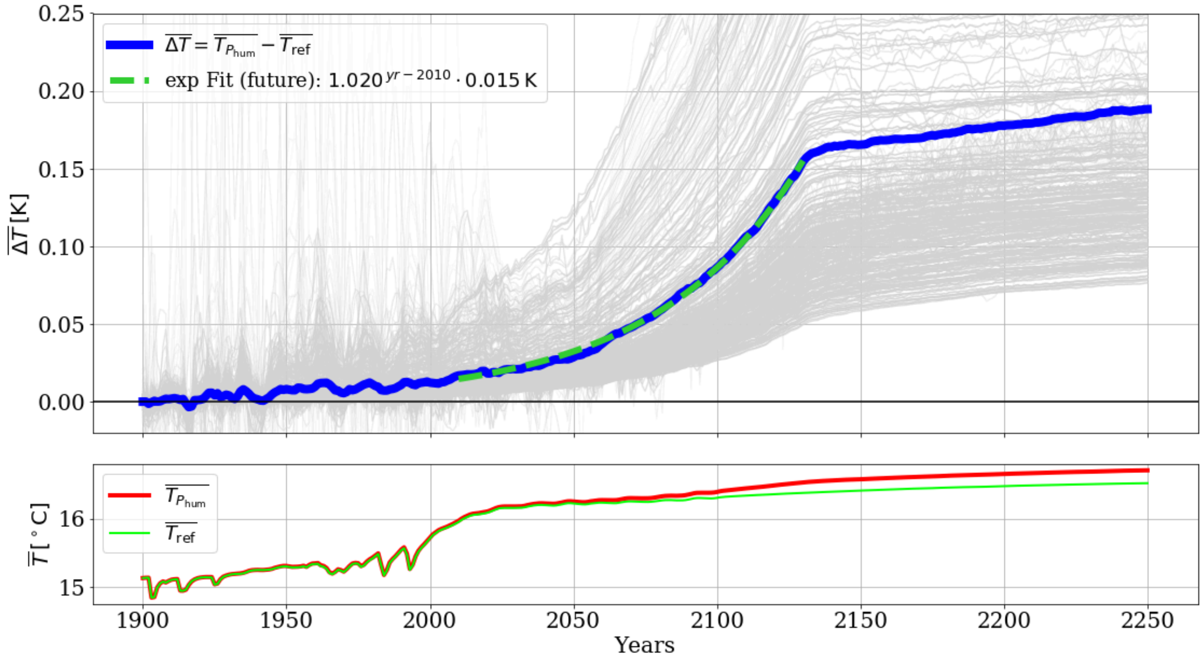

Figure 4.7: Equilibrium run for the AHF forcing in the year 2130 after a continued 2% growth per year, i.e. $P_{\text{hum}} = 0.36\,\text{W/m}^2$. The left part of the plot is equivalent to Figure 4.6. While the temperature change has not completely saturated in 2250, the obtained result approximates the equilibrium temperature response due to the forcing in 2130 reasonably well. Here, the equilibrium response to the AHF forcing ($\sim 0.188\,\text{K}$) is 21% larger than the transient temperature response in 2130 ($\sim 0.155\,\text{K}$).

Fluctuations in the North Atlantic. The grey lines in Figure 4.6 and 4.7 show the temperature changes of every single cell over the years compared to the reference run (the transparency accounts for the different area sizes of the cells). Especially until 2025, strong fluctuations in the local temperature changes occur in some cells. The corresponding cells are mainly located in the North Atlantic between Greenland and Spitzbergen. Figures 4.8 to 4.11 show the temperature change due to the AHF and the corresponding change in sea ice fraction (which will be described in detail later) in the relevant area.

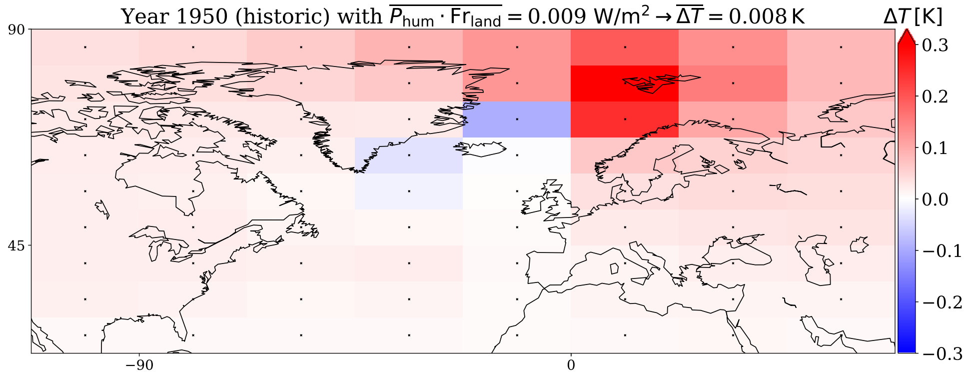

Figure 4.8: Surface Temperature change in 1950.

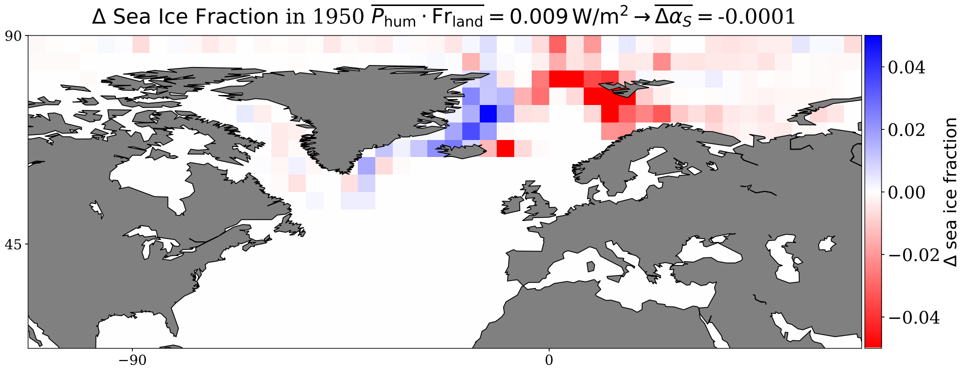

Figure 4.9: Change in sea ice fraction in 1950.

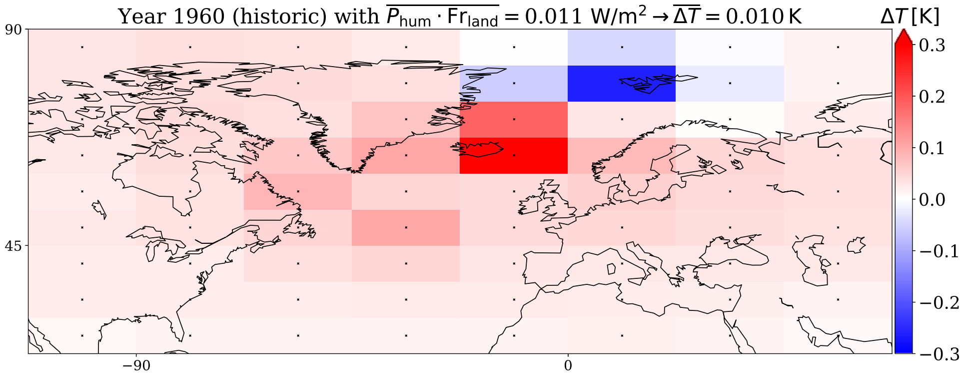

Figure 4.10: Surface Temperature change in 1960.

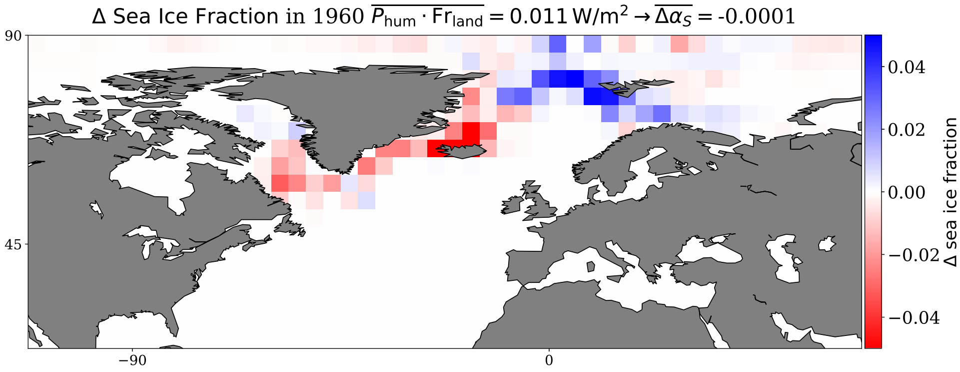

Figure 4.11: Change in sea ice fraction in 1960.

E.g. the temperature change of roughly 0.3 K in 1950 in Spitzbergen w.r.t. the reference run (Figure 4.8) changes into the opposite within only one decade – a -0.3 K lower temperature in 1960 (Figure 4.10). Apparently, these fluctuations (in Figures 4.6, 4.8 and 4.10) correlate with strong changes in the sea ice fraction along the east coast of Greenland and Spitzbergen (Figures 4.9 and 4.11). This behaviour shows similar features as the strong variability in the subpolar gyre found in Mengel et al. (2012). According to the authors, the self-enhancing loop of increased salt transport in the subpolar gyre and stronger deep convection influences the climate of the North Atlantic. However, they assume that this might be especially pronounced in models with a low spatial resolution like CLIMBER. The small AHF forcing inserted into CLIMBER in the years before 2025 already seems to have a large impact on the evolution of the subpolar gyre. The changes in the subpolar gyre also affect the strength of the Atlantic Meridional

Overturning Circulation (AMOC) (Caesar et al., 2018), which is described later in Section 4.4.7 in detail. Figure 4.12 shows that the AMOC strength of the perturbed run clearly deviates from the reference run in 1960 due to the P_{hum} insertion, whereas in 1950 it is roughly equivalent to the reference AMOC strength. A stronger AMOC leads to more heat transport from the equator to the subpolar regions and, hence, to less sea ice near Greenland and Iceland (see Figure 4.11). This correlates with a net global mean temperature increase in the years after 1960 (see Figure 4.12). On the other hand, apparently, the subpolar gyre, which is not investigated in more detail, leads to an increase in sea ice around Spitzbergen in 1960 w.r.t. the reference run.

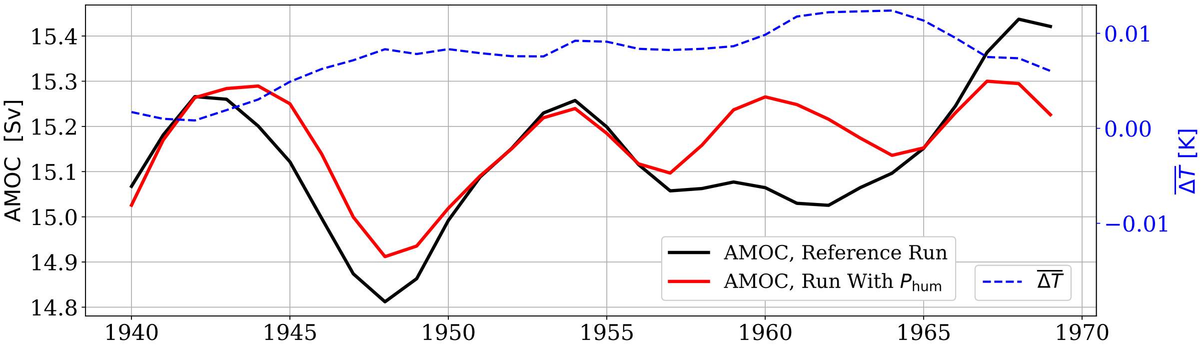

Figure 4.12: The AMOC strength from 1940 to 1970 in a reference run (black) and a run perturbed with the AHF (red). In 1960 the P_{hum} input leads to a strong deviation from the normal decadal cycle of the AMOC strength in CLIMBER, accompanied by changes in the sea ice and local temperature fluctuations. The AMOC strength is discussed in detail in Section 4.4.7.

Anyway, globally averaged the temperature change generally follows the exponential curve dictated by the growth of the AHF despite these fluctuations. After roughly 2025, the fluctuations disappear, since the AHF causes the AMOC strength to decrease so much (shown in Section 4.4.7) that the deviation is larger than the fluctuations and the AMOC in the perturbed run is always weaker than the reference circulation.

Future Projections in Comparison. Figure 4.13a and 4.13b compares both future scenarios investigated in this thesis: The constant-growth scenario (with a growth rate of 2% per year, as seen before in Figure 4.6) and the $\widetilde{\text{SSP5}}$-baseline scenario.

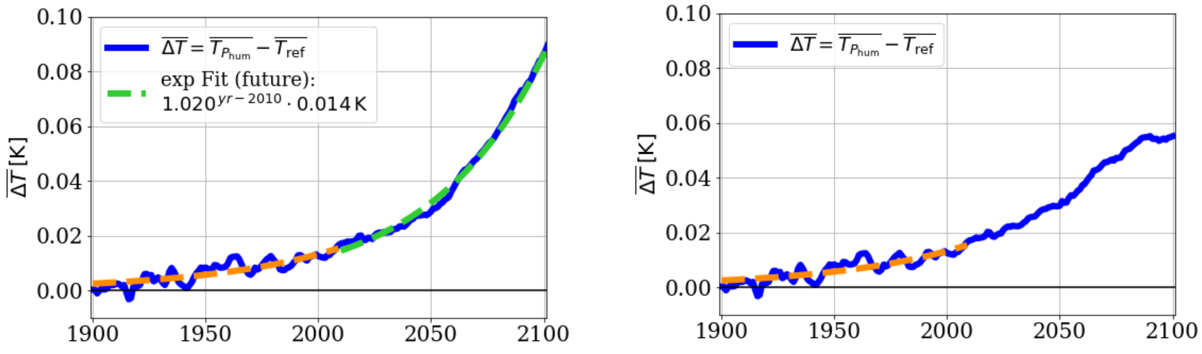

(a) 2%-growth after 2010.

(b) $\widetilde{\text{SSP5}}$-baseline growth scenario.

Figure 4.13: Future scenarios for P_{hum} and their global mean temperature response. The left plot is equivalent to Figure 4.6 and shown just for comparison purposes.

The temperature change due to the AHF in the latter scenario increases in a similar way as in the simple growth case until roughly 2075. However, due to the flattening of the energy production curve after 2075 (Figure 4.5), the magnitude of the global temperature response in 2100 is reduced: $\overline{\Delta T}\,(2100) = 0.55\,\mathrm{K}$ in comparison with $\overline{\Delta T}\,(2100) = 0.86\,\mathrm{K}$.

Map of the Temperature Change. A map of the temperature increase due to P_{hum} in 2100 after a 2% growth is shown in Figure 4.14 (i.e. a snapshot from Figure 4.13a at the year 2100).

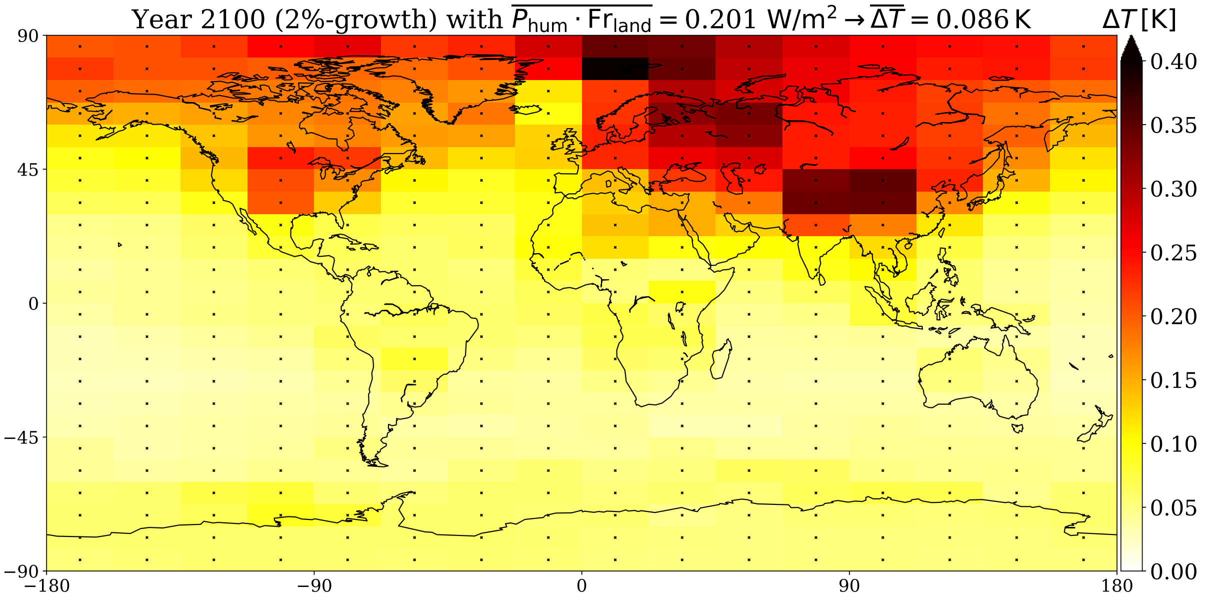

Figure 4.14: **2%-growth:** Temperature increase due to the 2%-growth of the heterogeneous P_{hum} input in 2100 with the same distribution as in 2010.

In general, the same pattern as indicated by the heterogeneous P_{hum} input at that time is obtained (compare with the $P_{\mathrm{hum}} \cdot \mathrm{Fr}_{\,\mathrm{land}}$ map in Figure 4.4). However, the temperature increase is spread out due to fluxes across the cells. Furthermore, the Arctic region as well as East Russia or North Canada show an extensive temperature increase even though there is no direct forcing applied. The strong Arctic warming shown here is of course correlated with the ice-albedo feedback (described in more detail later) and changes in the subpolar gyre as described before.

Figure 4.15 shows the equivalent map for the $\widetilde{\text{SSP5}}$-baseline scenario in Figure 4.13b. Note again, except for the energy production, all forcings, e.g. the $\mathrm{CO_2}$ concentration, remain constant at the 2010 values. Both the local and global magnitude of the temperature response is significantly lower than in the simple continued growth case. Some specific features of this $\widetilde{\text{SSP5}}$-baseline scenario include e.g. the pronounced local temperature increases around Asia.

Sanity Checks and Comparison with EBMs. The above results for the temperature impact require some ‘sanity checks’ and a comparison to the previous EBMs in order to evaluate whether the conceptual thoughts from Chapters 2 and 3 are consistent with the results from the CLIMBER simulation.

- In Section 2, the EBM-0D was introduced in equation (2.9) (with the Boltzmann parametrisation from equation (2.5)). This model yields a temperature change of roughly $0.010\,\mathrm{K}$ for the current $\overline{P_{\mathrm{hum}}} = 0.034\,\mathrm{W/m^2}$. In the simulation in Figure 4.6, the result is nearly twice as large: $\overline{\Delta T}\,(2010) = 0.016\,\mathrm{K}$. One reason for this discrepancy is of course the missing ice-albedo feedback in the EBM-0D.

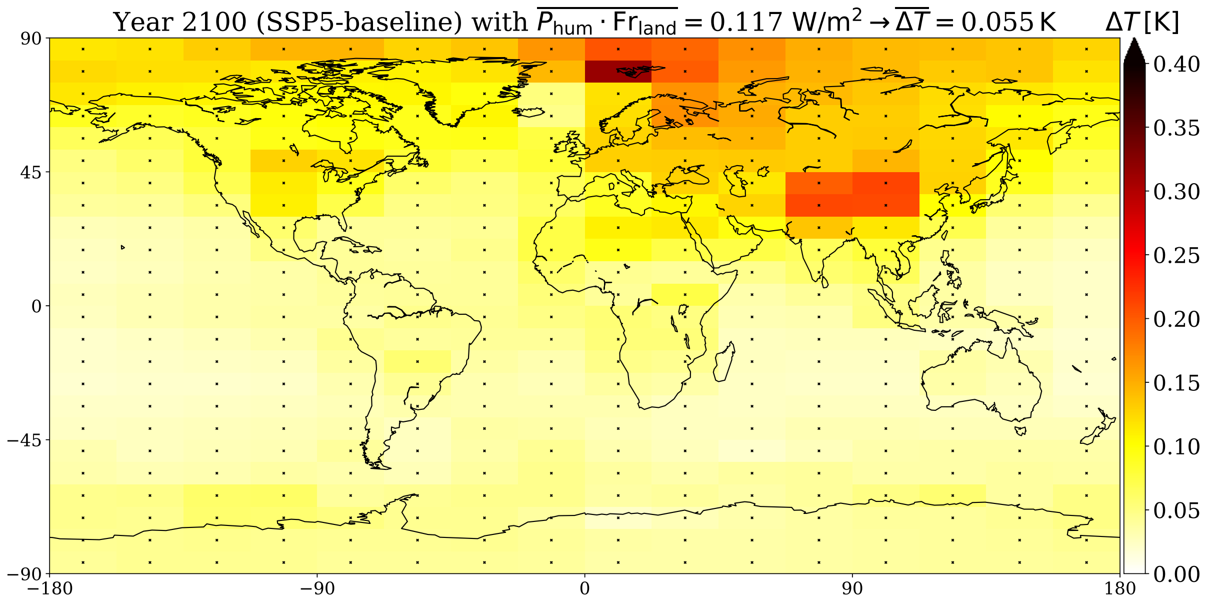

Figure 4.15: **$\widetilde{\textbf{SSP5}}$-baseline:** Temperature increase in 2100 due to the heterogeneous $\boldsymbol{P_{\mathrm{hum}}}$-input following the $\widetilde{\textbf{SSP5}}$-baseline scenario. The future scenario is patched to the historic data via the method 'growth', i.e. only the growth rates of the primary energy (or $\boldsymbol{P_{\mathrm{hum}}}$) for each region are retrieved from the $\widetilde{\textbf{SSP5}}$-baseline scenario. The global mean temperature impact is **0.55 K**, slightly more than half of the increase under a continued **2%** growth.

- Secondly, the impact of a tenfold increase of P_{hum} in the CLIMBER model is investigated. This is compared to the previous results from the EBM-1D in Section 3.3.2.

  A tenfold increase is roughly equivalent to a continued 2%-growth for 116 years. Therefore, the result from Figure 4.6 in the year 2126 can be used to simulate a tenfold increase in the CLIMBER run. The transient temperature change due to the AHF in CLIMBER in 2126 is 0.127 K larger than in 2010. From Figure 4.7, the equilibrium instead of the transient temperature response from the AHF forcing can be inferred. For the forcing in 2130, the equilibrium temperature response is $\overline{\Delta T_{\mathrm{equ}}}(P_{\mathrm{hum}}\,(2130) = 0.36\,\mathrm{W/m^2}) = 0.171\,\mathrm{K} + \overline{\Delta T\,(2010)}$. Due to the different P_{hum} values in 2126 (factor 9.9 $\sim$ tenfold) and 2130 (factor 10.7, i.e. $\overline{P_{\mathrm{hum}}}(2130) = 0.36\,\mathrm{W/m^2}$), this is of course slightly higher than the desired equilibrium temperature response of a tenfold increase. Scaling appropriately yields:

$$\overline{\Delta T_{\mathrm{equ}}}(P_{\mathrm{hum}} = 10\cdot P_{\mathrm{hum}}(2010)) = 0.171\,\mathrm{K}\ \cdot 1.02^{116}/1.02^{120} = 0.157\,\mathrm{K}\ . \tag{4.3}$$

  For the EBM-1D the most plausible models are the configurations with the Boltzmann parametrisation and a freezing temperature of $T_f = -10°C$ and both the 'small' and 'normal' meridional transport constant, i.e. (BsD$_{\text{-}10}$) and (BD$_{\text{-}10}$) (as well as BsD$_{\text{-}2}$), as discussed in Section 3.3.2. The global mean temperature increase from the (Gaussian) AHF forcing in these models is 0.096 K, with no shift of the iceline, and 0.22 K, with a shift of the iceline of two degrees in the North Hemisphere, respectively[5]. All other configurations of the EBM-1D result in a much higher temperature increase due to sometimes substantial changes in the ice fraction and, hence, the albedo.

---

[5] With a spatial resolution of $\Delta\theta = 1°$. Taking a higher resolution leads to slightly different, more distinguished results. In particular, the northern iceline in (BsD$_{\text{-}10}$) shifts by $0.5°$ instead of $0°$ and the temperature change increases to 0.14 K for a spatial resolution of $\Delta\theta = 0.5°$, as discussed in Section 3.3.2

In summary, the temperature impacts for a tenfold increase of the AHF for the climate model CLIMBER (transient and equilibrium run) are somewhere in between the ($\mathrm{BsD}_{\text{-}10}$) and the ($\mathrm{BD}_{\text{-}10}$) EBM-1D configuration's temperature increases (for a resolution of $\Delta\theta = 1°$), indicating that the shift of the iceline in ($\mathrm{BD}_{\text{-}10}$) is still exaggerated, however, at the same time emphasising the importance of the ice-albedo feedback:

$$\overline{\Delta T}\,^{\Delta\text{iceline}=0°}_{\text{BsD}_{-10}} < \overline{\Delta T}_{\text{CLIMBER trans.}} < \overline{\Delta T}_{\text{CLIMBER equil.}} < \\ < \overline{\Delta T}\,^{\Delta\text{iceline}_{\text{NH}}=2°}_{\text{BD}_{-10}} \left(< \overline{\Delta T}\,^{\Delta\text{iceline}_{\text{NH}}=2°}_{\text{BsD}_{-2}} \right) . \tag{4.4}$$

In fact, the result from the shortly mentioned high resolution model ($\mathrm{BsD}_{\text{-}10}$) with $\Delta\theta = 0.5°$, 0.14 K, is very close to the temperature increase from the CLIMBER model.

- In Figure 4.13a, the temperature change grows with 2.0% per year in alignment with the prescribed 2% increase of the P_{hum} in each year after 2010[6]. Furthermore, these exponential fits in Figures 4.13a and 4.6 also exhibit an important number for estimations, which might be useful to keep in mind: The pre-factors of the exponential function are 0.014 to 0.016 K, caused by the (mean) AHF forcing of 0.034 $\mathrm{W/m^2}$ in 2010. Expressed alternatively, each $\mathrm{W/m^2}$ results in a 0.41 to 0.47 K transient global mean temperature rise. According to the IPCC (2013) the transient climate response (to a steady increase of CO_2) is roughly $0.48 \pm 0.19\,\frac{\mathrm{K}}{\mathrm{W/m^2}}$[7], which is in good agreement with the results from CLIMBER.

Local Temperature Change Over AHF Forcing. Another approach to frame the simulation results, which also helps to check the trustability of the model, is to investigate each cell of the simulation individually by plotting all $\Delta T\,(lat, lon)$ over the associated $(P_{\text{hum}} \cdot \mathrm{Fr}_{\text{land}})\,(lat, lon)$, which is shown in Figure 4.16:

The correlation between local temperature change, ΔT_{cell}, and local $P_{\text{hum}} \cdot \mathrm{Fr}_{\text{land}}$ forcing input is plotted on the right. All cells with $P_{\text{hum}} = 0$ (e.g. ocean cells), which are the vast majority, are excluded from this plot but the temperature change in those cells is shown in the histogram on the left. Another histogram of the temperature changes in *all* cells is plotted in the middle. Most cells have a temperature change close to or just below the average temperature change (see also the grey lines in Figure 4.6), i.e. the temperature anomalies arising from the P_{hum} forcing in confined regions are spread out to neighbouring and remote cells. Naturally, the temperature changes in cells with a local input of $P_{\text{hum}} \cdot \mathrm{Fr}_{\text{land}} \neq 0$ deviate more from the average (right plot). As previously derived in the EBM-0D (with Boltzmann parametrisation), the global mean temperature change can be estimated by equation (2.10):

$$\overline{\Delta T_S} = \left(T_S^4 + \frac{\overline{P_{\text{hum}} \cdot \mathrm{Fr}_{\text{land}}}}{\tau\sigma} \right)^{\frac{1}{4}} - \overline{T_S} \, . \tag{4.5}$$

Assuming that this equation holds for any cell (lat, lon) of the climber grid (i.e. no meridional heat transport, no feedbacks, etc.)[8], then the temperature in each cell should change accordingly to this law.

---

[6] The growth rate is declining with the length of the simulation or the number of years comprised in the exponential fit to the data. This is expected since this is a transient instead of an equilibrium run. Therefore, a higher absolute P_{hum} change (e.g. a 2% increase later in the simulation) leads to a higher rate of absolute temperature change. However, this is delayed through the heat storing processes e.g. in the ocean. Anyway, the growth rate of the temperature increase in Figure 4.13a is reasonably close to 2% per year for all sensible fits to the simulated data.

[7] Derived by dividing the transient climate response by the effective radiative forcing for CO_2 doubling. Errors are calculated via the standard variance formula.

[8] This assumption implies that the map of the temperature change perfectly resembles the map of the $P_{\text{hum}} \cdot \mathrm{Fr}_{\text{land}}$-input.

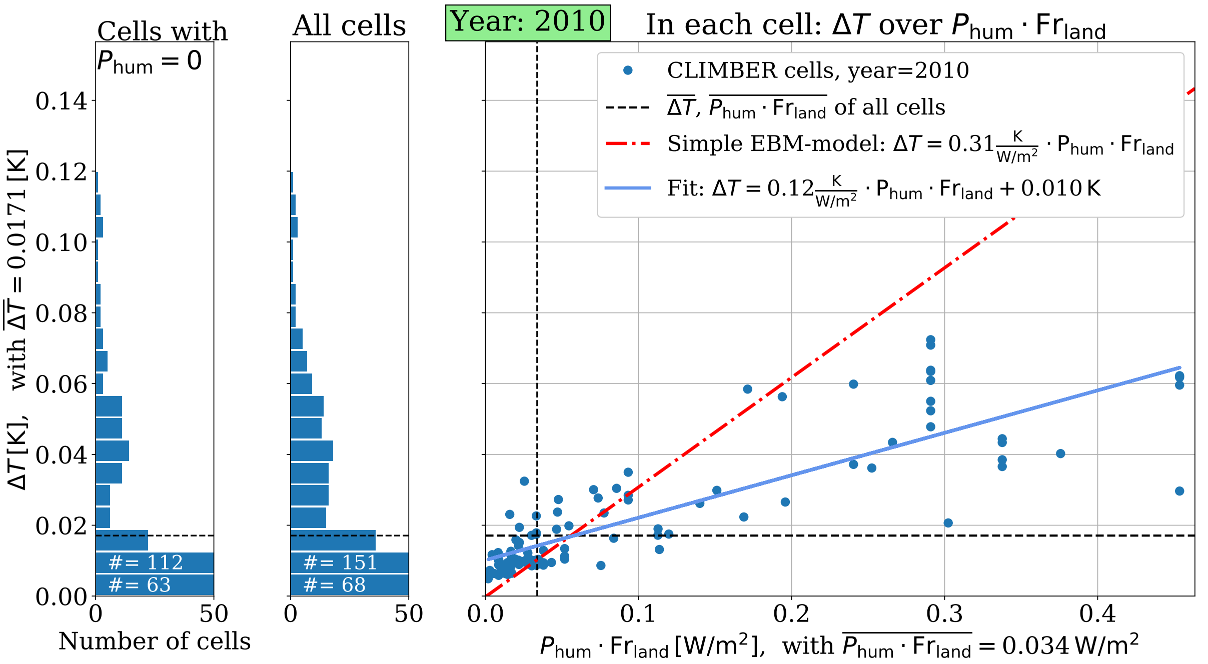

Figure 4.16: Right plot: Plot of the correlation between the simulated data for the transient ΔT and $P_{\mathrm{hum}} \cdot \mathrm{Fr}_{\mathrm{land}}$ for each cell with a non-zero AHF input in the CLIMBER grid for a run in 2010. The histogram in the left plot contains all cells with $P_{\mathrm{hum}} = 0$, which are removed in the right plot. The histogram in the middle shows the distribution of temperature changes for *all* cells. For comparison, some theoretical model data from equation (4.6) is shown in the correlation plot, which is derived in the main text. The dashed lines in the right show the average temperature increase in 2010 (0.016 K) and the mean $\overline{P_{\mathrm{hum}} \cdot \mathrm{Fr}_{\mathrm{land}}}$ (0.034 W/m^2).

For small P_{hum} this simplifies to a linear curve (red dashed line):

$$\Delta T\,(lat,\,lon) = 0.25 \cdot \frac{1}{\sigma \tau T^3} \cdot (P_{\mathrm{hum}} \cdot \mathrm{Fr}_{\mathrm{land}})\,(lat,\,lon) + \mathcal{O}(P_{\mathrm{hum}}^2)\,. \tag{4.6}$$

For this simple model the slope of the curve is roughly $0.31 \frac{K}{W/m^2}$ (red line in Figure 4.16). However, the simulated temperature change in cells with a P_{hum}-input is mostly much lower ($0.12 \frac{K}{W/m^2}$), since the temperature anomalies spread out to neighbouring cells.

Summary. In general, as expected, the global mean temperature change in CLIMBER follows the pattern and evolution of the P_{hum} forcing. However, the temperature response is spread out to neighbouring cells such that the temperature increase close to the global mean is observed nearly all around the planet. Temperatures in the Arctic region are especially affected (‘Arctic amplification’). Some interesting observations include the fluctuations of the temperature and sea ice in the North Atlantic in this model (correlated to changes in the subpolar gyre and the Atlantic Meridional Overturning Circulation) and the similarity to the results from the one-dimensional Energy Balance Model presented in Section 3.3.2 and values from the literature. Today the AHF is responsible for roughly 0.016 K (transient) global warming, which would be slightly larger in equilibrium. Every W/m^2 of AHF forcing leads to an additional transient global mean temperature change of 0.41 to 0.47 K. The CLIMBER model lies in between the EBM-1D configurations (BsD$_{\text{-}10}$) and (BD$_{\text{-}10}$) (for $\Delta\theta = 1°$ spatial resolution).

4.4.2 Albedo Analysis

Similar to the EBM-1D in Chapter 3, the ice-albedo feedback is a major feedback that enhances the temperature response in CLIMBER.

CLIMBER's POTSDAM-2 module calculates the radiative fluxes in the atmosphere. For this, the surface albedo in each surface cell is calculated from each fraction of the surface types. This section analyses the decline of the surface albedo with increasing AHF due to the sea ice retreat and changes in the snow fraction. Furthermore, the consequent global radiative forcing contribution resulting from the associated decrease of the planetary albedo is estimated.

Impact of the AHF on the Modelled Surface Albedo. Figure 4.17 shows a map of the (transient) changes in surface albedo α_S in the year 2100 due to the continued 2%-growth scenario for P_{hum}. Especially in the Arctic region the surface albedo decreases significantly in some cells, mostly in the region of the North Atlantic. E.g. in the cell covering Spitzbergen ($\alpha_{\text{S,ref}} \approx 0.2$) the albedo changes by more than 10% in 2100 due to the increase of P_{hum} (even though $P_{\text{hum}} = 0$ in this cell).

The major factor of the global surface albedo decrease is the melting of sea ice in the Arctic region (north of 67.5°, and additionally at the East Coasts of Greenland and Russia). Even though the impact of the AHF forcing (and the forcing itself) is mainly concentrated in the Northern Hemisphere, a decreasing trend of α_S can also be observed in the Antarctica in the latitude band from $-52.5°$ and $-75°$, i.e. in cells with a significant sea ice fraction. Furthermore, the relatively small changes of the surface albedo around 45° to 60° in the Northern Hemisphere are related to a decrease in the snow fraction.

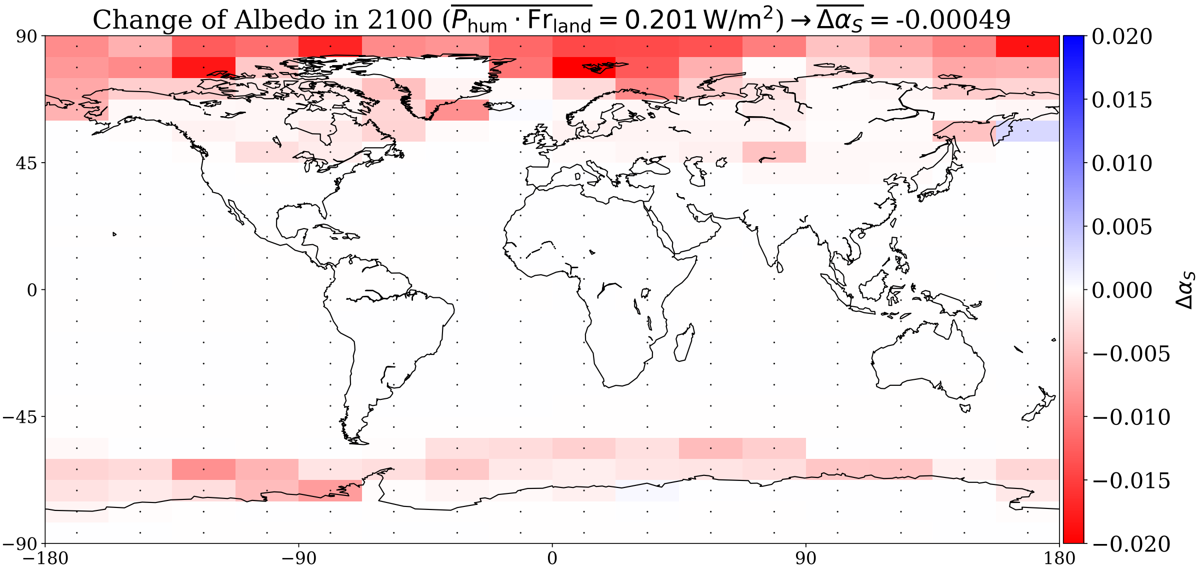

Figure 4.17: A map of the changes in surface albedo due to P_{hum} in the year 2100 (given continued 2%-growth after 2010). Especially in the region around the iceline of the North Pole the surface albedo decreases by up to 0.02 or 2%. Smaller albedo is associated with less reflection of solar radiation and, hence, higher temperatures.

In the following paragraphs these two main contributions to the reduction of the global surface albedo and, hence, to the amplified warming through the ice-albedo feedback, are investigated in more detail.

Sea Ice. The decrease in surface albedo is above all attributable to changes in the sea ice. CLIMBER's module, 'ISIS', gives the sea ice fraction in each surface cell of the ocean grid. Figure 4.18 and 4.19 show maps of the current sea ice and its decrease (in units fraction of a cell) due to the increase of P_{hum}.

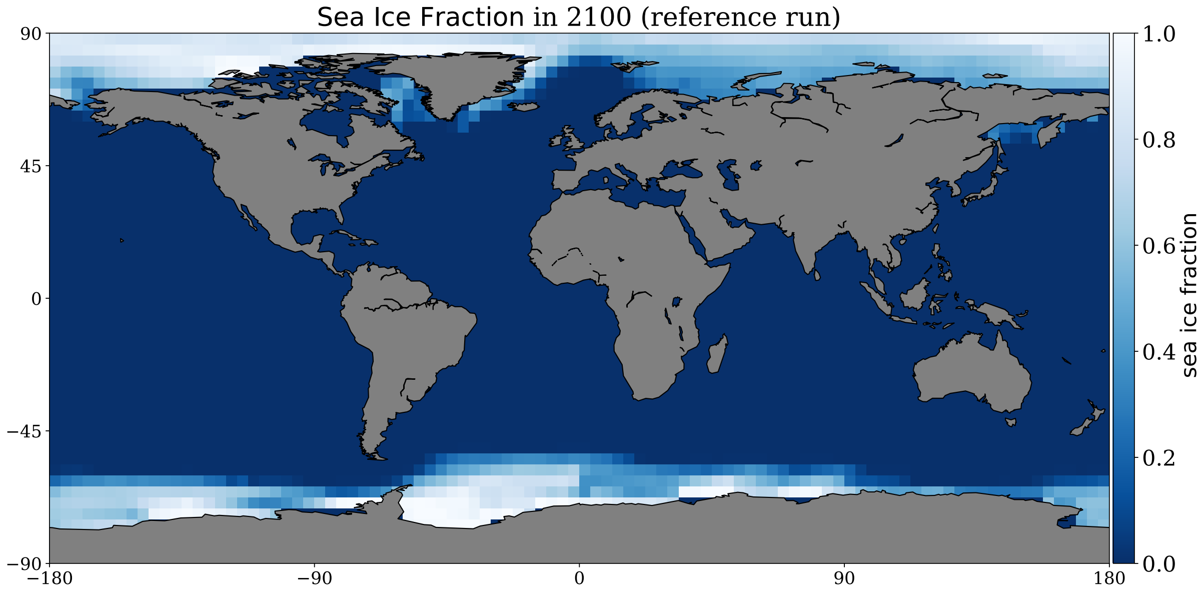

Figure 4.18: Sea ice fraction in 2100 for the reference run ($P_{\text{hum}} = 0$).

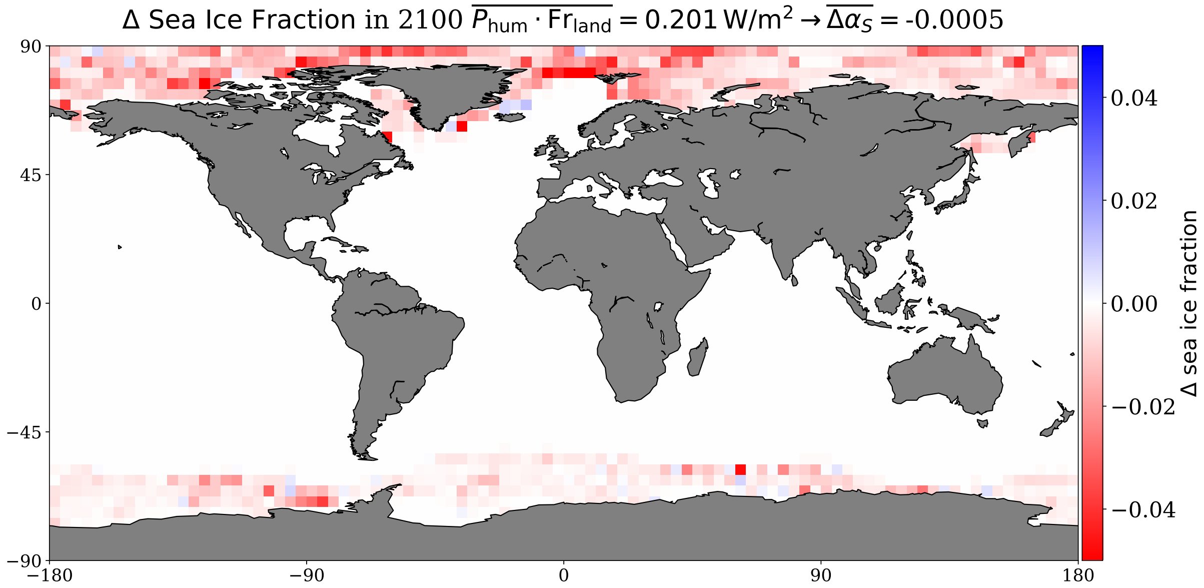

Figure 4.19: Changes of the sea ice fraction due to P_{hum} in the year 2100 (given a 2%-increase per year).

The total loss in sea ice extent can then be calculated via:

$$\Delta\ \text{Sea Ice Extent} = \sum_{\text{lat, lon}} \cos(lat) \cdot \delta lat \cdot \delta lon \cdot r^2_{\text{earth}}\ [\text{m}^2] \cdot \text{sea\_ice\_fraction}\,(lat, lon) \qquad (4.7)$$

In total, continuing a 2%-growth of P_{hum} up to 2100 leads to an additional transient sea ice loss of $2.6 \cdot 10^5\,\text{km}^2$ in CLIMBER, as shown in Figure 4.20. The vast majority of this in the Northern Hemisphere. For the $\widetilde{\text{SSP}}$5-baseline scenario, a total of $1.6\,\text{km}^2$ of sea ice is lost due to the AHF increase in 2100.

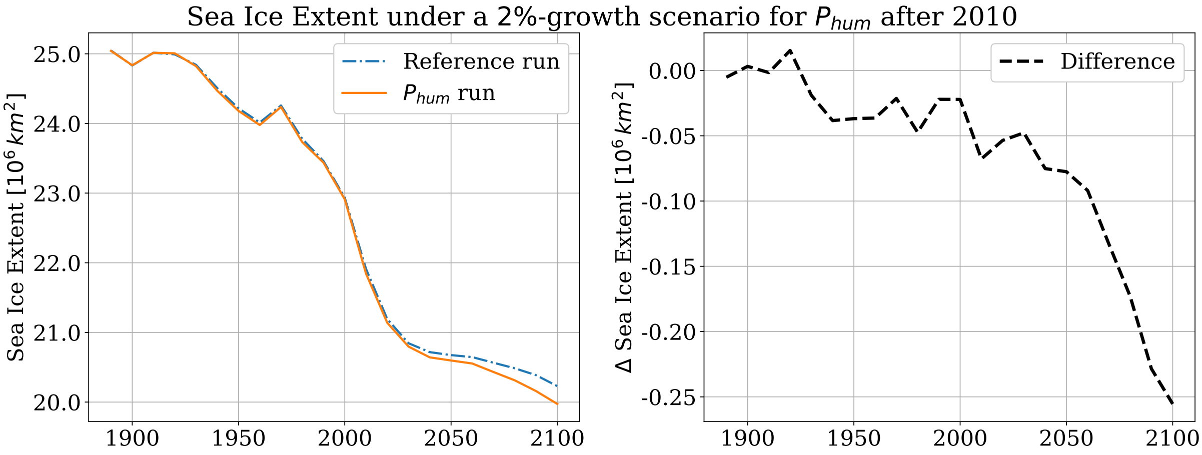

Figure 4.20: Total sea ice extent in m^2 and transient sea ice loss due to increasing P_{hum} with a 2%-growth rate. The strong decrease of sea ice in both the reference and the perturbed runs even after 2010 is due to the long-term temperature increase from the growing greenhouse gas emissions in the years before 2010 and the inertia of the ice. In 2100, a total of $2.6 \cdot 10^5\,\mathrm{km}^2$ of sea ice is additionally lost in CLIMBER due to the P_{hum} increase in this scenario. This is further enhanced if the equilibrium impacts are considered.

It should be noted that the sea ice, in general, decreases much stronger due to the long-term effects of the increasing greenhouse effect in the years before 2010. Anyway, this additional decrease from the AHF is of course strongly linked to the changes in surface albedo shown in the previous paragraph. From Figure 4.22b, an albedo change of roughly $\Delta\alpha_{\mathrm{melting}} = 0.6$ (from 0.7 to 0.1) is estimated, if ice disappears and is replaced by e.g. open water. Hence, with a simple back-of-the-envelope calculation, the total decrease of sea ice extent caused by the AHF leads to a global albedo decrease of

$$\overline{\Delta\alpha_{\text{from sea ice}}} = \Delta\alpha_{\text{melting}} \cdot \frac{A_{\text{sea ice}}}{4\pi \cdot r_{\text{earth}}^2} \approx 0.6 \cdot \frac{-2.6 \cdot 10^5\,\mathrm{km}^2}{4\pi \cdot (6371\,\mathrm{km})^2} = -3 \cdot 10^{-4} \tag{4.8}$$

This is in good agreement with the $\Delta\alpha_S = -4.9 \cdot 10^{-4}$ from the analysis of the atmosphere module in Figure 4.17. The equilibrium sea ice impact is accordingly larger than this result due to the long-term response of ice. The equilibrium run with 120 years of constant forcings (c.f. Figure 4.7) yields a larger sea ice loss compared to the transient impact in the order of 30% (not shown).

Snow. Additional to the sea ice, CLIMBER also computes the snow covered land fraction in the atmosphere module POTSDAM-2, which generally adjusts quickly to new climate conditions. This further influences the surface albedo. Assuming the continued 2%-growth of P_{hum} until 2100, some small changes in the global snow patterns can be observed. E.g. in the Northern Hemisphere winter months (December, January, February: DJF) the global snow fraction shows a decreasing effect over the timescale of a century (not shown here).

Anyway, the decrease in snow fraction due to the AHF and the consequent temperature increase is more locally confined. For example, Figure 4.21 shows the absolute change in snow fraction for the Northern Hemisphere winter months DJF in 2100 under a continued 2% growth. Similar to the iceline in Section 3.3.2, a ‘snowline’ can be defined at those latitudes, at which the snow fraction changes from 0 to a significantly larger value. These cells are particularly prone to a decrease in their absolute snow fraction. This appears to be especially distinct for two cells: the East Coast of Russia and East Kazakhstan. In the latter, the winter snow fraction in 2100 is 81% in the reference run but only 67% in the perturbed run

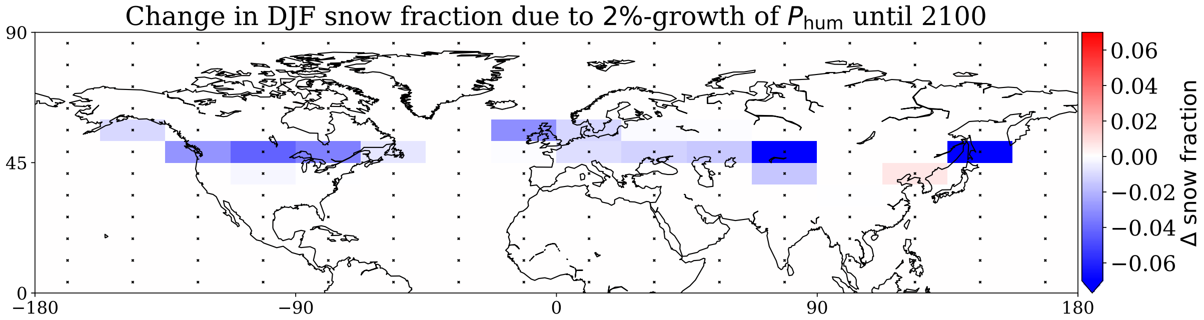

Figure 4.21: Changes in the snow fractions of the Northern Hemisphere winter months DJF in 2100 due to the 2%-growth scenario of P_{hum}. The largest absolute changes appear in Kazakhstan and East Russia. However, large relative changes, e.g. 30% less ice in North America's mainland and 8% in Germany appear all along the 'snowline'.

(even though $P_{\mathrm{hum}} = 0$ in this cell). However, large *relative* changes with respect to the snow fraction of the reference run, e.g. 30% less snow in North America's mainland and 8% in Germany appear all along the 'snowline'[9].

Surface vs. Planetary Albedo. The decrease of the globally averaged surface albedo due to P_{hum} resulting from changes in the snow and sea ice fraction, consequently, also decreases the planetary albedo, as shown in Figure 4.22a. However, a large part of the planetary albedo is influenced through the cloud cover and the reflection of the shortwave radiation in the atmosphere.

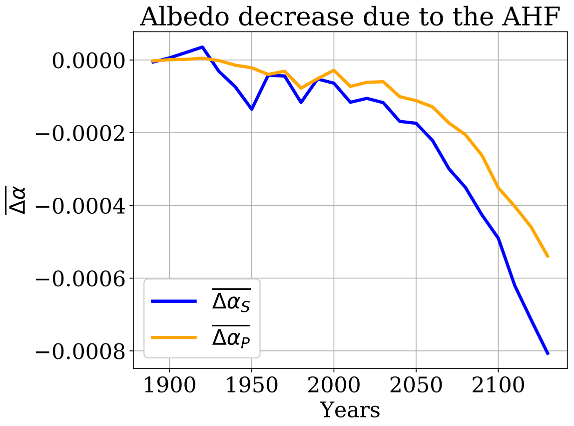

(4.22a) Global mean (surface and planetary) albedo change (given a 2%-growth of P_{hum}). The decrease of the global mean surface albedo, which amounts to $4.9{\cdot}10^{-4}$ in 2100, also leads to a decrease in global mean planetary albedo in the same order of magnitude but slightly smaller.

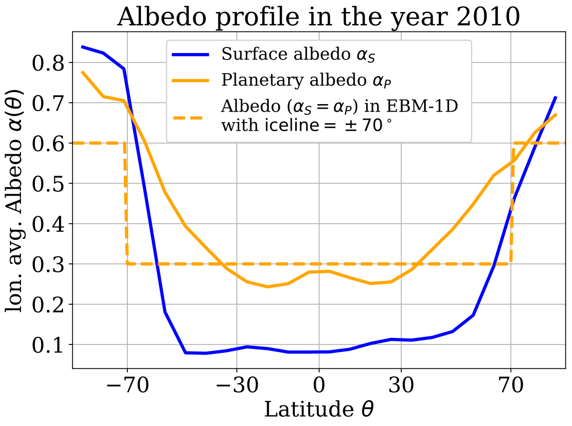

(4.22b) Longitudinally averaged surface α_S and planetary albedo α_P in the reference run in 2010. For comparison the 'surface' albedo of the one-dimensional EBM from before is also shown, in which the temperature falls below the freezing threshold for latitudes beyond ±70°.

The total decrease of the albedo until 2100, $\Delta\alpha_P = -0.00035$ (or $\Delta\alpha_S = -0.00049$) from Figure 4.22a, is equivalent to a shift of the iceline of pretty close to 0.5° in the Northern Hemisphere in the one-dimensional EBM-1D parametrisation[10]. Note that according to Montoya et al. (2005), CLIMBER tends to overestimates the planetary albedo in high latitudes.

---

[9] Comparing the relative changes in snow fraction is of course only meaningful if the fraction of land in that cell is large enough and the total base snow fraction is not too small. E.g. large relative changes of more than 90% appear e.g. in Vancouver or North East China, but the land fraction and, hence, the basis snow fraction of these cells is very small.

[10] The shift of the iceline at $\theta = 65°$ in the EBM-1D by one grid point of length $\Delta\theta$ yields an albedo change of $\Delta\alpha = \alpha_{\mathrm{new}} - \alpha_{\mathrm{old}} = (0.3 - 0.6) \cdot \cos(\theta) / \sum_\theta \cos(\theta)$. For $\Delta\theta = 0.5°$, this gives the same result.

For the purpose of comparing this section's results with the previous EBM analysis and to get a feeling for the different types of albedo, the latitude dependent albedo profile (i.e. longitudinally averaged albedo) is plotted in Figure 4.22b for the year 2010.

This analysis emphasises again the importance of the ice-albedo feedback if the AHF grows further in the future (2.6 km^2 by 2100 given the 2%-growth scenario). This process of the climate system is part of the so-called 'polar amplification' (e.g. Serreze et al. 2009). In general, most GCMs underestimate this polar amplification (Stroeve et al., 2012).Of course, this applies to all radiative forcings, not just the AHF. However, the heterogeneous pattern of the AHF forcing and its special high density in the high latitudes in the Northern Hemisphere are rather untypical features compared to traditional radiative forcing from greenhouse gases for example.

Therefore, the change in sea ice and snow patterns (and the corresponding forcing feedback) are a major factor in the calculation of the temperature response in CLIMBER due to the AHF.

4.4.3 Ocean Heat Uptake (OHU)

Next to the direct AHF forcing and the the forcing from the ice-albedo feedback a third important contribution to the global energy budget is considered in this model: The change in **h**eat **u**ptake by the **o**cean ($\overline{\Delta \text{OHU}}$). Some of the AHF emitted is captured by the oceans, which weakens the effect of the AHF on the transient surface temperature. This slowly heats up the oceans, which in turn leads to a warmer equilibrium surface air temperature at later times causing a significant delay of the global warming.

Given the 2%-growth scenario until 2100 ($\overline{P_\text{hum} \cdot \text{Fr}_\text{land}} = 0.201\,\text{W/m}^2$), the heat uptake is roughly $0.076\,\text{W/m}^2$ larger than in the reference run. I.e., the (transient) forcing from the AHF is reduced by roughly one third, assuming the heat uptake adjusts immediately to the AHF forcing. The temporal evolution of the ocean heat uptake in CLIMBER is shown later (together with some different P_hum-distributions) in Figure 4.27.

In general, an increased ocean heat uptake is a negative (transient) feedback, as the oceans absorb more radiative forcing and less heat is available to warm the surface air. However, in Section 4.4.5 a secondary process is discussed, which acts as a positive feedback: If the oceans absorb more heat, the warmer water melts more sea ice, which leads to an increased ice-albedo feedback and, hence, warms the atmosphere.

4.4.4 Total Forcing and Aggregated Forcings

In this analysis, three major contributions to the overall forcing were presented: the direct AHF forcing ($\overline{P_\text{hum}}$), the forcing from the decreased surface albedo (Section 4.4.2), which is driven by the sea ice retreat as well as, partially, a smaller snow fraction, and, finally, the change in the ocean heat uptake (Section 4.4.3), which leads to a transient negative forcing that weakens the temperature increase in the atmosphere temporarily.

The total forcing ΔF due to the AHF can be calculated via

$$\Delta F(lat,\, lon) = P_\text{hum}(lat,\, lon) \cdot \text{Fr}_\text{land} + (-\Delta\alpha_S(lat,\, lon) \cdot S(lat)) - \Delta\text{OHU}\ , \tag{4.9}$$

where the mean, latitude-dependent solar radiation $S(lat\ \theta)$ from equation (3.7) is used. Figure 4.23 shows a comparison of these forcings over the next century given a continued 2%-growth of the AHF.

The forcing associated with the ice-albedo feedback (cyan line) is in the same range as the P_{hum} forcing (red line) until 2000, and, later, makes up slightly less than half of the total forcing near the end of this century in the run with continued 2%-growth (Figure 4.23). The change in the globally averaged ocean heat uptake ($\overline{\text{OHU}}$) (blue line) is slightly smaller than the forcing from the ice-albedo feedback but also grows exponentially.

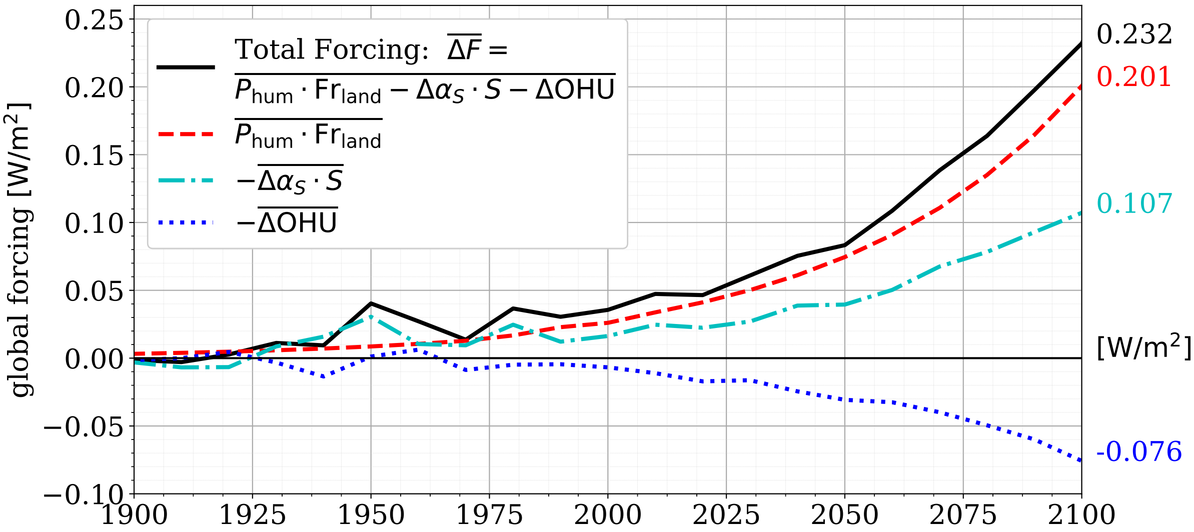

Figure 4.23: Total forcing $\overline{\Delta F_{\text{tot}}}$ [W/m^2] including the direct $\overline{P_{\text{hum}}}$ forcing (red), the consequent additional forcing from the ice-albedo feedback (cyan) and the negative (transient) feedback from changes of the ocean heat uptake $\overline{\Delta\text{OHU}}$ (blue).

In total, the resulting forcing is slightly larger than the direct P_{hum} forcing input. This explains to some degree the previously stated deviation of CLIMBER's result in comparison with the EBMs (relation in equation (4.4)) that do not consider the ice-albedo feedback (in the case of BsD$_{-10}$ with $\Delta\theta = 1°$ resolution or the EBM-0D) and/or neglect the negative feedback from the increased ocean heat uptake (all EBMs). The forcing contributions in 2100 are summarised in Table 4.1.

P_{hum} scenario	$\overline{\text{Direct}}$	$\overline{\text{OHU}}$	$\overline{\text{Ice} - \text{Albedo}}$	$\overline{\Delta F_{\text{tot}}} - \overline{\text{OHU}}$	$\overline{\Delta T}$
2% growth	0.201 W/m^2	−0.076 W/m^2	0.107 W/m^2	0.232 W/m^2	0.086 K

Table 4.1: All forcing contributions in 2100 for the AHF forcing (assuming a continued growth after 2010). The forcings amount to a total $\overline{\Delta F_{\text{tot}}}$, which is slightly higher than the original direct forcing. The resulting transient global mean temperature increase from the AHF is 0.086 K.

4.4.5 Runs with Artificial P_{hum}-Distribution

Description of the Scenarios. The following part of the analysis of CLIMBER aims at investigating the influence of the location of the anthropogenic heat emissions on the forcings, i.e. the direct AHF, the ocean heat uptake and the sea-ice response. This further helps to understand the processes that lead to a certain global mean temperature change.

For this, several artificial scenarios are defined, which assume that all energy is used (and, therefore, transferred to additional heat) in only one cell, namely in the US (Chicago and New York), Australia (Sydney), the EU (Germany), Vancouver area or in the North East coast of China (Shanghai), respectively. Since some of these cells are at different latitudes, they also differ in the size of the area. Furthermore, the land fraction is not necessarily the same in these cells. Nevertheless, in order to compare these scenarios, the specific P_{hum} in each of the cells is inserted such that the global mean AHF $\overline{P_{\mathrm{hum}} \cdot \mathrm{Fr}_{\,\mathrm{land}}}$ is the same in each scenario. Then,

$$P_{\mathrm{hum}}\,(cell)\,[\frac{\mathrm{W}}{\mathrm{m}^2}] \,\cdot\, \mathrm{Fr}_{\,\mathrm{land}}\,(cell) \,\cdot\, \cos\,(lat) \;=\; \mathrm{const.} \qquad\qquad \forall\ \text{`artificial'}\ \text{scenarios}\,, \tag{4.10}$$

where *cell* is the specific cell in which all energy dissipates as heat. Again, the direct forcing in each cell grows with 2% per year after 2010. E.g. in 2100 $P_{\mathrm{hum,\ EU}}$ is 74.4 W/m^2, whereas $P_{\mathrm{hum,\ Australia}}$ is 88.1 W/m^2. In both cases, though the global mean average is the same: $\overline{P_{\mathrm{hum}} \cdot \mathrm{Fr}_{\mathrm{land}}} = 0.201\,\mathrm{W/m}^2$.

This analysis would be a lot easier and more straight forward to interpret if same-sized (land) regions could be used for different latitudes instead of the differently sized cells in the CLIMBER grid. Then, the AHF could be inserted such that the same amount of P_{hum} forcing (on the same area) is inserted in all 'artificial' regions.

Differences in the Temperature Change Depending on the Location of the Forcing. Figures 4.24 to 4.26 show the temperature changes in three of these simulations in the year 2100. The other cases are not shown here but can be easily reproduced.

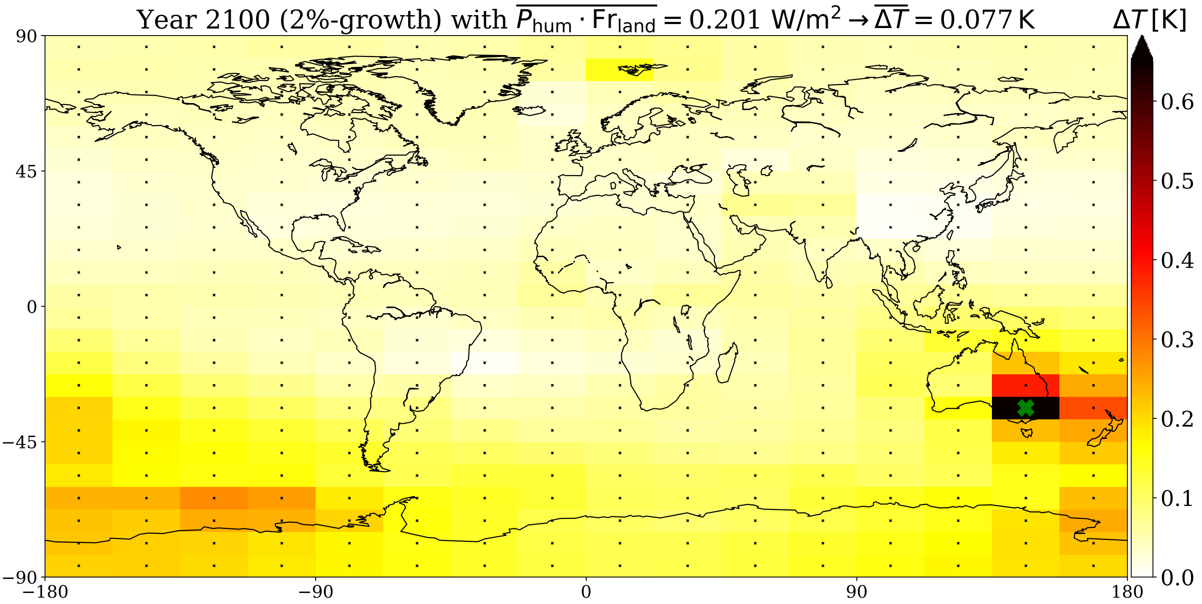

Figure 4.24: Temperature change in 2100 if all energy dissipates as heat in one cell (green cross) in Australia (at latitude 33.75°S).

First of all, while the 'EU' and 'Vancouver' cases (both at 48.75°N but with different land fractions in the specific cell) result in a global mean temperature change of roughly 0.095 K and 0.096 K, the heat emissions from 'Australia' or 'China' (both at 33.75°S/N) lead to only 0.077 K and 0.078 K global mean temperature change. The 'US' (41.25°N) response is in between, with 0.89 K. These results imply a strong dependency of the (transient) temperature increase on the latitude of the AHF emission: The further away from the equator, the higher the global mean temperature response.

The local temperature changes in the specific cell with the heat emissions reach 1.4 K (for 'China' and 'Australia' case) or 1.7 K (for 'Vancouver' case) and 2.2 K (for 'EU' case).

Interestingly, the temperature response in Spitzbergen is exceptionally strong independent of the location

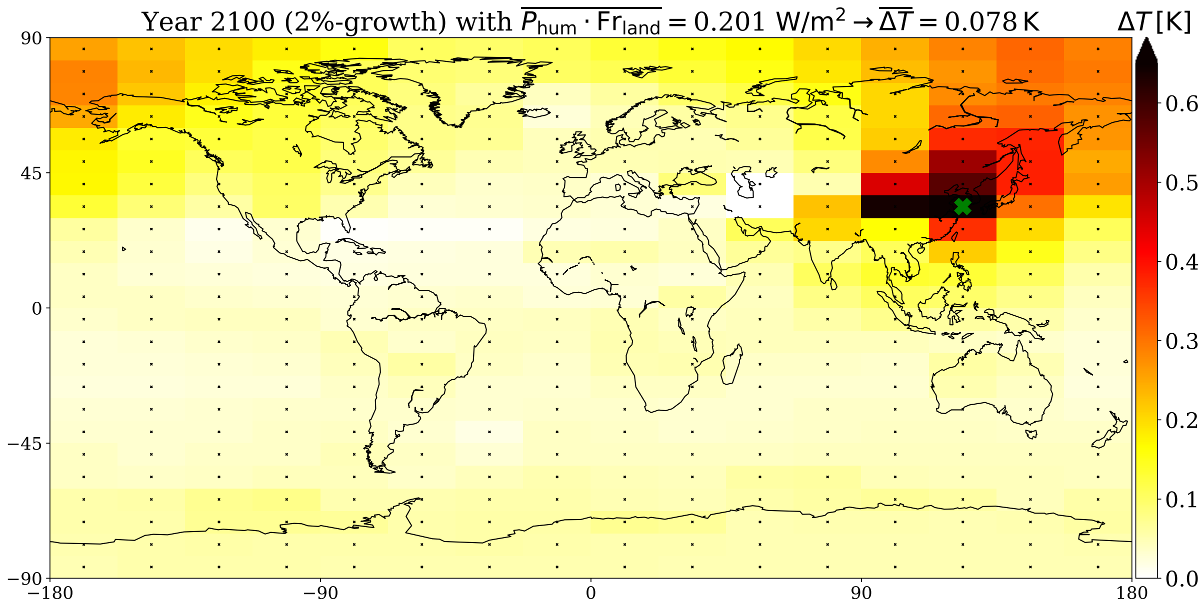

Figure 4.25: Temperature change in 2100 if all energy dissipates as heat in one cell (green cross) in the Shanghai region in North East China (at latitude 33.75°N).

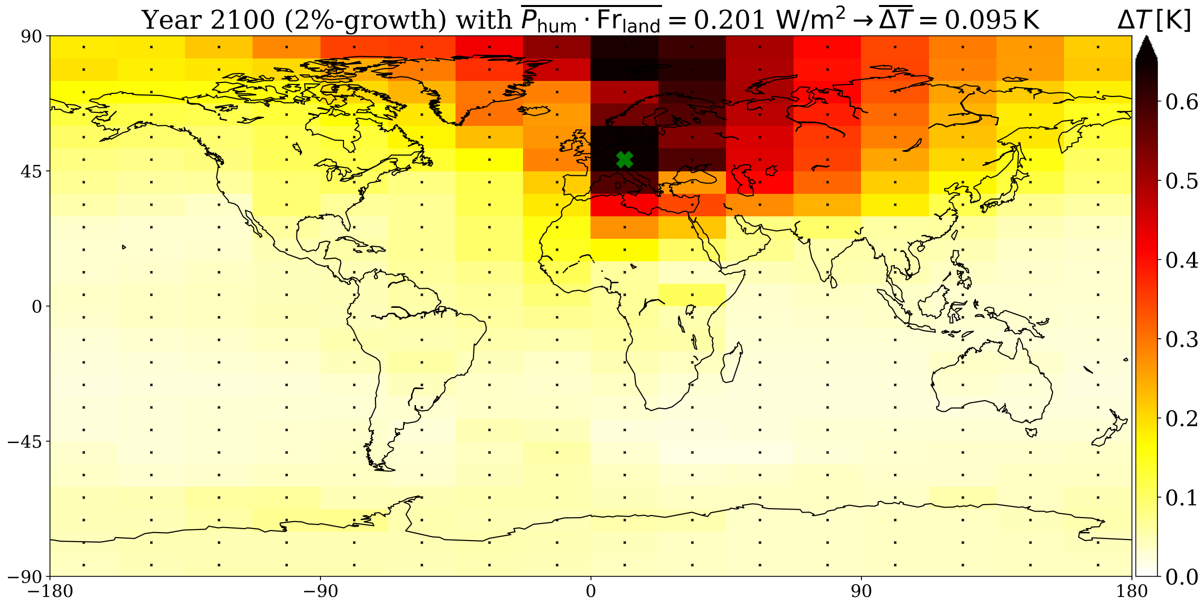

Figure 4.26: Temperature change if all energy dissipates as heat in one cell (green cross) in the EU (at latitude 48.75°N).

of the P_{hum} forcing. Even in the 'Australia' case a temperature increase of 0.15 K is reached in that cell, roughly four times the average of the Northern Hemisphere temperature increase. As described before, this is a consequence of the impact of the AHF on the subpolar gyre and the AMOC in the North Atlantic.

Anyway, all of these studies show again the large effects due to the polar amplification, whose strength depends on the distance between the equator and the cell with the P_{hum} insertion.

One might have expected that the emissions in the Southern Hemisphere (and in particular in 'Australia') lead to a significantly lower or at least delayed temperature increase. This would have been supported by several arguments:

- There is much less land around Australia. Heat released in the 'EU' or 'US' cell for example can therefore warm the surface air of neighbouring cells instead of being absorbed by the ocean. Indeed, the temperature responses in the neighbouring land cells tend to be much larger than in the neighbouring ocean cells for all cases. However, what seems to happen is that the circulation in the Southern Ocean transports absorbed heat from 'Australia' to cells containing Antarctic sea ice and, thereby, spreading the warming across the Southern Hemisphere and increasing the global mean temperature. The temperature impact is much more locally confined if more land fraction surrounds the specific cell, at which the AHF is released, but this does not necessarily influence the global mean temperature change.
- There are no regions with significant snow fraction in Australia and the surrounding areas. Hence, the albedo change and consequent temperature feedback from the impact on snow patterns is restricted to the cases in the Northern Hemisphere. This is not investigated in further detail but does not seem to make a large difference for the global mean temperature.
- It is generally known that the Antarctic is more persistent and, therefore, the polar amplification weaker than in the Northern Hemisphere. The reasons for this include the surface height of the Antarctic plateau, which impacts meridional heat transport and the water vapour feedback, a weaker surface albedo feedback, differences in the ocean and atmospheric heat transport as well as a more efficient heat uptake in the Southern Ocean (Salzmann, 2017). Especially the latter should be relevant for this transient simulation. The proposition is that some of the additional heat should have been stored (at least temporarily) in the Southern Ocean weakening the immediate impact of the AHF. This will be discussed in the following paragraphs in more detail.

Ocean Heat Uptake. In Section 4.4.3 the changes in the global ocean heat uptake were analysed for the 'real' P_{hum} distribution.

The location of the P_{hum} forcing, in particular, through the ocean fraction and specific ocean circulation patterns in the neighbouring cells, strongly influences the ocean heat uptake. This is investigated in more detail here in the artificial scenarios in CLIMBER with the forcing located in distinct, single cells.

Indeed, as claimed in the last paragraph, Figure 4.27 shows that, globally, more heat is inserted into the ocean in the 'Australia' case than in any other of the presented scenarios. On one hand this decreases the impact of the additional AHF forcing. On the other hand, however, the increased heat uptake warms the Southern Ocean and, therefore, melts more sea ice in the Antarctica, fuelling the ice-albedo feedback and increasing the temperature. The trade-off between the negative forcing from increased ocean heat uptake and the positive feedback from a stronger ice-albedo feedback is briefly shown in Table 4.2, in which all forcing contributions for the artificial scenarios are aggregated.

Anyway, a more detailed and, in particular, locally resolved investigation of the heat flux between the ocean and the atmosphere would be absolutely relevant for further research on the AHF, here. Also the detailed relation between ocean heat uptake and the features of the location of the source (e.g. the land fraction of the cell and its neighbours) could provide interesting insights here.

Differences in the Albedo Impact. Figures 4.28 to 4.30 show the changes in surface albedo for some of the artificial scenarios. In general, the closer the P_{hum} source to one of the polar regions, the stronger the change in surface albedo and the consequent ice-albedo feedback. However, especially in the 'Australia' case, the ice-albedo-feedback from melting Antarctic sea ice is emphasised and nearly as big

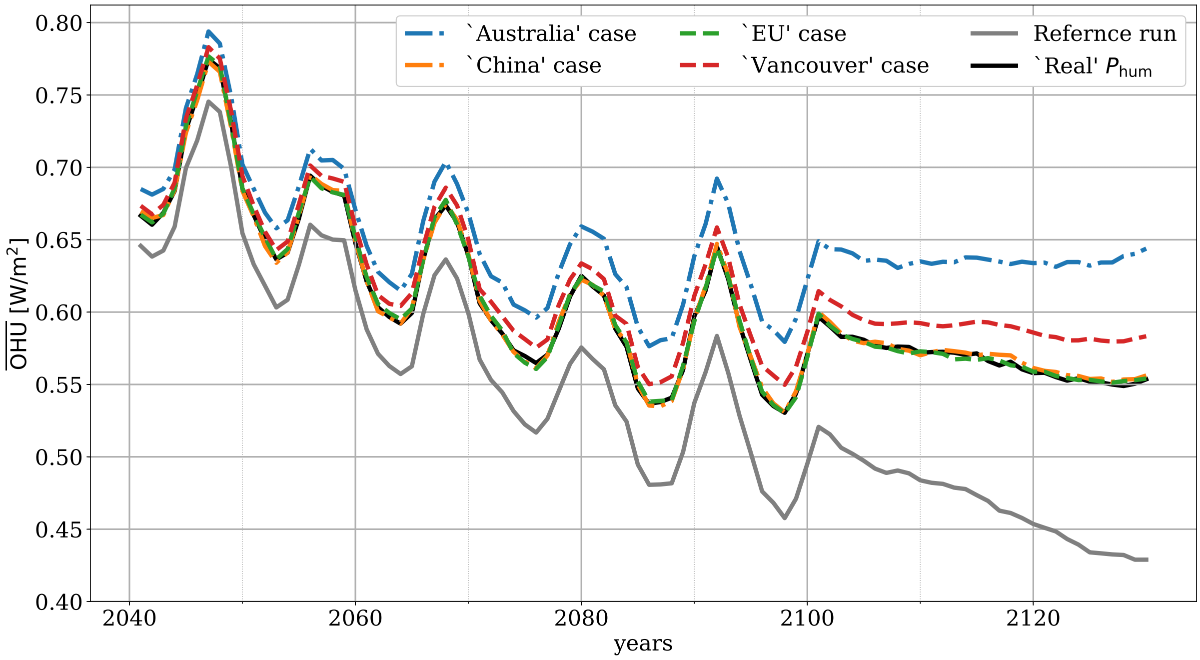

Figure 4.27: Global average heat flux into the ocean $\overline{\mathrm{OHU}}$ over the years in selected artificial AHF scenarios and the previously used ‘real’ AHF forcing (e.g. in Figure 4.6). In all scenarios the AHF increases with 2% per year. The oceans absorb the most heat in total in the ‘Australia’ case, followed by the ‘Vancouver’ case, The absorption in the ‘EU’ and ‘China’ case is equal to the ‘real’ AHF distribution scenario. A first-guess interpretation is that a stronger heat uptake by the ocean leaves less heat to warm the atmosphere. This has to be rejected to some degree as described in the text.

as the albedo change from the P_{hum} emission in Europe, which is 15° closer to the Pole. This stresses the importance of the complex interrelationships between some of the processes in CLIMBER. For reasonable conclusions one needs to look at all forcing contributions, simultaneously. Here, in the ‘Australia’ case, the stronger negative forcing from the ocean heat flux is largely compensated by an increased ice-albedo feedback due to the warmer oceans, as mentioned before.

Next to the map of the albedo change due to the AHF, the evolution of all forcing contributions in the specific case is plotted. This is summarised in the following paragraph in order to draw a comprehensive conclusion.

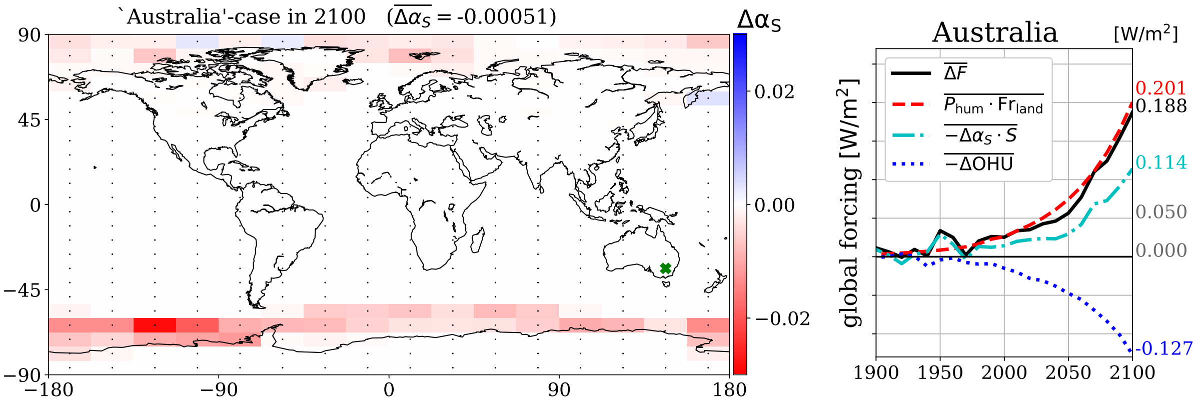

Figure 4.28: ‘Australia’ case (at latitude 33.75°S). Map of albedo changes in 2100 (left) and total forcing with the contributions from the ice-albedo-feedback and the direct AHF effect over time.

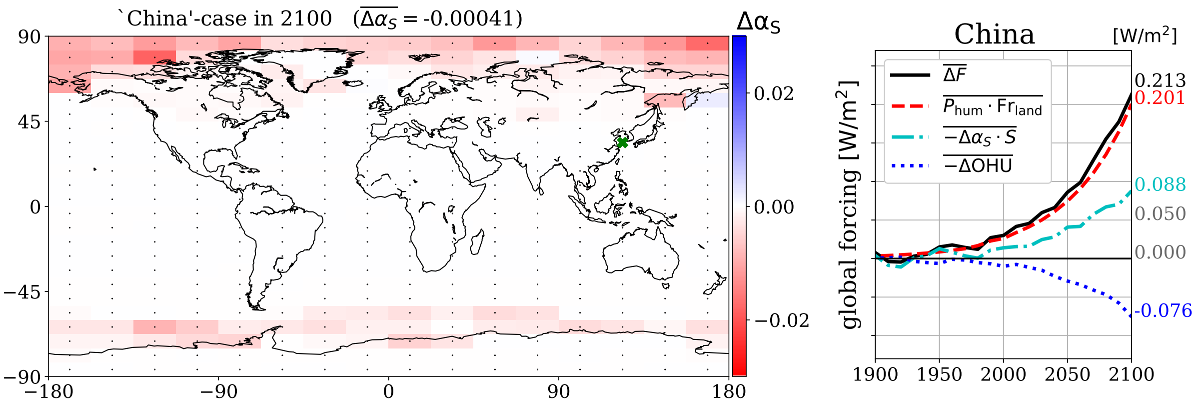

Figure 4.29: ‘North East China’ case (at latitude 33.75°N). Map of albedo changes in 2100 (left) and total forcing with the contributions from the ice-albedo-feedback and the direct AHF effect over time.

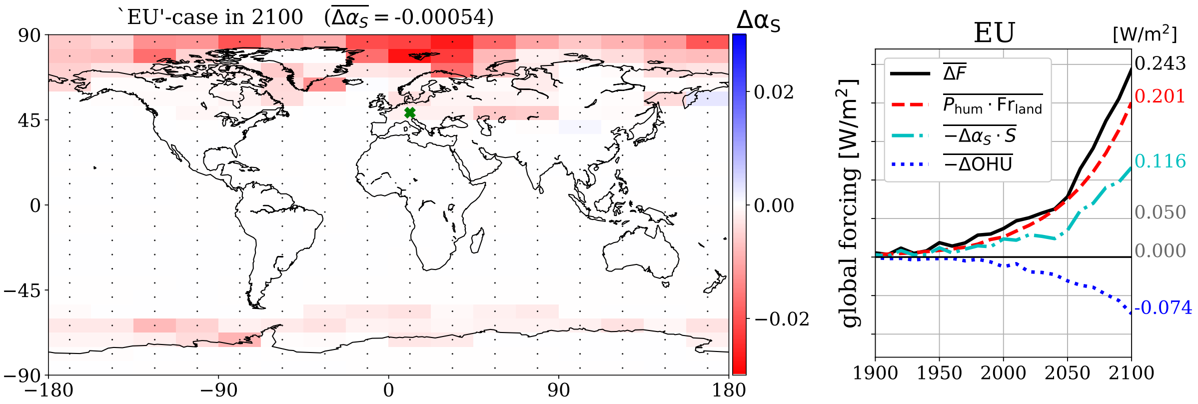

Figure 4.30: ‘EU’ case (at latitude 48.75°N). Map of albedo changes in 2100 (left) and total forcing with the contributions from the ice-albedo-feedback and the direct AHF effect over time.

All Forcings Combined. The contributions to the forcing from the direct AHF, the ice-albedo-feedback, and the ocean heat uptake in 2100 are summarised in Table 4.2.

P_{hum}-scenario	Latitude	$\overline{\mathrm{Direct}}$ [W/m^2]	$\overline{\mathrm{OHU}}$ [W/m^2]	$\overline{\mathrm{Ice-Albedo}}$ [W/m^2]	$\overline{\Delta F_{\mathrm{tot}}} - \overline{\mathrm{OHU}}$ [W/m^2]	$\overline{\Delta T}$
‘Vancouver’	48.75°N	0.201	−0.091	0.137	0.247	0.096 K
‘EU’	48.75°N	0.201	−0.074	0.116	0.243	0.095 K
‘US’	41.25°N	0.201	−0.083	0.107	0.225	0.089 K
‘China’	33.75°N	0.201	−0.076	0.088	0.213	0.078 K
‘Australia’	33.75°S	0.201	−0.127	0.114	0.188	0.077 K
‘real’ P_{hum} (as before)	NA	0.201	−0.076	0.107	0.232	0.086 K

Table 4.2: All forcing contributions in 2100 for the artificial P_{hum} scenarios with the assumption that all AHF is released in one cell. For comparison the values for the ‘real’ P_{hum} distribution is copied. The forcings amount to a total $\overline{\Delta F_{\mathrm{tot}}}$. This total forcing, now, corresponds well with the global mean temperature increase due to the AHF.

In every scenario in Table 4.2 the same global average AHF forcing was inserted. However, the total forcing varies strongly among the different P_{hum} distributions. The calculated total forcing represents accurately the order of the (transient) temperature responses.

A single forcing contribution is not sufficient to make a detailed statement. E.g. in the 'Australia' case the strong increase of the ocean heat uptake is larger than the (also large) ice-albedo feedback, leading to a total forcing that is smaller than the original direct $\overline{P_{\mathrm{hum}}}$ forcing. In all other cases $\overline{\Delta F_{tot}} \geq \overline{P_{\mathrm{hum}}}$.

By comparing the scenarios where the AHF comes from the same latitude ('EU' vs. 'Vancouver' and 'Australia' vs. 'China') in Table 4.2, the statement in Section 4.4.3 about the secondary effect of the ocean heat uptake increase can be confirmed: A larger ocean heat uptake is correlated to a larger ice melting (or ice-albedo feedback). However, the latitude, i.e. the distance of the heat emission to the sea ice, plays a crucial role as well.

Summary While the directly inserted globally averaged AHF forcing is the same in all artificial scenario, in which the P_{hum} forcing comes from one specific cell only, the (transient) temperature responses vary strongly. This is due to a complex interrelationship between the latitude of the AHF emission, the specific features of the surroundings of the AHF emission and the indirect forcing contributions from the ice-albedo feedback and the ocean heat uptake.

In general, the higher the latitude of the AHF emission the stronger the ice-albedo feedback and, therefore, the larger the temperature increase. If the direct neighbours of the cell with the AHF emission have a higher land fraction, the temperature response is more locally confined (with no implications on the size of the global impact). If water surrounds the cell, the ocean heat uptake is increased. This represents a negative (transient) forcing. However, at the same time a warmer ocean can lead to a higher rate of ice melting and, therefore, an increased positive ice-albedo effect. Whether there is a difference in the ocean heat uptake between the Southern and Northern Hemisphere and how the ocean circulation influences this in CLIMBER can not be fully concluded. Anyway, the 'Australia' case supports this statement.

In summary, the position of the AHF emission can play a crucial role in the temperature response in CLIMBER.

4.4.6 Reversibility

The following section investigates coarsely what a sudden stop of the AHF emissions would imply for the global mean temperature. Figure 4.31 shows a scenario, in which the AHF grows continuously with 2% per year but then, in 2130, the AHF is set to zero ($P_{\mathrm{hum}} = 0$) for all cells, e.g. because humanity disposes all AHF into space (e.g. by performing all computer simulations on clusters in space). The temperature reacts immediately as soon as the forcing is removed and the temperature change to the reference run is reduced. In some cells, the temperature even overshoots, i.e. it is lower than the temperature of the reference run in the decades following the AHF shut down. In cells, where sea ice melted due to the AHF, the temperature (and the ice) recovers only slowly. This holds especially for the sea ice in the Antarctica, where, several decades after the shut down of the AHF, the albedo alteration from the loss of sea ice is still nearly as strong as in 2130 in some cells (not shown). This seems plausible as the ice in the Antarctica is more persistent and inert than the Arctic ice, as mentioned before.

By the year 2250, 120 years after the shut down of the AHF in this scenario, 6% of the global mean temperature change from 2130 still remains.

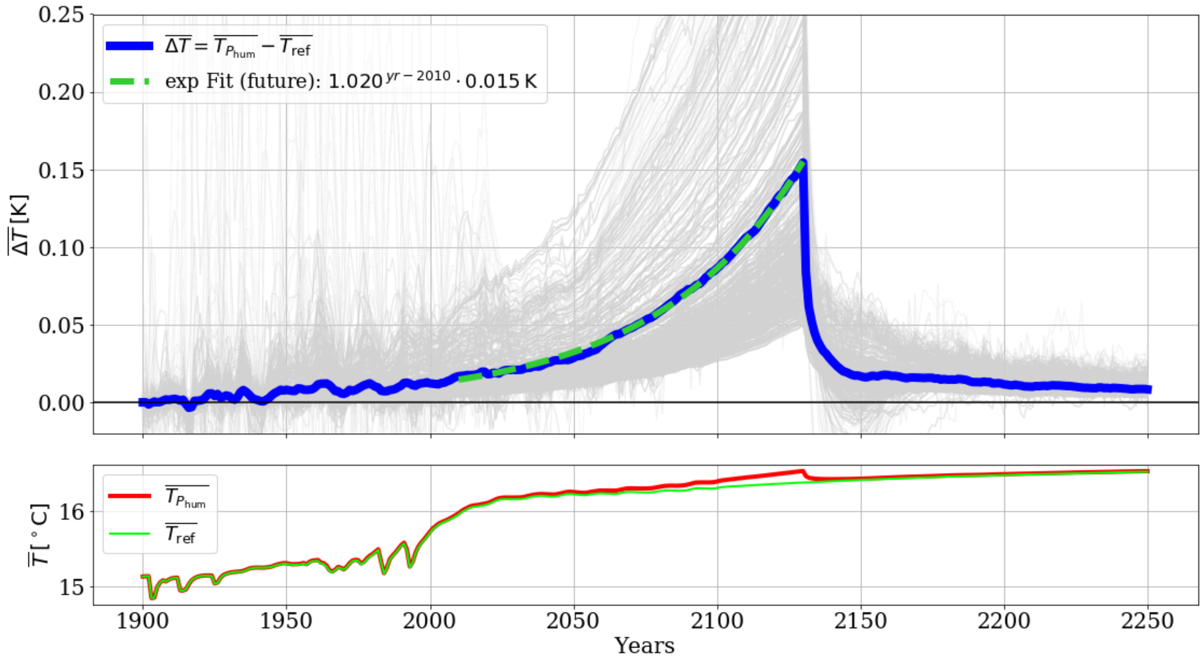

Figure 4.31: **'Vanishing AHF':** P_{hum} is increased with 2% per year and then vanishes after 2130 for whatever reason. The temperature drops back to a low level, but due to the inertia and long-term responses from the oceans and the sea ice, it takes more than a century to regain the equilibrium from pre-industrial times ($P_{\mathrm{hum}} = 0$).

4.4.7 Atlantic Meridional Overturning Circulation (AMOC)

In principle, continuing the increase of the AHF forcing far beyond this century does not yield significantly new results. CLIMBER has many prescribed parameters like the glacier fractions, which are not calculated dynamically, and, therefore, cannot reproduce tipping behaviour well. However, tipping most certainly is a crucial feature of long-term climate impacts (Steffen et al., 2018). The only relevant tipping element of the climate system implemented in CLIMBER is the meridional overturning circulation in the ocean module, MOM3. The impact of the AHF on the Atlantic Meridional Overturning Circulation (AMOC) is investigated in the following.

CLIMBER's ocean module simulates dynamic heat fluxes in the ocean on several layers. From this, the strength of the AMOC, which transfers large amounts of heat from warm, equator-near regions to the north parts of the Atlantic, can be inferred. There is a large debate about a possible decline of the strength of this circulation under global warming (e.g. Caesar et al. 2018). The major factor contributing to a possible slowdown of the AMOC is an increase of freshwater influx into the ocean in the Arctic region from ice melt, which affects the salinity, temperature, and, consequently, density patterns in the North Atlantic and, thereby, slows the 'engine' of the overturning process (Rahmstorf et al., 2015).

In this thesis, the maximum northward heat transport in relevant vertical layers ranging from roughly 600 m (to avoid wind driven fluxes at the surface) to 3000 m depths between $20° - 60°$N is taken as an indicator for the strength of the circulation. This method is very similar to previously used calculations of the AMOC strength e.g. in Medhaug and Furevik (2011).

In Medhaug and Furevik (2011) the AMOC strength from the models analysed is in the range of $13 - 24.3\,\mathrm{Sv}$ ($= 10^6\,\mathrm{m^3 s^{-1}}$). The authors additionally state that measurements give an AMOC strength of $14 - 18\,\mathrm{Sv}$ at 24°N. The reported observed AMOC strength (including the wind-driven Ekman transport) in (Smeed et al., 2014) is in a similar range (e.g. 18.9 Sv in 2004-2007 and 16.2 Sv in 2008-2011) with large fluctuations. With an AMOC strength of $15 - 16$ Sv, the CLIMBER simulations performed here are well within this range (see Figure 4.32). The maximum flux is at 35°N and at roughly 780 m depth for all runs. Figure 4.32 shows the (dynamic) evolution of this indicator of the AMOC for the reference run without P_{hum} compared to the run with a 2% increase of P_{hum} per year until 2250. The AMOC strength itself (left plot) has a large inter-annual variability, which is driven by buoyancy fluxes at the western, ice covered boundary of the ocean, as described in Buckley and Marshall (2016). However, a decreasing trend of the AMOC strength due to the AHF (right plot) is clearly visible. A decrease of the overturning circulation is in general associated with decreasing temperatures in the Northern Hemisphere, which might offset some of the temperature increase from the growing AHF forcing. The change is also closely associated with the subpolar gyre in the North Atlantic that is responsible for the fluctuations of the global mean temperature in Figure 4.6 as discussed in Figure 4.12 and in Section 4.4.1. However, a detailed analysis of these complex interrelationships between the climate and the ocean circulation is beyond the scope of this thesis.

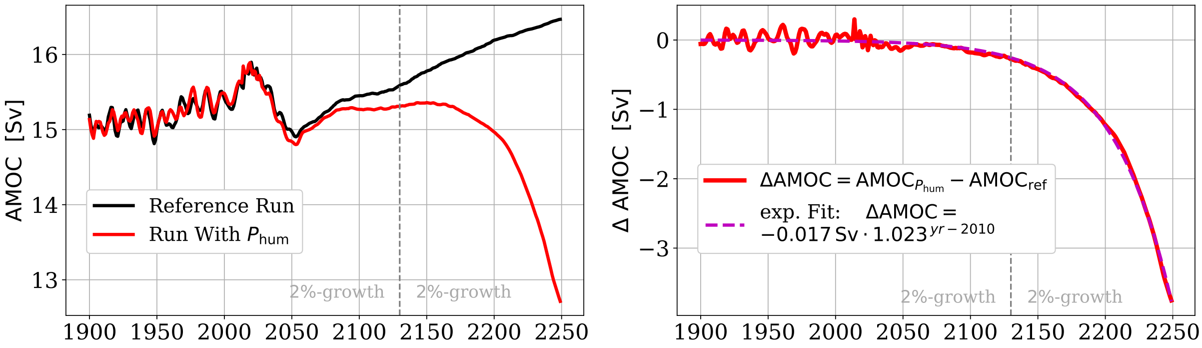

Figure 4.32: Simulation of the strength of the AMOC (indicated by the maximum of the stream function in the relevant depths and latitudes) for a run without P_{hum} and a run with a 2%-increase of P_{hum}. The exponential fit to the decrease of the AMOC strength is in good agreement. The fitting parameters indicates an AMOC slowdown by -0.4 Sv per W/m^2.

In the equilibrium run, in which the P_{hum} emissions are kept constant after 2130 (given a 2%-growth until 2130, i.e. $P_{\text{hum}}(yr \geq 2130) = 0.36\,\text{W/m}^2$), which is described in the beginning of this chapter and shown in Figure 4.7, the system approaches a state in which the AMOC strength is 0.26 Sv smaller than in the reference run (not shown).

The run in Figure 4.33 shows the change in AMOC for the case in which $P_{\text{hum}} = 0$ after 2130, i.e. the same run as shown in Figure 4.31 that investigates the reversibility of the AHF impacts. The circulation strength increases strongly again after the shut down of the AHF. Hence, the AMOC is not (yet) tipped by the AHF in this scenario in 2130. In fact, some process in the AMOC overshoots and the obtained circulation strength is even stronger than the reference AMOC in the second half of the 22$^{\text{nd}}$ century. It would be interesting at this point to investigate at what additional forcing from the heterogeneous P_{hum} the AMOC in CLIMBER tips and is irreversibly smaller than in the reference run even if the forcing is shut off.

Due to the local forcing from the EU and North America close to the AMOC, the impact of the AHF on the circulation strength is especially relevant and enhanced.

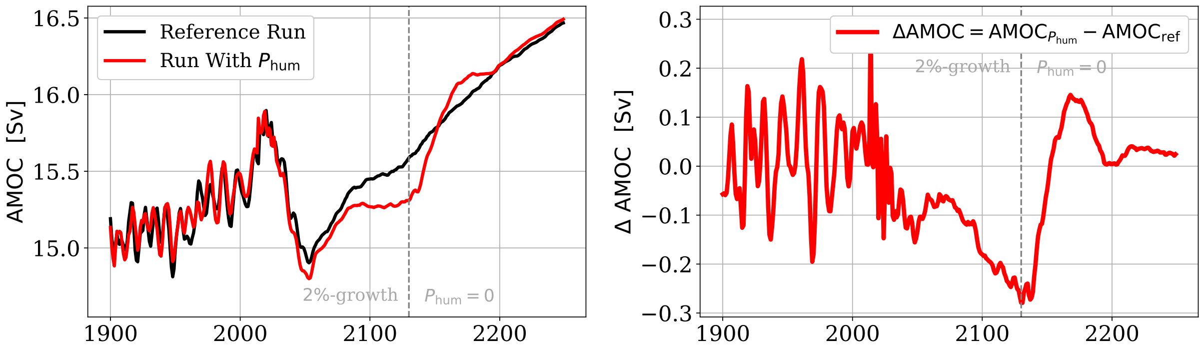

Figure 4.33: Simulation of the strength of the AMOC (indicated by the maximum of the stream function in the relevant depths and latitudes) for a run without P_{hum} and a run with a 2%-increase of P_{hum} until 2130 and $P_{\mathrm{hum}} = 0$ afterwards.

4.4.8 Simultaneous Increase of CO_2 and P_{hum}

So far, the CO_2 concentration after 2010 in all CLIMBER runs has been kept constant at the 2010 level. As before in the last paragraphs of Section 2.3 and Section 3.3.2, the effects of a scenario, in which both the P_{hum} and the CO_2 concentration increase simultaneously, are analysed in CLIMBER.

$$\Delta T_{\mathrm{P}+\mathrm{CO}_2} \overset{?}{\geq} \Delta T_{\mathrm{P}} + \Delta T_{\mathrm{CO}_2} \tag{4.11}$$

The previous models, EBM-0D and EBM-1D, show a very small additional temperature amplification if both variables are increased simultaneously compared to runs with separate growth scenarios. The reason for this is the secondary feedback that the P_{hum} forcing is additionally absorbed and re-emitted by the increased greenhouse gases in the atmosphere. Furthermore, the simultaneous increases of the greenhouse effect and the AHF forcing in the EBM-1D can transgress a threshold that triggers the sea ice to disappear completely (see Table 3.4). This special case, naturally, leads to a very large temperature amplification.

In CLIMBER, a 2%-growth of the AHF and the CO_2 increase according to the (original) SSP5-baseline scenario are investigated. The following four CLIMBER runs are relevant: A reference run, a run with increasing P_{hum} but constant CO_2, a run with increasing CO_2 but constant P_{hum}, and a run with simultaneously increasing CO_2 and P_{hum}. The results are shown in Figure 4.34. The plots show – in the direction of the arrows – the absolute temperature of the four runs, the corresponding temperature changes to the reference run, the temperature changes due to the reference run without the CO_2 contribution ('non-CO_2 temperature response'), and, finally, the difference between this 'non-CO_2' temperature increase in the P_{hum} run and in the simultaneous run, which determines the question mark in equation 4.11.

The theory described in the analysis of simultaneous increases in the EBMs before, suggests that this signal should be positive and exponentially growing (i.e. that equation (4.11) holds). However, no clear signal can be derived from these runs. In fact, the temperature change of the simultaneous run is even lower than in the run with constant CO_2-concentration.

There are multiple reasons why CLIMBER does not give the same result of a temperature response amplification for the simultaneous increase: E.g. increasing the CO_2 concentration according to the SSP5-baseline scenario leads to a significant change in the snow fraction. This has been identified as one (minor) driver of the climate impact of the AHF. Hence, the increased greenhouse effect in the simultaneous run interferes with the climate impact of the P_{hum} forcing and, therefore, reduces its ability

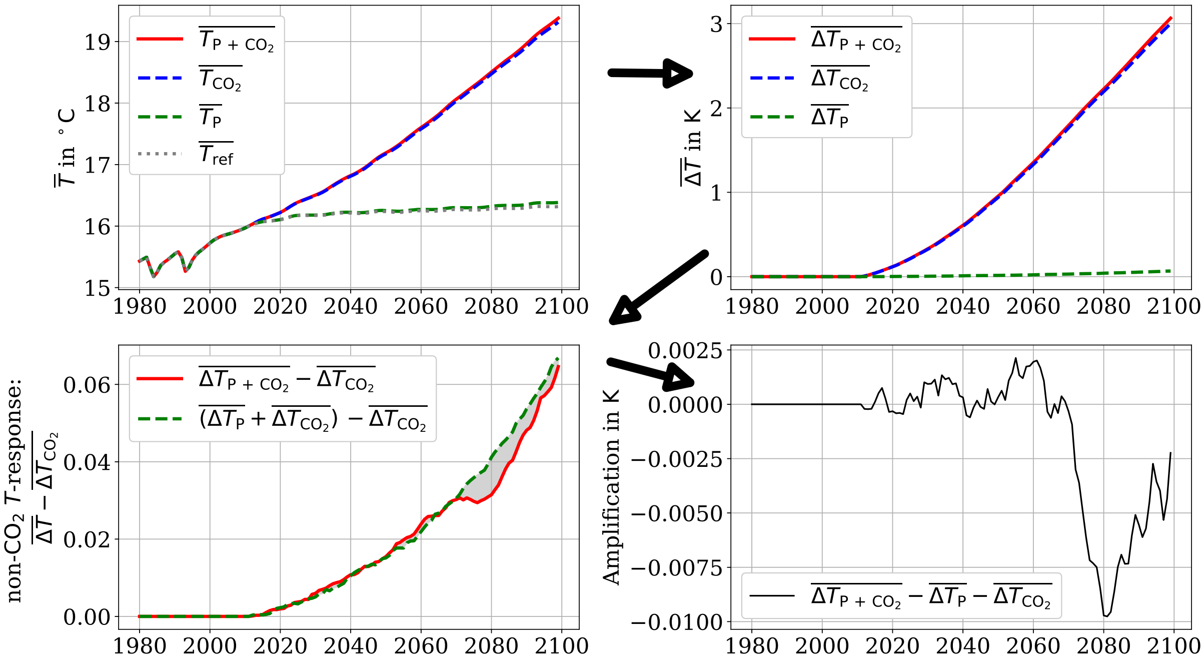

Figure 4.34: The amplification of the AHF temperature impact due to simultaneous CO$_2$ growth (bottom right) and the derivation of it, which is described in detail in the main text. Four different runs are used: A reference run with $P_{\mathrm{hum}}(t > 2010) = 0.034\,\mathrm{W/m^2}$ and $\mathrm{CO_2}(yr > 2010) = 388.75\,\mathrm{ppm}$ ($\rightarrow T_{\mathrm{ref}}$), a run with constant CO$_2$ but increasing P_{hum} ($\rightarrow T_{\mathrm{P}}$), a run with constant P_{hum} but increasing CO$_2$ ($\rightarrow T_{\mathrm{CO_2}}$), and, finally, a run with simultaneous P_{hum} and CO$_2$ increase ($\rightarrow T_{\mathrm{P+CO_2}}$). The upper left plot shows the absolute temperatures in $^\circ C$. The CO$_2$-related temperature increase is clearly dominant over the P_{hum}-related increase. The plot to the right shows the differences of each of the three perturbed runs to the reference scenario, T_{ref}. Next, the bottom left plot illustrates all of these runs subtracted by the temperature response that arises from the pure CO$_2$ increase, i.e. the lines represent the 'non-CO$_2$ temperature response' of all runs. The difference between these non-CO$_2$ responses of the $T_{\mathrm{P+CO_2}}$ and the T_{P} run, which is indicated by the filled grey region, is then plotted on the right. This term represents what has previously in this thesis (Chapters 2 and 3) been referred to as 'amplification of the AHF temperature impact due to simultaneous CO$_2$ growth'. Here, however, there is no amplification, but rather a weakening of the AHF temperature impact due to the simultaneous CO$_2$ increase (see main text).

to impact the climate. Furthermore, the complex interrelationship of the weakening of the AMOC and the consequent change of ice extent in the Northern Hemisphere, might dominate the relation in equation 4.11.

Apparently, in the decade around 2070 the $T_{\mathrm{P+CO_2}}$ scenario exhibits some odd behaviour, which might have to do with these multiple, inter-connected processes. This is not pursued further. In summary, however, the effects of simultaneously increasing CO$_2$ and P_{hum} forcing, again, seem to be of minor relevance in CLIMBER under the given scenarios.

4.5 Summary

Starting from the conceptual models in Chapters 2 and 3, this chapter describes the AHF in a climate model of intermediate complexity, CLIMBER-3α. This makes the modelling of a two-dimensional AHF forcing possible by distinguishing between separate world regions. This is especially relevant for the AHF, since, in contrast to most forcings like the greenhouse effect or even aerosol injection from volcanic eruptions, the AHF produces a strong locally confined forcing.

For future projections, two scenarios are simulated: A simple 2% growth with today's AHF distribution and a more elaborate scenario based on the Shared Socio-Economic Pathways (SSP5).

The global-scale results presented above from CLIMBER-3α are very similar to those obtained from the Energy Balance Models. In fact, the temperature response to a tenfold increase of today's AHF in the intermediate complexity climate model is comparable to the two most realistic and conservative configurations of the EBM-1D. This emphasises the importance of the ice-albedo effect resulting from melting sea ice and reduced snow covered areas.

However, there are several additional findings from CLIMBER-3α:

- The ice melting is strongly localised and connected to the circulation patterns of the oceans and, furthermore, depends on the location of the AHF.
- Also, the ocean heat uptake acts as a negative forcing on the transient temperature response in the same order of magnitude as the ice-albedo feedback.
- These two secondary processes, the ice-albedo feedback and the increased ocean heat uptake, are correlated with each other and the trade-off strongly depends on the location of the AHF forcing. E.g. for AHF emissions in the Southern Hemisphere both contributions are especially pronounced.
- Thus, the total forcing arising from the direct AHF can be calculated including these major feedbacks. In general, the resulting forcing is slightly higher than the direct forcing.
- The latitude, the surrounding cells (ocean or land), and specific features like circulation patterns in the ocean near the AHF emission play a significant role in determining the impact of the AHF from a specific location.
- In general, increasing the AHF leads to a smaller Atlantic Meridional Overturning Circulation. However, large fluctuations are observed in these circulations in the model output even today, with a relatively small AHF forcing due to a complex interaction between the subpolar gyre, the AMOC and the additional forcing. This impact of the AHF is already relevant for today's sea ice dynamics in CLIMBER and, via the ice-albedo feedback, even for fluctuations in the global mean temperature.

CLIMBER-3α has a relatively coarse spatial resolution and many processes are not calculated dynamically but are prescribed, making simulations faster and easier to understand. Some results might, therefore, be overestimated or oversimplified. Especially fluctuations, e.g. in the dynamics of the AMOC, should be treated carefully.

However, inserting the AHF into CLIMBER-3α and analysing the climate impacts gives more various and valuable insights in the processes involved and extends the understanding of the impacts of heterogeneous AHF forcing. It also helps to estimate global mean temperature impacts of energy scenarios for the next century, in which both local and global impacts due to the AHF may become a non negligible factor in climate change, given the humanity manages to reduce the greenhouse gas emissions to zero early enough to avoid much larger global warming from the greenhouse effect.

Chapter 5

Challenging the Assumption that All Energy Sources Contribute to the AHF

In this thesis so far, the assumption was made that the total primary energy contributes to the AHF independent of the energy source. As often stated before, this assumption is not correct. This chapter will look more into which energy sources actually constitute the AHF.

In the introduction a more adequate definition of the AHF was established: The AHF consists of dissipated waste heat from those energy sources that insert additional energy into the Earth System. An energy source can be classified as (1) purely additional heat (contributing to the AHF), (2) partially additional heat (partially contributing) and (3) barely any additional heat (not contributing).

5.1 Limits of the AHF Contribution

Looking at future technological innovations, there are some limits imposed as to how much an energy source can contribute to the AHF. The efficiency limit and the availability limit.

Primary vs. Consumed Energy - The Efficiency Limit. The efficiency of the energy production strongly influences the minimum amount of AHF released per useful unit of energy. Currently, roughly only 2/3 of the primary energy are used to fulfil our society's needs, while 1/3 contributes to the waste heat immediately (IEA, 2014). In fact, the fraction of really 'necessary' energy to sustain our current civilisation is even smaller if the demand-side efficiency of the devices that use this primary energy is also taken into account.

The thermodynamic laws set an upper limit on the efficiency of the extraction of usable energy from primary energy sources, e.g. the thermodynamic efficiency limit for solar PV energy conversion.

For the thermal power plants which create electricity from heated fluids (such as in nuclear, solar thermal or fossil fuel power plants) the Carnot Limit is the (unreachable) theoretical upper bound. However, the conversion of gravitational potential to electricity or other usable energy (such as in a hydroelectric power station) can, in principle, reach an efficiency close to one, for example.

Geophysical Limits of the Availability. Secondly, there are also geophysical (next to social or economic) limits to the amount of energy that can be extracted from a certain energy source. Together, the limits set an upper boundary of the AHF for each source.

The derivation of the availability limits in the natural sciences ranges from climate model based approaches to theoretical, thermodynamic arguments. An extensive review on the various theories or approaches could be very valuable for the modelling part in this thesis in order to provide comprehensive limit scenarios. In fact, one might even try to define Planetary Boundaries for different energy sources, e.g. taking the AHF into account or more elaborately all climate impacts (similar to Jakob and Hilaire 2015).

In the following, one example of a theoretical framework describing such limits is often employed: The concept of free energy generation in Kleidon (2012). Free energy is the amount of energy that is available to be extracted as work in a system rather than to dissipate to heat (Atkins, 2010). Kleidon (2012) uses this concept of the free energy balance together with the calculation of the entropy as a tool to budget the available energy from different sources. A very short description of the framework and consequences can be found in Appendix A.7.

The approach presented in Kleidon (2012) results in much tighter limits as to how much energy the civilisation can consume compared to standard approaches (e.g. Marvel, Kravitz, and Caldeira 2013). Similar methods that also use a purely physically based framework could be very relevant to identify global limits. However, more studies like this should be performed in order to obtain consensual statements.

A more applied (but traditional) set of estimates is given, for example, in Jacobson and Delucchi (2011). The authors suggest a full transition to a wind, water and solar powered energy mix by 2050. The feasibility of their transition pathway is supported through the calculation of the maximum extractable power of each of the energy sources and the required area and material for the technology. According to their estimates, the potential of solar and wind power alone can power our civilisation's global energy demand multiple times.

5.2 Overview of the AHF Contribution of Different Energy Sources and Associated Limits

In the following, the major energy sources are discussed individually with respect to

- why they contribute to the AHF or not
- their actual contribution to the AHF limited by the efficiency of energy extraction and
- estimations of the amount of available energy from the source.

In order to quantify the contribution to the AHF (second bullet point), the AHF factor ζ is defined for each energy source via the ratio of the AHF over the useful energy consumed by the civilisation in this process. In order to compare the results of different energy sources, the 'consumed useful energy' refers to electrical energy in the definition:

$$\zeta = \frac{\text{AHF}}{\text{consumed electrical energy}} \tag{5.1}$$

Note, this does not include secondary energy use, such as district heating from waste heat or re-using energy, like the charging of a car battery while driving downhill. Both aspects decrease the ζ by making use of the AHF or decreasing the AHF output of a process.

A lower AHF factor is of course desirable. However, this is constrained by the efficiency limit in the second bullet point. Furthermore, the availability of energy from a certain source sets an limit on the energy mix and, hence, the global AHF-factor.

There are numerous studies on the topics and statements presented in the following. Two examples of theories on these aspects are described in more detail: First, a simple calculation to estimate the AHF contribution of solar PV cells and, secondly, two approaches for estimating the maximum extractable wind power. Similar approaches could also be applied to all other energy sources in order to develop a comprehensive picture of the (possible future) AHF impact.

5.2.1 Fossil Fuels

The current primary energy mix consists of roughly 82% fossil fuel driven combustion (IEA, 2014).

- By burning fossil fuels, the energy from geologically stored plant material is depleted that was created by solar energy millions of years ago. Strictly speaking, this would imply that on the long-term no additional heat is released into the atmosphere. However, the rate of combustion vs. the storage of new coal reservoirs today is so high (see e.g. Andrews 2013) that it makes sense to look at short timescales only, in which the fossil fuel energy is completely converted to additional heat to the system.

- Due to the efficiency η_{FF} of combustion, the AHF released is larger than the actually consumed energy by a factor of $1/\eta_{\mathrm{FF}}$. Today, fossil fuel power plants convert the primary energy into electricity with an average efficiency of 36% (IEA, 2008). Hence, the AHF-factor in this case is roughly $\zeta = 3$, i.e. one releases three times the energy than the amount that is actually used, e.g. to get from one place to another.

  Note that there is a small fraction of primary energy from fossil fuels in the statistics (6% in 2010 in IEA 2014) that is used for so-called ‘non-energy use’, i.e. this fraction is consumed as a raw material rather than for the purpose of gaining utilisable energy. This covers mainly the conversion of oil or coal into new chemical forms, like the production of paraffin wax or coal tars. Since this energy is stored and does not dissipate as heat on a short timescale, technically, it does not contribute to the AHF. However, this is neglected here.

  Over the past decade the efficiency of combustion has slightly improved from 33% to 36%. Some technologies have efficiencies up to 46% and the efficiency of some power plants is expected to reach 50% (Vatopoulos et al., 2012).

- There has been a lot of discussion about the availability of fossil fuels (‘Peak Oil’, e.g. in Sorrell et al. 2010). However, no consensual ultimate limit of the reserves could be identified yet. In fact, the estimates for proved natural gas reserves have been growing over the last centuries, e.g. due to new extraction technologies like fracking (BP, 2016).

It is not the AHF process described here directly contributing to the warming, but the release of CO_2 and its indirect corresponding climate impacts after the combustion of fossil fuels, that is currently the dominant reason why fossil fuels cannot be part of a future sustainable energy mix (Jakob and Hilaire, 2015), however large the reserves are. In fact, Winkelmann et al. (2015) show that immense climate change including a complete melting of the Antarctic ice sheet appears before the geophysical limit of availability of fossil fuels is reached.

5.2.2 Nuclear Energy

Nuclear energy, both from fission as well as, potentially, from fusion, clearly classifies as additional heat in the system.

Fission

- For the fission process, one mainly needs the Uranium isotopes, ^{235}U and ^{238}U, which have lifetimes in the range of a billion years. Hence, the rapid release of this chemical energy in a nuclear power plant is an additional energy input into the system.
- Current fission power plants operate at a thermal efficiency of less than 33% (Table 8.1 in EIA 2017), taking into account that a nuclear power plant cannot be fully utilised for energy production all the time, which further decreases the efficiency (the 'Net electrical MWe' power output) (World Nuclear Associtation, 2018). The AHF-factor is accordingly $\zeta \geq 3$.

  Little improvements of the efficiency are observed over the last decade (Table 8.1 in EIA 2017). However, through technology advancements the efficiency is expected to rise. Also, so-called 'breeder' nuclear power plants have a strongly reduced Uranium need, as the fuel can be re-used (Jacobson and Delucchi, 2011).
- The fission process is constrained by the availability of Uranium. In 2010, nuclear energy contributed with roughly 5% to the primary energy consumption (IEA, 2014). According to NEA and IAEA (2016), this fraction corresponds to roughly $56.6 \cdot 10^3$ t Uranium consumed per year. By extrapolating this to the total energy demand, an amount of $1.1 \cdot 10^6$ t Uranium per year would be needed to power our current human civilisation with nuclear power. By using new technologies as described before or other fuels, such as Thorium, which is more abundant than Uranium, the potential can be strongly increased (NEA and IAEA, 2016). Current estimates suggest an availability of 'conventional'[1] Uranium of $13.4 \cdot 10^6\, t$ (NEA and IAEA, 2016). Hence, nuclear power from the fission process of Uranium would not even cover 15 years of today's total worldwide energy production. However, there are likely largely undiscovered (unconventional) resources (NEA and IAEA, 2016), requiring more effort and investment, though. Jacobson and Delucchi (2011) state that Uranium resources in a 'large-scale nuclear program' would exhaust in roughly a century.

One could conclude that the use of current nuclear power plants (not taking Thorium, etc. into account) is more likely constrained by the limited availability of Uranium than by the climate damage due to the AHF. However, a fast and large increase in nuclear power does not only raise physical concerns but also social or political issues including the development of nuclear weapons and the ability to oversee this (Jacobson and Delucchi, 2011). Furthermore, there is the risk of accidents in nuclear power plants and the unresolved problem of long-term storage of radioactive waste.

---

[1] The 'conventional' Uranium resource base includes all available and speculated resources but not secondary sources or 'unconventional' resources such as Uranium in phosphate rocks.

Fusion So far, no project has achieved a net power output from a controlled fusion process. Still, fusion remains a promising hope for many to meet the human energy demand while not emitting greenhouse gases or producing large amounts of nuclear waste.

- In order to initiate the fusion process (i.e. to overcome the repulsion of the two positively charged nuclei) a large energy threshold needs to be transgressed, which barely occurs spontaneously on our planet given the temperatures here. The reaction can be initiated by producing a plasma with high enough temperatures. The fusion energy gained in this process is classified as a purely additional energy input into the system.
- The factors that determine the efficiency of a fusion power plant are numerous: The physical foundation of the fusion process, the technical implementation (e.g. energy for the magnetic field), or the thermal heat engine to produce electricity. An ultimate limit of the efficiency remains subject for further research, especially since, so far, the net power output of all fusion reactors has been negative.
- For fusion, there is no resource limit, because the abundance of Deuterium and Tritium (which can be 'bred' with Lithium) is basically unlimited (Jacobson and Delucchi, 2011). Depending on the exact technology used, there might be constraints regarding other materials needed to deal with the strong magnetic field and the plasma, though.

This analysis suggests that, after reaching a reasonable, positive efficiency in the power plants, the first geophysical limit to fusion power is the consequent AHF and its climate impacts.

5.2.3 Geothermal Energy

- Geothermal energy is extracted from the heat released by the interior of the planet. This energy would naturally be inserted at some point in the atmosphere, however, again on much longer time-scales than through artificial extraction of that heat far below the surface. Hence, a large part of geothermal energy is a contribution to the AHF. Using the amount of energy that reaches the surface and heats the lower atmosphere, however, would not contribute to the AHF.
- Heating through geothermal energy has an efficiency of less than one, e.g. due to the pumping mechanism. Also, the production of electricity from geothermal energy has a maximum efficiency like any heat engine. Hence, the AHF factor is of the same order as for fossil fuels: $\zeta \geq 3$. As stated before, using geothermal energy, which reaches Earth's surface anyway, yields $\zeta = 0$.
- Kleidon (2012) estimates that roughly 40 TW of free energy are produced by Earth's interior, i.e. more than twice the current primary energy production (17 TW). However, most of this energy is used for mantle convection and plate tectonics. Hence, the potential of geothermal energy is very limited. Jacobson and Delucchi (2011) use 45 TW as maximum extractable power, although, according to them, only $0.07 - 0.14$ TW are in 'likely developable locations'. Finally, Davies and Davies (2010) use heat flow measurements all over the surface of the planet to estimate the energy flux from the interior and obtain a value of 47 ± 2 TW.

The climate damage due to the AHF from geothermal energy is limited mainly due to the low power availability and technological challenges to retrieve more power from this energy source.

5.2.4 Solar Power

- The direct use of solar energy through **photovoltaic (PV)** panels or **thermal heating** can be considered as partially additional heat. On one hand, (a part of) the solar power that arrives on the site is converted to electricity and then later dissipates as heat. This makes no difference to the global energy budget compared to the case in which there is no solar panel but the solar radiation immediately dissipates as heat at the same place. However, usually this technique is accompanied by methods to capture more solar power e.g. through mirrors or anti-reflective surfaces. Thereby, a larger fraction of the solar irradiation is kept on earth, that would otherwise have been reflected to space. In other words, solar power technologies often decrease the surface albedo and, thus, insert some additional heat into the system. An example calculation of the contribution is provided below.

- For **solar thermal** panels, the efficiency of collecting the solar radiation and using it to heat some liquid can in principle reach one. However, the thermal efficiency of converting this heat to e.g. electricity needs to be taken into account, which decreases the overall efficiency to ~ 0.3 (and increases the AHF contribution accordingly).

  The energy conversion of a single-junction **PV solar cell**, as mentioned before, has a thermodynamic upper limit of $\sim 30\%$ due to thermalisation losses (Würfel, 2002). For stacked solar panels this can in theory be extended to 86% . However, the latter limit is basically unreachable as it requires an infinite number of layers with different band gaps and 'maximally concentrated' sunlight (which in turn influences the AHF of course) . The 'best' solar cell achieved so far has an efficiency of 44.7% (given maximally concentrated sunlight) (Fraunhofer ISE, 2013). For single junction cells a maximum efficiency of 29% has been reached.

  Example Scenario For PV solar cells, a simple back-of-the-envelope scenario is discussed below to illustrate the potentials and limits of this energy source and calculate the contribution to the AHF. Assume that the total human energy demand is met by solar panels in the Sahara zone. Then, the additional energy inserted into the Earth System comes from the albedo change of the corresponding area. In order to meet the demand for energy consumption in 2010 an average power of $P_{\text{consumed}} = 11.7\,\text{TW}$ is needed (IEA, 2014) (the primary power produced was 17 TW). Thus, with an efficiency of $\eta_{\text{PV}} \approx 30\%$ of a PV solar panel and an annual mean solar irradiation (global horizontal irradiance[2]) of $S = 274\,\text{W/m}^2$ ($\sim 2400\,\text{kWh/m}^2\text{/year}$) in the Sahara zone (at the southern border of Libya) (from Solargis 2016), a total area of $A_{\text{PV}} \sim 1.42 \cdot 10^{11}\,\text{m}^2 = 142,000\,\text{km}^2$ (roughly 8% of Libya) needs to be covered with solar panels. Naturally, the situation is much more complex as factors like transmission losses or any thoughts regarding energy security or fluctuating energy demand and storage are neglected in this estimate. In general, the surface albedo in the Sahara is roughly $\alpha_S = 40\%$ (Donohoe and Battisti, 2011). A solar panel significantly reduces this value; let us assume to $\alpha_S = 0$. According to Donohoe and Battisti (2011), the surface albedo in the Sahara makes up for roughly 50% of the total planetary albedo, which is of the order of $\alpha_P = 40\%$. I.e. by decreasing the surface albedo to zero, the planetary albedo in the Sahara decreases to $\alpha_P = 0.2$, the atmospheric contribution. Thus, a change in the planetary albedo of $\Delta\alpha_P = 0.2$ in the designated area results from the use of the solar panels. An additional heat input of $S|_{\text{A}_{\text{PV}}} \cdot \Delta\alpha_P = 274\,\text{W/m}^2 \cdot 0.2 = 54.8\,\text{W/m}^2$ is emitted to the system from the area covered with

---

[2] The power of the (diffuse and direct) solar radiation that arrives on a $1\,\text{m}^2$-area that is horizontally aligned with the surface.

solar panels. The size of this local AHF is comparable to the values in the CLIMBER-3α simulations with artificial P_{hum}-scenarios in Section 4.4.5 (e.g. the 'EU' case). In total, the anthropogenic energy production emits additional

$$P_{\text{additional}} = P_{\text{consumed}} \cdot \frac{\Delta\alpha_P}{\eta_{\text{PV}}} = 0.66 \cdot P_{\text{consumed}} = 7.8\,\text{TW} \tag{5.2}$$

to the atmosphere in this scenario. Hence, the AHF factor is $\zeta = 0.66$ for solar energy in this scenario

The much smaller AHF contribution of solar PV energy production compared to e.g. fossil fuels in general is to some degree cancelled by the low efficiency of the technology. Note that this factor does not depend on the solar irradiation on the PV. If the solar panels are placed somewhere else with a lower solar irradiation, more area needs to be covered with PV cells, but at the same time the additionally absorbed radiation per m^2 is less. However, in a region with less albedo and, in particular, less surface albedo, the change in planetary albedo $\Delta\alpha_P$ is much smaller. E.g. if one wants to produce all energy with PV cells on the ocean, the surface albedo is barely changed and so the additional AHF vanishes and $\zeta = 0$.

This illustrates that the position of the solar panel and the local climate patterns (like cloud cover, usual surface type, etc.) is crucial for the determination of the AHF contribution of solar power plants.

- There are different approaches to determine how much energy can be extracted from solar radiation: In general the total power arriving at the TOA is $1.7 \cdot 10^5$ TW, i.e. a factor of 10,000 of the current energy production (456 years of 2%-growth). Jacobson and Delucchi (2011) claim a maximum solar PV energy production of 6500 TW in total and 340 TW (i.e. a factor 20 of today's primary energy production or 150 years of 2%-growth) in likely developable locations, e.g. only on suitable land areas and latitudes between $50°S$ and $50°N$. With an AHF factor of mostly less than 0.66, fully exploiting the 340 TW leads to an additional AHF in the same order of magnitude of the tenfold increase described in Chapters 2 to 4. A more applied approach that takes the seasonal, daily fluctuations of wind and solar power and the implications for the grid and storage technology into account for the US is presented in Shaner et al. (2018).

  Again, Kleidon (2012)'s approach can be used to retrieve a limit by calculating the rate of free energy generation. The free energy from solar power is in the same order of magnitude (6070 TW) as Jacobson and Delucchi (2011)'s approach. However, Kleidon states that most of this energy is used to drive dissipative processes in the atmosphere, like the circulation, convection or hydrological cycle and is not available for human appropriation.

  By placing solar cells into space, a basically unlimited amount of solar energy can be achieved. One could investigate the energy needed to transfer the material there and look at options to store energy (and make it return to earth). Such ideas are not pursued further here.

  According to Jacobson and Delucchi (2011) and references therein the extension of PV-solar panels to global dimensions could at most be limited by the availability of silver (for electrodes) and germanium (for multi-junction solar cells). However, there are methods to substitute these materials.

Due to the immense availability of solar power, the growing extraction of this energy potentially poses a threat to the climate via the AHF. However, the AHF contribution from solar power is much lower compared to conservative energy sources, especially if solar panels are placed on dark surfaces.

5.2.5 Wind Power

- Wind power classifies as non-additional heat in the atmosphere. Wind, in general, is driven by local disequilibria of temperature and pressure created by the solar irradiance on the earth[3]. The resulting flows of air (near the surface or in the future perhaps even at the altitude of the jet stream) are used to produce electricity. Without the extraction by wind power plants, the kinetic energy of the wind would nonetheless dissipate as heat through friction (e.g. on mountains or trees) on relatively short timescales. Hence, the AHF contribution is zero.

  However, the extraction of large amounts of wind power changes the redistribution of temperature and, thereby, can indirectly lead to a much larger temperature change (cooling *or* warming), as e.g. discussed in Marvel, Kravitz, and Caldeira (2013).

- Since wind power is not contributing to the AHF, the efficiency is only relevant for the number of power stations but not for the AHF, i.e. $\zeta = 0$. Anyway, the efficiency of wind power extraction is limited to 59.3% by Betz's law, accounting for the fact that air needs to leave the wind power station after the extraction of power in order to sustain the flow.

- The limitation of wind power is subject to a large debate. In the following, some studies about the potential of wind power with strongly deviating results are presented:

  One example for defining a geophysical limit is given in Marvel, Kravitz, and Caldeira (2013). The authors find that the maximum extractable power from wind power plants is 400 TW if placed on the surface, but more than 1800 TW if high-altitude winds are used. In a climate model, a parameter that controls the 'effective extraction area per unit volume' is introduced, which determines the amount of drag force either in near-surface altitudes or uniformly in the whole atmosphere. For small extraction areas the resulting power generated from those wind farms rises linearly with the drag force. After a certain threshold of the extraction area parameter, though, the extracted power saturates. This is defined as the geophysical limit. Next to massive impacts on the circulation (like the poleward heat transport), Marvel, Kravitz, and Caldeira (2013) find a global mean temperature increase (for near-surface wind farms) or decrease (for wind farms utilising the whole height of the atmosphere) arising from this large wind power extraction.

  In fact, there is no consensus as to whether wind energy from the jet stream in high altitudes can significantly contribute to the energy production. According to the more physically and theoretically motivated framework based on the free energy balance developed in (Kleidon, 2012), Miller, Gans, and Kleidon (2011) claim that the maximum extractable power of the jet stream wind is only 7.5 TW, i.e. two orders of magnitude lower. The reason for this much smaller limit according to Miller, Gans, and Kleidon (2011) is that 'the high wind speeds [in the jet stream] result from the near absence of friction and not from a strong power source'. Therefore, the sustainable extraction rate is limited by the 'generation rate of kinetic energy', i.e. the net power inserted in the mean flow, and can not be calculated from the instantaneous wind power via $\frac{1}{2}\rho v^2$. Imagine a flow of air without any forces (and no friction). Then, extracting the energy would stop the flow and the maximum rate of energy extraction would be zero immediately afterwards. Since the jet stream is a geostrophic flow (resulting from a balance of the pressure gradient from equator to pole and the corresponding Coriolis force, not driven by an external force), the generation rate of kinetic energy is considerably low and depends on the depletion rate of the pressure gradient, which shifts the

---

[3] Or by the balance between a pressure gradient and the Coriolis force (geostrophic winds) as described later.

  energy balance away from this purely geostrophic balance. Thus, it cannot provide the society with large amounts of energy according to Kleidon (2012).

  Another estimate in Jacobson and Delucchi (2011) puts a geophysical limit of surface wind (100m above ground) at 1700 TW with roughly $40-85$ TW power in 'likely developable locations', i.e. three to seven times the global energy demand.

  A further restriction on the energy production from wind farms is the extraction rate of raw materials (in particular Neodymium) to produce permanent magnets for the generators. Jacobson and Delucchi (2011) state that the need for Neodymium is 0.2 kg/kWh for current generators. While the global reserves are large enough to support an extensive growth, the extraction rate would need to increase strongly, which yields further political, environmental and economical issues. On the other side, the development of alternative generator designs without Neodymium can eliminate this restriction (Jacobson and Delucchi, 2011).

Since wind power does not contribute to the AHF, only the redistribution of heat through the wind power plants contributes to a climate change.

5.2.6 Hydroelectric Power

- Hydroelectric power is generated by the evaporation and precipitation through solar power, and thus the extraction of kinetic energy from the gravitational potential. For the contribution of hydroelectric power to the AHF, the same argument holds as for wind power: It does not contribute to the AHF. However, the creation of artificial lakes has strong environmental as well as social impacts.
- In principle, the conversion efficiency of kinetic energy into electricity can approach a value close to one. Since the AHF contribution is zero, also $\zeta = 0$ holds.
- According to Jacobson and Delucchi (2011), suitable locations for large-scale hydro power plants are very limited and mostly already in use. Today, 0.32 TW are generated globally by hydro power, making it the largest fraction of the renewable energy sector.

The AHF factor of **tidal**, **wave**, and **ocean circulation** power stations is nearly zero due to similar arguments as presented for hydroelectric and wind power. Their contribution to the primary energy production is relatively small and is not projected to grow in the future.

5.2.7 Biomass

- The burning of biomass is the combustion of recently created plants from solar energy via photochemistry. From the released heat, useful energy like electricity can be produced.

  Strictly speaking, one would also have to include the food production into the human primary energy consumption. If 10 billion people eat roughly 2000 kcal per day, the radiation from the human bodies ($\sim 100\,W$/person) alone is 1 TW (compare to 17 TW primary energy production). In fact, the 'primary energy' needed for this food is much larger because the energy uptake by our bodies as well as the conversion of raw materials to food (e.g. the production of meat via the feeding of cattle) is relatively inefficient (Kleidon, 2012), making this contribution a major factor in the anthropogenic energy demand.

It is difficult to clarify whether biomass contributes to the AHF. One could argue that plants and animals are the result of recent solar energy, and would, if not eaten by humans, still emit their stored energy at some point through natural decay. Similar to the fossil fuels, this is a question of time scales and the ratio of production vs. consumption of plants or animals. However, if e.g. forests are converted into grassland for cattle, the surface albedo is changed and, thus, the anthropogenic heat flux is also influenced. Through a large-scale greening of previously unused land, and thereby an increase of the albedo, the process of biomass burning could even be a negative influence on the AHF.

- The burning of biomass to produce electricity is also limited by the thermal efficiency. Furthermore, the efficiency of plants to produce biomass from solar energy would be relevant for the calculation of the AHF contribution.
- The limitations of biomass include the availability of precipitation, solar radiation, nutrition, space, etc. Hence, defining geophysical limits can be very difficult. One approach to calculate the potential of biomass in the energy mix is given in Ladanai and Vinterbäck (2009), for example. Furthermore, in Kleidon (2012)'s work, biotic activity is one of the biggest sources of free energy with a generation rate of currently 215 TW. In contrast to solar free energy or the contribution from the interior of the planet, a large fraction of this biotic free energy is not dissipated but is the main driver to establish the disequilibrium on earth (Kleidon, 2012).

5.3 Summary

In summary, not all of the primary energy sources contribute to the AHF, as assumed for the modelling Chapters 2 to 4. However, in 2010 the share of purely contributing energy sources, nuclear and fossil fuel energy, was $\sim 87\%$ (IEA, 2014). Including the partially contributing sources, e.g. geothermal, solar and biomass, this number increases even more and the assumption of taking the whole primary energy as a measure for the AHF seems to be justified. Next to the AHF contribution, an approach was made to estimate limitations of the efficiency of producing electrical energy for each source and limits of the availability.

In Figure 5.1, a graph is shown that summarises the thoughts on the contribution of each energy source to the AHF and its efficiency of producing electrical energy presented in the section above. All of these findings are rather qualitative and non-comprehensive first approaches. There are a vast number of additional processes that could be included in this thought experiment. The main purpose of this chapter and the graphic is to establish the framework of the additional heat input into a system and to get a feeling for the contributions and orders of magnitude of the different energy sources.

One key message, though, is that a transition to a renewable energy mix (without nuclear energy) largely eliminates the problem of a global warming through anthropogenic heat emissions.

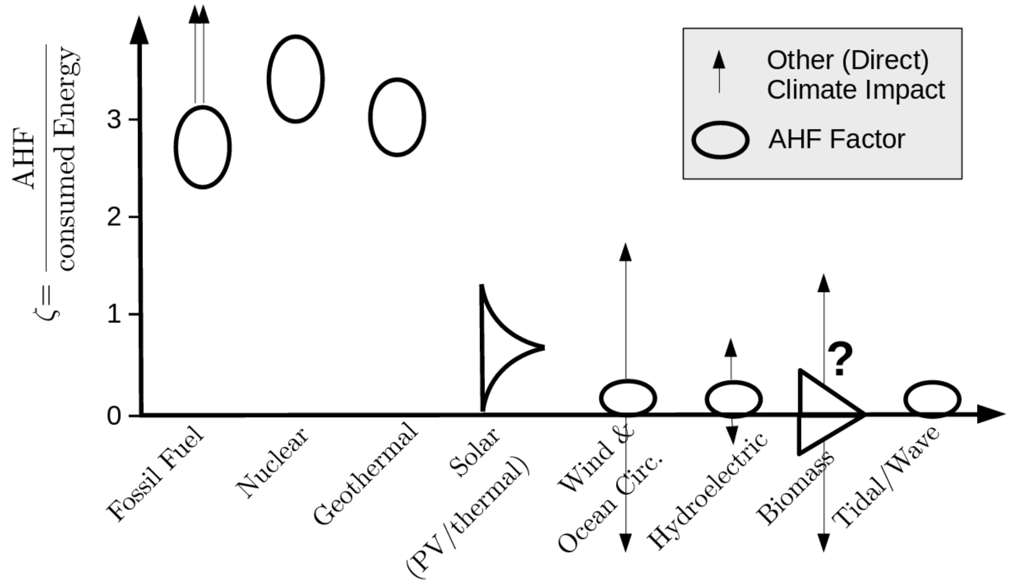

Figure 5.1: Contribution of a certain energy source to the AHF if the raw material is used to produce electrical energy: $\zeta = \frac{\text{AHF [W]}}{E_{\text{consumed electrical energy}}}$ as in equation (5.1).
The energy retrieved from the combustion of fossil fuels, from nuclear fission power plants and from geothermal power fully contributes to the AHF. The efficiency of roughly 33% (or slightly higher) of a heat engine gives a factor of roughly 2-3 in the conversion of primary energy to electricity. For PV and thermal solar cells, the associated change in albedo is the only contribution to the AHF: $\zeta = \frac{\Delta\alpha_P}{\eta}$. Depending on the location and technological specifications the AHF factor can reach from zero to roughly one. Wind, hydroelectric, wave and tidal power do not contribute to the AHF, however, there might be other large climate impacts associated with them (such as a change in global mean temperature due to the reduction of meridional transport and the feedbacks associated with the lower temperature exchange (Marvel, Kravitz, and Caldeira, 2013)). The contribution of biomass to the AHF, e.g. through changes in the surface albedo, has not been adequately determined here.

Chapter 6

Challenging the Assumption of Future Growth Scenarios - Socio-Economic Limits.

Primarily, two potential future primary energy production scenarios are investigated in this thesis: A constant 2% growth of primary energy production per year over the next decades and the more elaborate SSP5-baseline scenario, with a growth rate similar to the 2%-growth scenario until 2050 but a saturation towards the end of the century resulting in roughly half of the primary energy production of the 2%-growth scenario in 2100 (see Figure 4.5). Despite this saturation, the SSP5-baseline scenario is established as the scenario with the highest energy production (Kriegler et al., 2017).

So why is the much more radical scenario of continued exponential growth (with a growth rate of 2% similar to the current value) investigated next to the SSP5-baseline approach?

In fact, the data sets for separate world regions (later in Figure 4.3) indicate that many (especially more developed) regions show a stagnation of the total primary energy production in the recent years, while other regions such as East Asia and parts of Africa grow much stronger than with 2% per year. A saturation, e.g. following a sigmoidal (or logistic) curve, is often used as a typical projection of after a period of accelerated growth (e.g. for the population size in the SSP5). However, some studies (e.g. Peters et al. 2011 or Jakob and Marschinski 2012) also argue that the reason why the energy production in wealthy regions like North America or Europe does not grow at the moment is that energy-intensive industries have been outsourced to developing countries[1].

The following section presents some arguments to justify the assumption of exponential growth of future energy production. Afterwards, a framework from Garrett (2014) is shortly presented that can be used to simulate such scenarios in a model that obeys physical laws rather than one that relies on currently existing economic theories and assumptions.

---

[1] A different method, like using consumption based energy data, would capture these developments better than the approach via the primary energy production in this thesis. However, this neglects other contributions like the AHF created during the process of energy production itself and, therefore, is not pursued in this work.

6.1 Exponential Growth as a Business-As-Usual Scenario?

So far, the data of global primary energy production has not shown any sign of saturation[2]. In fact, the primary energy supply per capita shows a small increasing trend over the last decades(IEA, 2014).

Furthermore, imagine the whole world were powered by 'clean' energy sources (e.g. fusion power plants), eliminating the problem of greenhouse gas emissions and, hence, one big incentive to reduce the energy consumption. In such a scenario, there would be no obvious reason why the thrive for growth in our civilisation should stop.

A very simple, first-guess business-as-usual approach should, consequently, not exclude the possibility of truly maintaining a constant growth rate (at least for a few generations).

Of course, there are several arguments why the saturation in the SSP5 scenario makes sense: For instance, the growth in population is somewhat limited by the amount of food or space available on the planet. Also, one might think that a person's energy demand needs to saturate at some point (you can only fly, drive or consume energy a fixed number of hours per day).

However, one could argue that we simply cannot forecast what life in a society in 30, 50 or 116 years looks like. As the development of the energy demand from e.g. bitcoin mining proves, there might be big technological innovations far beyond our imagination that require vast amounts of energy. The energy demand for bitcoin mining is already of the order of the electricity consumption of Austria (Digiconomist, 2018) – an increase in energy demand that was completely unforeseeable only a decade ago. Similar arguments might also apply for the restriction of the population size: Research on genetically manipulated food or cloning exists already. Thus, our estimates on the carrying capacity of the planet (sustainable or not) could be strongly underestimated due to unknown technological innovation and biological evolution (Arrow et al., 1996).

Finally, even if both the population size and the energy demand per capita saturate in the second half of the century or even before, a continued 2% growth of the energy production over several decades is not entirely far-fetched: As shown in Figure 1.1, providing each inhabitant on this future world (assume 10 billion people) with an equal amount of available primary energy, say that of the average American citizen[3] a fivefold increase of the global primary energy production is required (or a 2% increase over 81 years), which goes far beyond the saturated energy demand of the SSP5-baseline scenario.

Of course this assumption of a continued exponential growth implies many radical consequences about the way of living and the rate of innovation. The approach should be seen as a reasonable, but extreme upper limit that is more risk-averse than standard methods like the SSP scenarios.

As a side note, in the previously mentioned study on the AHF by Flanner (2009) the energy projection between 2040 and 2100 also follows a 2% growth per year.

---

[2] Note that the current growth rate is actually slightly smaller than in the 1970s or 1980s in the data provided by IEA (2014). However, this is presumably (mostly) due to economic fluctuations and changes in the methods of the data acquisition by the IEA, e.g. the growth rate in the last decade since the economic crisis is much larger than in the data for the 1990s.

[3] Who has a relatively large energy demand, but by far not the largest.

6.2 A Theoretical Framework to Determine Possible Future Primary Energy Production.

Scenarios like the SSP framework often base on micro-modelling of relevant agents, like governments or economic global players in the context of our socio-economic system. A more theoretical, macro-model to calculate restrictions on the future energy demand by Garrett (2014) is presented in the following.

In contrast to complicated and multi-dimensional Integrated Assessment Models, this framework describes a low-dimensional, global approach to forecast the society's economic growth and greenhouse gas emissions based on physical laws rather than economic descriptions. This has the advantage that the model does not extrapolate the current economic structure and socio-economic rules to future societies.

Garrett represents the civilisation as a uniform, open, non-equilibrium, thermodynamic system (without any resolved internal differences). This civilisation consumes and dissipates energy in order to sustain existing circulations and further material growth.

The global wealth, i.e. in Garrett's terms the integrated global economic production over the past, is supported through the primary energy production. These two variables are tied to each other over a constant retrieved from data: $7.1\,W$ primary energy production is required to sustain 1000 (inflation adjusted) 2005 US-dollar (Garrett, 2012). Hence, growth in energy production implies growth in wealth.

This system can be described by a thermodynamic formulation, which leads to a deterministic equation for the so-called 'rate of return'. The evolution of this rate of return determines the growth rate of the energy production (and civilisation's wealth). Prior growth, for example, leads to the ability of a system to continue or even accelerate its rate of growth, i.e. there is a positive feedback loop. In analogy, a child that eats and, thereby, grows, requires more food or energy later on in order to sustain its internal processes. On the other hand, external decay (e.g. through environmental damages) decreases the rate of return and, hence, leads to a decrease in production.

The evolution of the rate of return is determined by

- the rate of energy reserve discovery (i.e. if energy reserve discovery exceeds the depletion rate, the growth is accelerated),
- the increased longevity of the drivers of our civilisation (e.g. a longer average lifetime of people leads to faster growth; however, increased decay due to e.g. natural disasters hampers growth),
- the change in efficiency of turning raw materials or energy into 'useful' things or infrastructure (if the energy and materials required to build a road towards new energy resources, the energy extraction and, hence, the economic wealth grows) and
- a saturation from prior growth (the law of diminishing returns).

Especially the third factor, i.e. changes in the efficiency of raw material extraction, highlights a crucial finding of the work that is often not considered in standard economic models: The rebound effect. Efficiency improvements lead to cheaper energy, which in turn increase the energy consumption, rather than decrease it.

The framework leads to a certain number of distinct growth modes for the primary energy consumption and the economic wealth, depending on the rate of technological innovations and the initial growth rate. Another key finding is that, when growth rates approach zero, these modes become instable, i.e. the economy and energy production can likely be locked in a state of accelerated collapse. This is especially true for systems that have initially grown super-exponentially (similar to a bubble economy).

Such models, as the one described in Garrett (2014), can help to set limits for future energy scenarios and consider more radical scenarios like super-exponential growth cases, which obey physical laws, rather than human-made economic theories. Also, they give an idea about possible equilibrium states of economy and energy production and their implications (such as the instable regime for zero growth models).

On the other hand, such models do not include any human decision making or any form of political or economic action by the society, which makes the theory in Garrett (2014) a rather untypical approach. E.g. Müller-Hansen et al. (2017) reviews some modelling techniques that model the complex interrelationships between agents and socio-economic processes and corresponding emergent behaviour on a macro-level.

6.2.1 Summary

The assumption of a 2% growth per year of the AHF is a risk-averse, upper-limit scenario that is certainly more radical than usual projections. However, there are several logical as well as theoretically based arguments for such a continued growth case.

Next to the evolution of the total primary energy, both the energy mix as well as the efficiency play an important role in the future dynamics of the AHF as discussed in Chapter 5. While a shift towards a renewable energy mix eliminates most warming from anthropogenic emissions, an extensive use of nuclear power (e.g. through fusion power) increases the AHF.

One important aspect of this framework described in this chapter is that efficiency gains (e.g. on the demand side), while leading to a decrease in primary energy consumption (and, hence, AHF) in first order, might on the contrary fuel energy use in total through the rebound effect (Garrett, 2014). This stresses the relevance of studying the impacts of increasing AHF on the climate.

Chapter 7

Conclusion

Key Findings and Summary. This thesis has explored the climate impacts of future growth scenarios for an additional forcing from the anthropogenic heat flux in simple to intermediate complexity climate models.

In the first step, in Chapter 2, the forcing was included in a conceptual and simple zero-dimensional Energy Balance Model. Today, the AHF of $0.034\,\mathrm{W/m^2}$ adds $0.010\,\mathrm{K}$ to the total anthropogenic warming in this model. This number provides a valuable and easily reproducible order of magnitude estimate of the impact due to the AHF. The Energy Balance Model was then extended to a latitude-dependent EBM-1D in Chapter 3. This made the parametrisation of ice possible. Hence, the ice-albedo feedback due to the AHF forcing was calculated as a major feedback impact. The EBM-1D has various degrees of freedom and most models in this framework are relatively instable w.r.t. being converted to a houthouse planet. In particular, this is determined by the choice of parametrisation for certain processes as well as the meridional transport strength. Therefore, the temperature increase depends strongly on the model configuration and the corresponding shift of the iceline due to the additional AHF forcing. In general, the ice-albedo feedback in reasonable configurations is in the same order of magnitude as the direct AHF forcing, resulting in a strong Arctic amplification of the temperature increase.

In Chapter 4, a more complex, comprehensive climate model, CLIMBER-3α, was used to obtain more realistic impact estimates of the AHF forcing. The AHF was inserted as a locally confined 2D forcing distribution at the surface of the atmosphere. Similar to the EBM-1D, the direct forcing and the ice-albedo feedback originating from the sea ice retreat are in the same order of magnitude. Additionally, a third relevant impact is obtained, the increase of the ocean heat uptake, which acts as a negative (transient) forcing. The direct and indirect impacts of the AHF also further influence the ocean circulations, e.g. the AMOC and the subpolar gyre. Through a complex interaction of these circulations with each other and the sea ice, even the relatively small heterogeneous forcing impact of the past decades can give rise to strong fluctuations in the local temperature in the Arctic region. Furthermore, the influence of the location of the AHF emission on the impact was extensively discussed: In a nutshell, the size and pattern of the impact depend for example on the latitude, the parameters of the surrounding cells (like land fraction) and certain ocean circulation features (e.g. the strength of the ocean heat uptake).

In order to compare the models, the temperature responses to a potential future tenfold increase of the current AHF (i.e. a continued exponential growth over slightly more than the next century) were simulated. The numbers are summarised in Table 7.1.

Model		$\overline{\Delta T}$ [K]	Southern Iceline in °	Northern Iceline in °
EBM-0D		0.092	NA	NA
EBM-1D	Smaller D ($\mathrm{BsD}_{-10}(\mathrm{G_F})$)	0.096	$-65.5 \rightarrow -65.5$	$65.5 \rightarrow 65.5$
CLIMBER	Transient (2%-growth per year)	0.127		
CLIMBER	Equilibrium	0.157		
EBM-1D	Larger D ($\mathrm{BD}_{-10}(\mathrm{G_F})$)	0.219	$-70.5 \rightarrow -70.5$	$70.5 \rightarrow 72.5$

Table 7.1: Summary of the (temperature) results from all different models obtained for a tenfold increase of today‘s AHF forcing.

In Chapter 5, the previous assumption that all energy contributes to the AHF forcing irrespective of the energy source is dropped and the AHF contribution of each energy source is determined, individually. Furthermore, the maximum amount of available energy from the specific source is estimated.

Finally, in Chapter 6, the assumption of a continued growth in energy production (and economic production) over the next century is critically discussed and justified for the purpose of this thesis.

Motivation and Political Implications for Future Energy Scenarios. Nearly all current large-scale economic systems thrive for continued growth. Through the past decades of growth, the human civilisation has already severely altered the living conditions on this planet. At the moment, the main anthropogenic impact on the planet is the emission of greenhouse gases (IPCC, 2013). However, amplified through the Paris Agreement in 2015, both the policy makers' as well as the public opinion increasingly shifts towards trying to reduce greenhouse gases and to abolish emissions overall.

One hope to achieve these goals is to use controlled nuclear fusion to produce electricity. Setting aside the problem that no fusion power plant has produced a net energy outcome so far, fusion power provides basically unlimited and 'clean' energy[1]. However, similar to fossil fuels or nuclear fission, this adds additional heat into the atmosphere, with the consequences described in this work.

So far, the AHF has no relevant climate impact on a global scale. However, given continued growth in a decarbonised world, the AHF can become a relevant factor of post-greenhouse gas warming in the relatively near future within the next century. Also, on a local scale, even today the AHF is a non-negligible process. This holds not only for the direct AHF impact in urbanised areas, but also for remote, large-scale areas like the sea ice near Greenland due to the ice-albedo feedback and impacts on the ocean circulation. The analysis of CLIMBER-3α has shown that a forcing as small as the AHF in the current years (roughly 2% of the CO_2 forcing) can influence ocean circulation in such a way that a temperature change of more than $\pm 0.3\,\mathrm{K}$ can result in the Arctic region with significant changes in the sea ice cover.

Future research on this subject could reproduce these simulations with different, more elaborate scenarios and other models in order to obtain consensual statements, include more processes and more accurate parametrisations of these processes. Also, while keeping the global perspective and the long time horizon with significantly deviating energy production rates compared to those nowadays, a higher resolved model could give more insights. These include especially the impacts in Greenland or Spitzbergen, for example, and a possible earlier collapse of tipping elements, e.g. the AMOC or the Arctic (summer) sea ice.

Concluding, the forcing introduced through the anthropogenic heat flux is by no means a dominant contribution to the global warming today. If radical energy projections are used for the next century, however, it can become an important factor for post-greenhouse gas warming. Some energy sources, like

---

[1] Further (more radical) thought experiments on extending the 'sustainable' energy reserves of our society in a growth-driven world include the appropriation of the wind power in the jet stream or solar panels in space.

wind power, are advantageous in this process, since they do not insert (as much) additional heat as, for example, fusion. However, while ‘green growth’ approaches may certainly help to bring forward the decarbonisation of the energy sector, ultimately, the growth in energy production will have to stop before the human civilisation overheats the planet through anthropogenic heat emissions. Such a limit is still at least a few generations away, also depending on the availability of renewable energy sources, but might be approached in the next century.

Appendix

A.1 How to Insert the AHF

In all models of this thesis, i.e. the EBM-0D, EBM-1D, as well as in CLIMBER-3α the AHF is inserted as a direct (ground) heat flux input. As Zhang, Cai, and Hu (2013) point out there are other ways to do this. In a multi-layer atmosphere model, P_{hum} could also be inserted either as a sensible heat flux or as long wave (LW) radiation. Ground heat flux directly increases the temperature of the surface and, thereby, increases the sensible heat flux and the OLR.

If P_{hum} is directly interpreted as an increase of LW radiation from the surface, most of the energy would be trapped in the lower troposphere, where LW radiation is absorbed, and heats the atmosphere layers there. In this case, the temperature impact of the AHF would change due to the absorption and reflection in the atmosphere. E.g. equation (2.10) in the simple EBM-0D would read $\sigma\overline{T_S + \Delta T_S}^4 = \sigma\overline{T_S}^4 + \overline{P_{\text{hum}}}$ instead of $\sigma\overline{T_S + \Delta T_S}^4 = \sigma\overline{T_S}^4 + \overline{\frac{P_{\text{hum}}}{\tau}}$ and would, thereby, enhance the temperature impact of the AHF.

Similarly, if directly interpreted as sensible heat flux, the AHF warms the atmosphere layers in the lower troposphere. Zhang, Cai, and Hu (2013) chose to model the AHF as sensible heat flux in their work.

A.2 Amplification of the Temperature Increase in EBM-0D due to Simultaneous $\mathbf{CO_2}$ and $\mathbf{P_{hum}}$ Increase

The basic equation of the zero-dimensional EBM with a linear OLR parametrisation is given in equation (2.11) and reads:

$$0 = \frac{S_0}{4}(1-\alpha) - (A + B \cdot T) + P_{\text{hum}} \ . \tag{7.1}$$

Here, the parametrisation of the parameters A and B according to Caldeira and Kasting (1992) is used to model a CO_2-dependency. With this, the additional amplification of the temperature increase in the scenario, in which CO_2 and P_{hum} are increased simultaneously, is analytically derived in the EBM-0D, i.e.:

$$\Delta T_{\text{combined}} > \Delta T_{\text{P}} + \Delta T_{CO_2} \ , \tag{7.2}$$

where $\Delta T_{\text{combined}}$ is the temperature change, when both P_{hum} and CO_2 are increased simultaneously.

Note, in Caldeira and Kasting (1992) A and B are in fact $A, B\,(CO_2) = A, B\,(\ln(CO_2))$. From equation (7.1) the temperature in this model is given by:

$$T_S(CO_2, P_{\text{hum}}) = \frac{S_0/4(1-\alpha) + P_{\text{hum}} - A(CO_2)}{B(CO_2)} \tag{7.3}$$

First, the temperature increases due to separate P_{hum} (ΔT_P) and CO_2 increases (ΔT_{CO_2}) are :

$$\begin{aligned} T_S(\text{CO}_2, P_{\text{hum}} + \delta P) &= \frac{S_0/4(1-\alpha) + P_{\text{hum}} - A(\text{CO}_2)}{B(\text{CO}_2)} + \frac{\delta P}{B(\text{CO}_2)} && (7.4) \\ &= T_S(\text{CO}_2, P_{\text{hum}}) + \frac{\delta P}{B(\text{CO}_2)} && (7.5) \\ \rightarrow \Delta T_P &= \frac{\delta P}{B(\text{CO}_2)} && (7.6) \\ T_S(\text{CO}_2 + \delta\text{CO}_2, P_{\text{hum}}) &= \frac{S_0/4(1-\alpha) + P_{\text{hum}} - A(\text{CO}_2 + \delta\text{CO}_2)}{B(\text{CO}_2 + \delta\text{CO}_2)} && (7.7) \\ \rightarrow \Delta T_{\text{CO}_2} &= T_S(\text{CO}_2 + \delta\text{CO}_2, P_{\text{hum}}) - T_S(\text{CO}_2, P_{\text{hum}}) && (7.8) \end{aligned}$$

Next, the simultaneous increases gives the temperature:

$$\begin{aligned} T_S(\text{CO}_2 + \delta\text{CO}_2, P_{\text{hum}} + \delta P) &= \tfrac{S_0/4(1-\alpha) + P_{\text{hum}} - A(\text{CO}_2 + \delta\text{CO}_2)}{B(\text{CO}_2 + \delta\text{CO}_2)} && + \frac{\delta P}{B(\text{CO}_2 + \delta\text{CO}_2)} && (7.9) \\ &= T(\text{CO}_2 + \delta\text{CO}_2, P_{\text{hum}}) && + \frac{\delta P}{B(\text{CO}_2 + \delta\text{CO}_2)} && (7.10) \\ &= T(\text{CO}_2, P_{\text{hum}}) + \Delta T_{\text{CO}_2} && + \frac{\delta P}{B(\text{CO}_2 + \delta\text{CO}_2)} \\ & && + \Delta T_P - \frac{\delta P}{B(\text{CO}_2)}, && (7.11) \end{aligned}$$

where in the last step the previous relations (7.6) and (7.8) are inserted in order to compare the resulting temperature increases from simultaneous to separate increases of P_{hum} and CO_2. Subtracting $T(\text{CO}_2, P_{\text{hum}})$ from equation (7.11) yields:

$$\Delta T_{\text{combined}} = \Delta T_{\text{CO}_2} + \Delta T_P + \frac{\delta P}{B(\text{CO}_2 + \delta\text{CO}_2)} - \frac{\delta P}{B(\text{CO}_2)} \tag{7.12}$$

Then, the amplification of the warming from an additional δP_{hum} due to a simultaneous CO_2 increase in the EBM-0D is:

$$\frac{\delta P}{B(\text{CO}_2 + \delta\text{CO}_2)} - \frac{\delta P}{B(\text{CO}_2)}, \tag{7.13}$$

which is always positive, since the slope of the OLR parametrisation of time decreases with CO_2: $B(\text{CO}_2) > B(\text{CO}_2 + \delta\text{CO}_2)$. Furthermore, since the decrease in $B(\text{CO}_2)$ with CO_2 flattens for high CO_2 values (i.e. $B(\text{CO}_2 + \delta\text{CO}_2) \rightarrow B(\text{CO}_2)$ for $\text{CO}_2 \rightarrow \infty$), the amplification slowly vanishes for large CO_2 concentrations.

The main message of this derivation is that the temperature changes from an increase of CO_2 and P_{hum} can not be simply added to get the combined temperature increase. This amplification effect can be calculated analytically for the linear OLR parametrisation of Caldeira and Kasting (1992).

A.3 Results of the EBM-1D Including the Ice-albedo Feedback for a Tenfold Increase of $\mathbf{P_{hum}}$

Model Configuration	$\langle\mathbf{\Delta T}\rangle_\theta$	**initial → final iceline [south, north]**
$(\mathrm{LMD}_{-2}(\mathrm{M}))$	$\mathbf{1.920}\,^\circ\mathrm{C}$	$[-69.5, 69.5] \rightarrow [-89.5, 89.5]$
$(\mathrm{LMD}_{-2}(\mathrm{G_F}))$	$\mathbf{1.838}\,^\circ\mathrm{C}$	$[-69.5, 70.5] \rightarrow [-89.5, 89.5]$
$(\mathrm{LMD}_{-10}(\mathrm{M}))$	$\mathbf{0.461}\,^\circ\mathrm{C}$	$[-70.5, 70.5] \rightarrow [-72.5, 72.5]$
$(\mathrm{LMD}_{-10}(\mathrm{G_F}))$	$\mathbf{0.374}\,^\circ\mathrm{C}$	$[-70.5, 70.5] \rightarrow [-70.5, 73.5]$
$(\mathrm{LMsD}_{-2}(\mathrm{M}))$	$\mathbf{2.732}\,^\circ\mathrm{C}$	$[-65.5, 65.5] \rightarrow [-89.5, 89.5]$
$(\mathrm{LMsD}_{-2}(\mathrm{G_F}))$	$\mathbf{2.706}\,^\circ\mathrm{C}$	$[-65.5, 65.5] \rightarrow [-89.5, 89.5]$
$(\mathrm{LMsD}_{-10}(\mathrm{M}))$	$\mathbf{0.361}\,^\circ\mathrm{C}$	$[-65.5, 65.5] \rightarrow [-66.5, 66.5]$
$(\mathrm{LMsD}_{-10}(\mathrm{G_F}))$	$\mathbf{0.251}\,^\circ\mathrm{C}$	$[-65.5, 65.5] \rightarrow [-65.5, 66.5]$
$(\mathrm{LCD}_{-2}(\mathrm{M}))$	$\mathbf{2.065}\,^\circ\mathrm{C}$	$[-70.5, 70.5] \rightarrow [-89.5, 89.5]$
$(\mathrm{LCD}_{-2}(\mathrm{G_F}))$	$\mathbf{2.090}\,^\circ\mathrm{C}$	$[-70.5, 70.5] \rightarrow [-89.5, 89.5]$
$(\mathrm{LCD}_{-10}(\mathrm{M}))$	$\mathbf{0.678}\,^\circ\mathrm{C}$	$[-70.5, 70.5] \rightarrow [-73.5, 73.5]$
$(\mathrm{LCD}_{-10}(\mathrm{G_F}))$	$\mathbf{1.147}\,^\circ\mathrm{C}$	$[-70.5, 70.5] \rightarrow [-71.5, 89.5]$
$(\mathrm{LCsD}_{-2}(\mathrm{M}))$	$\mathbf{3.058}\,^\circ\mathrm{C}$	$[-65.5, 65.5] \rightarrow [-89.5, 89.5]$
$(\mathrm{LCsD}_{-2}(\mathrm{G_F}))$	$\mathbf{2.994}\,^\circ\mathrm{C}$	$[-65.5, 66.5] \rightarrow [-89.5, 89.5]$
$(\mathrm{LCsD}_{-10}(\mathrm{M}))$	$\mathbf{0.404}\,^\circ\mathrm{C}$	$[-65.5, 65.5] \rightarrow [-66.5, 66.5]$
$(\mathrm{LCsD}_{-10}(\mathrm{G_F}))$	$\mathbf{0.397}\,^\circ\mathrm{C}$	$[-65.5, 65.5] \rightarrow [-65.5, 67.5]$
$(\mathrm{BD}_{-2}(\mathrm{M}))$	$\mathbf{1.230}\,^\circ\mathrm{C}$	$[-70.5, 70.5] \rightarrow [-89.5, 89.5]$
$(\mathrm{BD}_{-2}(\mathrm{G_F}))$	$\mathbf{0.721}\,^\circ\mathrm{C}$	$[-70.5, 70.5] \rightarrow [-71.5, 89.5]$
$(\mathrm{BD}_{-10}(\mathrm{M}))$	$\mathbf{0.222}\,^\circ\mathrm{C}$	$[-70.5, 70.5] \rightarrow [-71.5, 71.5]$
$(\mathrm{BD}_{-10}(\mathrm{G_F}))$	$\mathbf{0.219}\,^\circ\mathrm{C}$	$[-70.5, 70.5] \rightarrow [-70.5, 72.5]$
$(\mathrm{BsD}_{-2}(\mathrm{M}))$	$\mathbf{0.252}\,^\circ\mathrm{C}$	$[-65.5, 65.5] \rightarrow [-66.5, 66.5]$
$(\mathrm{BsD}_{-2}(\mathrm{G_F}))$	$\mathbf{0.248}\,^\circ\mathrm{C}$	$[-65.5, 65.5] \rightarrow [-65.5, 67.5]$
$(\mathrm{BsD}_{-10}(\mathrm{M}))$	$\mathbf{0.096}\,^\circ\mathrm{C}$	$[-65.5, 65.5] \rightarrow [-65.5, 65.5]$
$(\mathrm{BsD}_{-10}(\mathrm{G_F}))$	$\mathbf{0.096}\,^\circ\mathrm{C}$	$[-65.5, 65.5] \rightarrow [-65.5, 65.5]$

Table 7.2: Changes in equilibrium global mean temperature and northern and southern iceline for different model configurations as described in Table 3.1. The OLR can be either parametrised as a Boltzmann **(B..)** process (as in equation (2.5) or linearly approximated according to Mcguffie and Henderson-Sellers (2014) **(LM..)** or Caldeira and Kasting (1992) **(LC..)** as in equation (2.6)). The meridional transport constant is tuned to iceline = 70° **(..D..)** or (in order to stabilise the system) iceline = 65° **(..sD..)**. The freezing temperature, at which the albedo switches from 0.3 to 0.6 is −2°C $(.._{-2}..)$ or −10°C $(.._{-10}..)$. And, finally, the AHF is either inserted as a global mean **(M)** or a Gaussian distribution in the Northern Hemisphere $(\mathbf{G_F})$. In all runs: $\langle P_{\text{hum, final}}\rangle_\theta = 0.34\,\frac{\mathrm{W}}{\mathrm{m}^2}$ and $\langle P_{\text{hum, initial}}\rangle_\theta = 0.034\,\frac{\mathrm{W}}{\mathrm{m}^2}$.

A.4 Data Preparation for Forcings in CLIMBER-3α

Past The Paleoclimate Modelling Intercomparison Project Phase 3 (PMIP3, `https://pmip3.lsce.ipsl.fr/`) provides a recommended set of forcing data sources ready to use for last millennium simulations (Schmidt et al., 2012). The only relevant forcing contributions in the presented CLIMBER-3α runs are from CO_2-equivalent concentration and the solar irradiance. The choice for data sets of these inputs in this thesis is equivalent to the simulations in Feulner (2011) (with the solar radiation reconstruction from Steinhilber, Beer, and Fröhlich (2009)), which also bases on the PMIP3 recommendations.

Some specific derivations for the forcing data are described below:

- Global **GHG concentrations**, which are retrieved from the PMIP3-recommendations in Schmidt et al. (2012): The basic idea of the calculation of the radiative forcing of greenhouse gases is sketched below. The concentrations of the absorptive gases CO_2, N_2O, and CH_4 are considered. At first, the radiative forcing due to relative changes in the concentration of each gas is calculated individually via established formula from Houghton, Jenkins, and Ephraums (1990) or Myhre et al. (1998). For example, for the CO_2 greenhouse effect the radiative forcing is

  $$RF_{\mathrm{CO_2}} = 6.3 \cdot \log(\mathrm{CO_2}/\mathrm{CO_{2,\ ref}}) \ . \tag{7.14}$$

  The equations for N_2O and CH_4 are more complicated. Secondly, all three forcings are added and via the inverse formula transformed into CO_2-equivalent concentrations:

  $$\mathrm{GHG-concentration\,[ppm]} = \mathrm{CO_{2,\ ref}} \cdot e^{\frac{1}{6.3}\cdot(RF_{\mathrm{CO_2}}+RF_{\mathrm{CH_4}}+RF_{\mathrm{N_2O}})} \tag{7.15}$$

- The forcing from **total solar irradiation** is mainly determined by four different factors:
  - The (global mean) solar irradiation at the TOA fluctuates according to orbital variations and periodic changes in the sun. The commonly known 11-year solar cycle is one example, in which the solar constant at the TOA fluctuates by roughly $0.05\,\mathrm{W/m^2}$. Other influences like orbital variations or cosmic rays do not play a substantial role on the time-scales in this thesis.
  - Land-use changes affect the ground and vegetation patterns and, therefore, the surface albedo. Subsequently, the albedo change implies a radiative forcing. This effect amounts to a net radiative forcing of $-0.15\,\mathrm{W/m^2}$ for today's land-use in comparison with pre-industrial times (IPCC, 2013).
  - The emission of anthropogenic sulphates SO_2 (e.g. from ships) and the consequent building of SO_4 aerosols in the atmosphere reflects solar radiation back to space, i.e. these aerosols increase the planetary albedo. This effect has become especially important in the last century, in which aerosol emissions due to enhanced human activity have grown to a crucial negative forcing. E.g. the forcing from sulphate aerosols given in IPCC (2013) is roughly $-0.5\,\mathrm{W/m^2}$.
  - During eruptions of volcanoes large amounts of sulphate are emitted and, therefore, these events can strongly influence the planetary albedo. Historic data for the injection of volcanic sulphate into the atmosphere is retrieved from Crowley (2000) and transformed into radiative forcing.

  Due to these variables, the total solar irradiance usually fluctuates by no more than a few $\mathrm{W/m^2}$ around the mean $S_0 \approx 1361\,\mathrm{W/m^2}$ (Kopp and Lean, 2011). The final data is obtained from Steinhilber, Beer, and Fröhlich (2009), resembling the study in Feulner (2011). The input file containing the yearly total solar irradiance and CO_2-data can be found in folder co2_Constfuture.dat. This data is used up to the year 2010.

Future For future projections of the total solar irradiance, the recommended data set in the CMIP6 recommendation for solar forcing from Matthes et al. (2017) is used. The solar constant in this data set varies mostly only according to the 11-year solar cycle. Volcanic eruptions are switched off and land-use and aerosol concentration are kept constant. The data can be downloaded from the original publication or from solarv_fut2.dat. Even though the recommended data set for future solar forcing starts earlier for the calibration of the CMIP6 models, this new data is used only after 2010.

In order to study the impact of a sole AHF increase, the CO_2-concentration is kept constant in future projections at the 2010 value (387.5 ppm). In the last paragraph of the analysis of CLIMBER-3α (Section 4.4.8), though, the simultaneous increase of CO_2 and AHF is investigated. Then, the SSP5-baseline scenario from (Kriegler et al., 2017), which resembles a business-as-usual case, is used (co2_ssp5.dat). This scenario reaches a CO_2-concentration of 1000 ppm by the year 2094. The growth rate of the CO_2 concentration in the SSP5-baseline scenario rises constantly from $\sim$ 2 ppm/year to $\sim$ 12 ppm/year until it levels off after the year 2080. Note, due to small differences in the absolute CO_2-concentration between the historic and the future (SSP5) data sets, the future projections are patched onto the historic data. From the historic and projected data given in Schmidt et al. (2012) and Matthes et al. (2017) one can reproduce the GHG forcing data used in this thesis with the code in create_co2file_future.py.

A.5 Patching the SSP Data to the World Bank and IEA Data

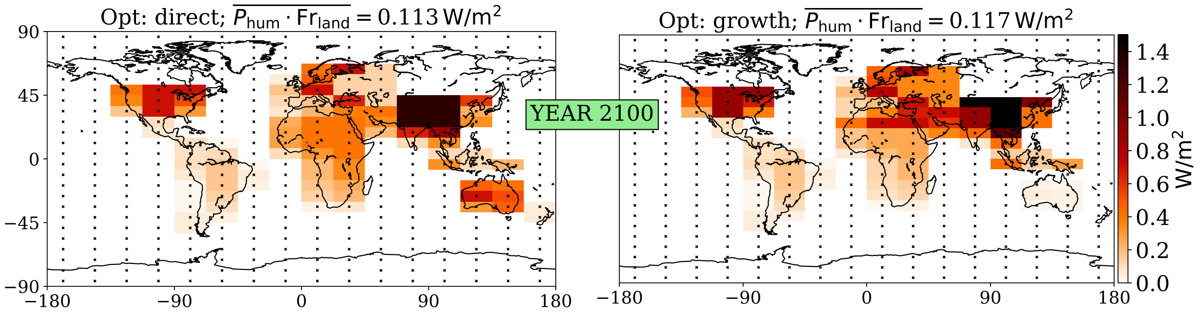

Figure 7.1: Comparison of the two methods to patch the AHF of the $\widetilde{\mathrm{SSP5}}$-baseline scenario from Kriegler et al. (2017) to the historic data from The World Bank (2018) and IEA (2014). The method 'growth' (right) e.g. produces a much larger forcing in the region 'ref' (i.e. around Russia) than the method 'direct' (left), whereas for Australia it is the other way around. The global mean P_{hum} input is slightly larger for the 'growth' method. This can be reproduced by switching between the options *opt* = 1('growth') and *opt* = 2('direct') in the code in create_SSP5baseline_Phum_files.py and comparing the resulting files.

A.6 New Subroutines in Climber

In the file 'exp.F' of the POTSDAM2 code:

```
            SUBROUTINE read_P_hum
**** ***********************************************************
*     This routine is called in  'ini.F'  in subroutine 'setatm'/'INI_CLIMBER':
*         [...] if (KSOLC.eq.1) call DATA_SOL
*         call a_read_P_hum
*         open (77,file='masbal.dat') [...]
*     For each year, read the 'P_hum_yearXXX.dat' files, which are stored in
*    working_dir_p/$run_name/tm ($runname is e.g.  'c3beta_anthrHeat_FULL').
*     Save all P_hum data in a 3D-array
*     ATTENTION: You need to set the times in the initialisation of 'PHUM_all'
*    and in variables 'startyear' and 'endyear', as well as in subroutine
*   'GET_CURRENT_PHUM'
```

```
*     by Peter Steiglechner, April 2018
*****************************************************
    integer :: startyear, endyear
    real, dimension (1:16, 1:24) :: PHUM
    integer :: year
    real, dimension (1810:2010, 1:16, 1:24) :: PHUM_all
    COMMON  /Phum/ PHUM_all
*********************************************************************
    CHARACTER*20 :: file_name_pre, file_name_post, file_name
    startyear=1810
    endyear=2010
    file_name_pre = "P_hum_year"
    file_name_post = ".dat"
    do 10 year = startyear, endyear, 1
        write(file_name, "(A10,I4,A4)") file_name_pre, year, file_name_post
        open (1,file=file_name)
        read (1,*) PHUM
        PHUM_all(year, :, :) = PHUM
        close (1)
    10    continue
    return
    end

****************************************************************************
SUBROUTINE GET_CURRENT_PHUM
****************************************************************************
*     This routine is called in 'potsdam2.F' in subroutine 'POTSDAM2':
*        C... MODULES CALL
*        [...] call get_tbc
*          call  GET_CURRENT_PHUM
*        call PCO2 [...]
*     Here, the P_hum for the current year ('NYR') is loaded into the
*    field 'P_hum' for later use in 'svat.F'.
*     by Peter Steiglechner, April 2018
***************************************************************************
#     include  "declar.inc"
#     include  "params.inc"
real, dimension (1:16, 1:24) :: P_hum
    COMMON /Phum/ PHUM_all(1810:2010, 1:16, 1:24)
    COMMON /current_P/ P_hum
****************************************************************************
    if ((NYR-52973).le.1810) then
        P_hum = PHUM_all(1810, :, :)*0
    else
        if ((NYR-52973).le.2010) then
```

```
        P_hum = PHUM_all(NYR-52973, :,: )
    else
        P_hum = PHUM_all(2010, :, :)*1.02**(NYR-52973-2010)
    endif
endif
return
end
```

A.7 Description of the framework in Kleidon (2012)

In a nutshell, Kleidon derives limits of free energy via the fundamental energy and entropy balance for an open, non-equilibrium system like the Earth System.

For example, the differential heating from the sun leads to a constant disequilibrium of the Earth System in steady state. This disequilibrium is associated with free energy generation. From the temperature gradients across the latitudes, some energy can be extracted to a different gradient, e.g. the movement of air masses, and then further converted to e.g. electricity (electric gradient) in a heat engine.

The entropy balance, however, puts an upper limit on the extraction of power based on the second law of thermodynamics and the competing other process of the dissipation of the gradient – the Maximum Power Principle. In fact, the Earth System operates close to this limit, according to (Kleidon, 2012)[2].

The following analogy illustrates the limit imposed by the Maximum Power Principle: Imagine a temperature gradient that is compensated by a convective heat flux, a.k.a. wind, with a certain amount of power. As it blows along the surface, the wind lifts and accelerates dust particles from the surface. Thus, work can be extracted from the accelerated particles. By moving more particles, the extracted power (here the kinetic energy of the particles) from the temperature gradient increases. However, at the same time the wind looses power as its (kinetic) gradient is depleted by the movement of the heavier particles. There is a trade-off between the force that drives the flux (the momentum gradient) and the flux of particles that depletes this force (the convective heat flux). The energy of the wind can not be fully extracted to move the dust particles.

Using this framework, Kleidon (2012) derives the amount of available free energy generation from the main drivers of the disequilibrium: the radiative energy flux by the sun (i.e. atmospheric circulation, photosynthesis, ...) and the energy fluxes from the 'initial conditions' (cooling of the interior, radioactive decay and crystallisation of the Earth core).

The total free energy generation according to Kleidon (2012) through physical processes in the atmosphere is: $P_{\text{geo, a}} = 6070\,\text{TW}$. Additionally, $P_{\text{geo, b}} = 40\,\text{TW}$ from the Earth's interior and $P_{\text{bio}} = 215\,\text{TW}$ of chemical free energy from photosynthesis are generated. This free energy is then used to drive the atmospheric circulation, convection, wind, waves and the hydrological cycle (for $P_{\text{geo, a}}$), the mantle convection and plate tectonics (for $P_{\text{geo, b}}$) and the metabolism of organisms (for P_{bio}). Thus, most of the free energy is involved in a dissipative process. In fact, the main portion of 'unused' free energy and, therefore, energy available for human appropriation comes from the biotic activity. The human activity requires already a large part of this available free energy. To better capture this free energy consumption, Kleidon suggests the human appropriation of free energy as a suitable metric for human activity.

---

[2] The Maximum Power Principle is related to the Maximum Entropy Principle, i.e. that complex systems maximise the entropy production in steady state.

Bibliography

Andrews, K. (2013). “Ask an expert: Is coal still being formed today?” `http://www.abc.net.au/science/articles/2013/02/18/3691317.htm`. (Visited on 09/05/2018).

Arrow, K. et al. (1996). “Economic growth, carrying capacity, and the environment”. In: *Environment and Development Economics*. ISSN: 14694395. DOI: `10.1017/S1355770X00000413`.

Atkins, P. (2010). *The Laws of Thermodynamics. A Very Short Introduction.* Oxford: Oxford University Press. ISBN: 9780199572199.

Berg, M., B. Hartley, and O. Richters (2015). “A stock-flow consistent input-output model with applications to energy price shocks, interest rates, and heat emissions”. In: *New Journal of Physics* 17. ISSN: 13672630. DOI: `10.1088/1367-2630/17/1/015011`.

BP p.l.c (2016). “BP Statistical Review of World Energy 2016”. `https://www.bp.com/content/dam/bp/pdf/energy-economics/statistical-review-2016/bp-statistical-review-of-world-energy-2016-full-report.pdf`. (Visited on 09/05/2018).

Buckley, M. W. and J. Marshall (2016). “Observations, inferences, and mechanisms of the Atlantic Meridional Overturning Circulation: A review”. In: ISSN: 19449208. DOI: `10.1002/2015RG000493`.

Budyko, M. I. (1969). “The effect of solar radiation variations on the climate of the Earth”. In: *Tellus* 21.5, pp. 611–619. ISSN: 0040-2826. DOI: `10.3402/tellusa.v21i5.10109`. URL: `https://www.tandfonline.com/doi/full/10.3402/tellusa.v21i5.10109`.

Caesar, L. et al. (2018). “Observed fingerprint of a weakening Atlantic Ocean overturning circulation”. In: *Nature*. ISSN: 14764687. DOI: `10.1038/s41586-018-0006-5`. arXiv: `NIHMS150003`.

Caldeira, K. and J. F. Kasting (1992). “Susceptibility of the early Earth to irreversible glaciation caused by carbon dioxide clouds”. In: *Nature* 359.6392, pp. 226–228. URL: `http://dx.doi.org/10.1038/359226a0`.

Chaisson, E. J. (2008). “Long-term global heating from energy usage”. In: *Eos* 89.28, pp. 253–254. ISSN: 00963941. DOI: `10.1029/2008EO280001`.

Chen, B. et al. (2016). “Exploring the possible effect of anthropogenic heat release due to global energy consumption upon global climate: a climate model study”. In: *International Journal of Climatology* 36.15, pp. 4790–4796. ISSN: 10970088. DOI: `10.1002/joc.4669`.

Crowley, T. J. (2000). “Causes of Climate Change Over the Past 1000 Years”. In: *Science* 289.5477, pp. 270–277. ISSN: 00368075. DOI: `10.1126/science.289.5477.270`. URL: `http://www.sciencemag.org/cgi/doi/10.1126/science.289.5477.270`.

Crutzen, P. J. (2002). “Geology of mankind”. In: ISSN: 00280836. DOI: `10.1038/415023a`.

Crutzen, P. J. (2004). “New Directions: The growing urban heat and pollution ”island” effect - Impact on chemistry and climate”. In: 38.21, pp. 3539–3540. ISSN: 13522310. DOI: `10.1016/j.atmosenv.2004.03.032`. arXiv: `arXiv:1011.1669v3`.

Davies, J. H. and D. R. Davies (2010). “Earth’s surface heat flux”. In: *Solid Earth.* ISSN: 18699529. DOI: `10.5194/se-1-5-2010`.

Dickinson, R. E. et al. (1986). “Biopshere-Atmosphere Transfer Scheme (BATS) for the NCAR Community Climate Model”. In: *NCAR Technical Note* National Center for Atmospheric Research, Boulder, Colorado.

Digiconomist (2018). “Bitcoin Energy Consumption Index”. `https://digiconomist.net/bitcoin-energy-consumption`. (Visited on 09/01/2018).

Donohoe, A. and D. S. Battisti (2011). “Atmospheric and surface contributions to planetary albedo”. In: *Journal of Climate* 24.16, pp. 4402–4418. ISSN: 08948755. DOI: `10.1175/2011JCLI3946.1`.

Feulner, G. (2011). “Are the most recent estimates for Maunder Minimum solar irradiance in agreement with temperature reconstructions?” In: *Geophysical Research Letters* 38.16. ISSN: 00948276. DOI: `10.1029/2011GL048529`.

Fichefet, T. and M. A. Maqueda (1997). “Sensitivity of a global sea ice model to the treatment of ice thermodynamics and dynamics”. In: *Journal of Geophysical Research: Oceans* 102.C6, pp. 12609–12646. ISSN: 21699291. DOI: `10.1029/97JC00480`.

Flanner, M. G. (2009). “Integrating anthropogenic heat flux with global climate models”. In: *Geophysical Research Letters* 36.2, pp. 1–5. ISSN: 00948276. DOI: `10.1029/2008GL036465`.

Fraunhofer ISE (2013). “World Record Solar Cell with 44.7% Efficiency”. `https://www.ise.fraunhofer.de/en/press-media/press-releases/2013/world-record-solar-cell-with-44-7-efficiency.html`. (Visited on 08/26/2018).

Garrett, T. J. (2012). “Modes of growth in dynamic systems”. In: *Proceedings of the Royal Society A: Mathematical, Physical and Engineering Sciences* 468.5, pp. 2532–2549. ISSN: 1364-5021. DOI: `10.1098/rspa.2012.0039`. arXiv: `arXiv:1202.0564v1`.

Garrett, T. J. (2014). “Long-run evolution of the global economy: 1. Physical basis”. In: *Earth’s Future* 2.3, pp. 127–151. ISSN: 23284277. DOI: `10.1002/2013EF000171`. URL: `http://doi.wiley.com/10.1002/2013EF000171`.

Holland, M. M., C. M. Bitz, and B. Tremblay (2006). “Future abrupt reductions in the summer Arctic sea ice”. In: *Geophysical Research Letters* 33.23. ISSN: 00948276. DOI: `10.1029/2006GL028024`.

Houghton, J. T., G. J. Jenkins, and J. J. Ephraums (1990). “Climate Change The IPCC Scientific Assessment”. In: 1.1, p. 414. ISSN: 1040-8703. DOI: `10.1097/MOP.0b013e3283444c89`.

International Energy Agency (2008). “Energy Efficiency Indicators for Public Electricity Production from Fossil Fuels”. `https://www.iea.org/publications/freepublications/publication/En_Efficiency_Indicators.pdf`. (Visited on 09/05/2018).

International Energy Agency (2014). “Key World Energy Statistics 2014. Energy use (kg of oil equivalent per capita) (EG.USE.PCAP.KG.OE) [Data file]”. `http://databank.worldbank.org/data/reports.aspx?source=2&series=EG.USE.PCAP.KG.OE&country=EAS`. (Visited on 09/05/2018).

IPCC (2013). “Summary for Policymakers”. In: *Climate Change 2013: The Physical Science Basis. Contribution of Working Group I to the Fifth Assessment Report of the Intergovernmental Panel on Climate Change.* Ed. by T. Stocker et al. Cambridge, United Kingdom and New York, NY, USA: Cambridge University Press. Chap. SPM, 1–30. ISBN: ISBN 978-1-107-66182-0. DOI: `10.1017/CBO9781107415324.004`. URL: `www.climatechange2013.org`.

Jacobson, M. Z. and M. A. Delucchi (2011). “Providing all global energy with wind, water, and solar power, Part I: Technologies, energy resources, quantities and areas of infrastructure, and materials”. In: *Energy Policy* 39.3, pp. 1154–1169. ISSN: 03014215. DOI: `10.1016/j.enpol.2010.11.040`. URL: `http://dx.doi.org/10.1016/j.enpol.2010.11.040`.

Jakob, M. and J. Hilaire (2015). “Unburnable fossil-fuel reserves”. In: *Nature*. ISSN: 14764687. DOI: `10.1038/517150a`.

Jakob, M. and R. Marschinski (2012). “Interpreting trade-related CO2 emission transfers”. In: *Nature Climate Change*. ISSN: 1758-678X. DOI: `10.1038/nclimate1630`.

Kleidon, A. (2012). “How does the Earth system generate and maintain thermodynamic disequilibrium and what does it imply for the future of the planet?” In: *Philosophical Transactions of the Royal Society A: Mathematical, Physical and Engineering Sciences* 370.1962, pp. 1012–1040. ISSN: 1364-503X. DOI: `10.1098/rsta.2011.0316`. arXiv: `1103.2014`. URL: `http://rsta.royalsocietypublishing.org/cgi/doi/10.1098/rsta.2011.0316`.

Kopp, G. and J. L. Lean (2011). “A new, lower value of total solar irradiance: Evidence and climate significance”. In: *Geophysical Research Letters*. ISSN: 00948276. DOI: `10.1029/2010GL045777`.

Kriegler, E. et al. (2017). “Fossil-fueled development (SSP5): An energy and resource intensive scenario for the 21st century”. In: *Global Environmental Change* 42, pp. 297–315. ISSN: 09593780. DOI: `10.1016/j.gloenvcha.2016.05.015`.

Ladanai, S. and J. Vinterbäck (2009). “Global Potential of Sustainable Biomass for Energy”. In: *SLU, Institutionen för energi och teknik Swedish University of Agricultural Sciences , Department of Energy and Technology*, p. 32. ISSN: 1654-9406. DOI: `ISSN1654-9406`.

Lenton, T. M. et al. (2008). “Tipping elements in the Earth’s climate system”. In: *Proceedings of the National Academy of Sciences*. ISSN: 0027-8424. DOI: `10.1073/pnas.0705414105`.

Lindsay, R. W. and J. Zhang (2005). “The thinning of Arctic sea ice, 1988-2003: Have we passed a tipping point?” In: *Journal of Climate* 18.22, pp. 4879–4894. ISSN: 08948755. DOI: `10.1175/JCLI3587.1`.

Marvel, K., B. Kravitz, and K. Caldeira (2013). “Geophysical limits to global wind power”. In: *Nature Clim. Change* 3.2, pp. 118–121. ISSN: 1758-678X. URL: `http://dx.doi.org/10.1038/nclimate1683`.

Matthes, K. et al. (2017). “Solar forcing for CMIP6 (v3.2)”. In: *Geoscientific Model Development* 10.6, pp. 2247–2302. DOI: `10.5194/gmd-10-2247-2017`. URL: `https://www.geosci-model-dev.net/10/2247/2017/`.

Mcguffie, K. and A. Henderson-Sellers (2014). *The Climate Modelling Primer*. 4th ed. ISBN: 978-1-119-94336-5.

Medhaug, I. and T. Furevik (2011). “North Atlantic 20th century multidecadal variability in coupled climate models: Sea surface temperature and ocean overturning circulation”. In: *Ocean Science*. ISSN: 18120784. DOI: `10.5194/os-7-389-2011`.

Mengel, M. et al. (2012). “Enhanced Atlantic subpolar gyre variability through baroclinic threshold in a coarse resolution model”. In: *Earth System Dynamics*. ISSN: 21904979. DOI: `10.5194/esd-3-189-2012`.

Miller, L. M., F. Gans, and A. Kleidon (2011). “Jet stream wind power as a renewable energy resource: Little power, big impacts”. In: *Earth System Dynamics* 2.2, pp. 201–212. ISSN: 21904979. DOI: `10.5194/esd-2-201-2011`.

Montoya, M. et al. (2005). “The earth system model of intermediate complexity CLIMBER-3α. Part I: Description and performance for present-day conditions”. In: *Climate Dynamics* 25.2-3, pp. 237–263. ISSN: 09307575. DOI: `10.1007/s00382-005-0044-1`.

Müller-Hansen, F. et al. (2017). “Towards representing human behavior and decision making in Earth system models – an overview of techniques and approaches”. In: *Earth System Dynamics* 8.4, pp. 977–1007. DOI: `10.5194/esd-8-977-2017`. URL: `https://www.earth-syst-dynam.net/8/977/2017/`.

Myhre, G. et al. (1998). “New estimates of radiative forcing due to well mixed greenhouse gases”. In: *Geophysical Research Letters* 25.14, pp. 2715–2718. ISSN: 00948276. DOI: `10.1029/98GL01908`.

NOAA Earth System Research Laboratoy (Physical Science Devision) (2011a). "NCEP-NCAR Reanalysis 1. Monthly 'ltm skt.sfc' 1981-2010 from the NCEP Reanalysis [Data File]". `http://www.esrl.noaa.gov/psd/data/gridded/data.ncep.reanalysis.derived.html`. (Visited on 09/05/2018).

NOAA Earth System Research Laboratoy (Physical Science Devision) (2011b). "NCEP-NCAR Reanalysis 1. Monthly 'ltm ulwrf.ntat' 1981-2010 from the NCEP Reanalysis [Data File]". `http://www.esrl.noaa.gov/psd/data/gridded/data.ncep.reanalysis.derived.html`. (Visited on 09/05/2018).

NOAA Earth System Research Laboratoy (Physical Science Devision) (2017). "NCEP/DOE AMIP-II Reanalysis (Reanalysis-2) Daily Averages. Skin Temperature, Daily Mean, Surface, 1979-2017 [Data file]". `https://www.esrl.noaa.gov/psd/cgi-bin/db_search/DBSearch.pl?&Dataset=NCEP/DOE+AMIP-II+Reanalysis+(Reanalysis-2)+Daily+Averages&Variable=Skin+Temperature`. (Visited on 09/05/2018).

North, G. R. (1975). "Analytical Solution to a Simple Climate Model with Diffusive Heat Transport". In: 32.7, pp. 1301–1307. ISSN: 0022-4928. DOI: `10.1175/1520-0469(1975)032<1301:ASTASC>2.0.CO;2`.

North, G. R. (1984). "The Small Ice Cap Instability in Diffusive Climate Models". In: *Journal of the Atmospheric Sciences* 41.23, pp. 3390–3395. ISSN: 0022-4928. DOI: `10.1175/1520-0469(1984)041<3390:TSICII>2.0.CO;2`.

NSIDC (2018). *All About Sea Ice: Salinity and Brine.* URL: `https://nsidc.org/cryosphere/seaice/characteristics/brine_salinity.html` (visited on 05/31/2018).

OECD Nuclear Energy Agency and International Atomic Energy Agency (2016). "Uranium 2016: Resources, Production and Demand". `https://www.oecd-nea.org/ndd/pubs/2016/7301-uranium-2016.pdf`. Chapter 2, conclusion, page 124. (Visited on 09/05/2018).

Pacanowski, R. C. and S. M. Griffies (1999). *The MOM3 Manual.* Tech. rep. 4. Princeton, NJ: NOAA/-Geophysical Fluid Dynamics Laboratory, 680 pp.

Peters, G. P. et al. (2011). "Growth in emission transfers via international trade from 1990 to 2008". In: *Proceedings of the National Academy of Sciences.* ISSN: 0027-8424. DOI: `10.1073/pnas.1006388108`. arXiv: `arXiv:1604.05974v2`.

Petoukhov, V. et al. (2000). "CLIMBER-2: A climate system model of intermediate complexity. Part I: Model description and performance for present climate". In: *Climate Dynamics* 16.1, pp. 1–17. ISSN: 14320894. DOI: `10.1007/PL00007919`.

Pierrehumbert, R. T. (2010). *Principles of Planetary Climate.* Cambridge, UK: Cambridge University Press. ISBN: 9780521865562.

Press, W. H. et al. (2007). *Numerical Recipes 3rd Edition: The Art of Scientific Computing.* 3rd ed. New York, NY, USA: Cambridge University Press. Chap. 20.1.1. ISBN: 0521880688, 9780521880688.

Rahmstorf, S. et al. (2015). "Exceptional twentieth-century slowdown in Atlantic Ocean overturning circulation". In: *Nature Climate Change.* ISSN: 17586798. DOI: `10.1038/nclimate2554`.

Rose, B. (2017). "Lecture notes in 'ATM 623: Climate Modeling'". `https://github.com/brian-rose/ClimateModeling_courseware`. (Visited on 08/26/2018).

Salzmann, M. (2017). "The polar amplification asymmetry: role of Antarctic surface height". In: *Earth System Dynamics.* ISSN: 21904987. DOI: `10.5194/esd-8-323-2017`.

Schellnhuber, H. J., S. Rahmstorf, and R. Winkelmann (2016). "Why the right climate target was agreed in Paris". In: 6.7, pp. 649–653. ISSN: 17586798. DOI: `10.1038/nclimate3013`.

Schmidt, G. A. et al. (2012). "Climate forcing reconstructions for use in PMIP simulations of the Last Millennium (v1.1)". In: *Geoscientific Model Development* 5.1, pp. 185–191. ISSN: 1991959X. DOI: `10.5194/gmd-5-185-2012`.

Sellers, W. D. (1969). “A global climatic model based on the energy balance of the earth-atmosphere system”. In: 8.3, pp. 392–400. ISSN: 0021-8952. DOI: `10.1175/1520-0450(1969)008<0392:AGCMBO>2.0.CO;2`.

Serreze, M. C. et al. (2009). “The emergence of surface-based Arctic amplification”. In: *Cryosphere.* ISSN: 19940424. DOI: `10.5194/tc-3-11-2009`.

Shaner, M. R. et al. (2018). “Geophysical constraints on the reliability of solar and wind power in the United States”. In: *Energy & Environmental Science.* ISSN: 1754-5692. DOI: `10.1039/C7EE03029K`.

Smeed, D. A. et al. (2014). “Observed decline of the Atlantic meridional overturning circulation 2004-2012”. In: ISSN: 18120784. DOI: `10.5194/os-10-29-2014`.

Solargis (2016). “Global Solar Atlas. GHI [Data Map]”. `http://globalsolaratlas.info/?c=16.867634,22.5,5&s=22.187405,23.063964`. (Visited on 09/05/2018).

Sorrell, S. et al. (2010). “Global oil depletion: A review of the evidence”. In: *Energy Policy.* ISSN: 03014215. DOI: `10.1016/j.enpol.2010.04.046`.

Steffen, W. et al. (2015). “The trajectory of the anthropocene: The great acceleration”. In: ISSN: 2053020X. DOI: `10.1177/2053019614564785`.

Steffen, W. et al. (2018). “Trajectories of the Earth System in the Anthropocene”. In: *Proceedings of the National Academy of Sciences.* ISSN: 0027-8424. DOI: `10.1073/pnas.1810141115`. arXiv: `arXiv:1408.1149`.

Steinhilber, F., J. Beer, and C. Fröhlich (2009). “Total solar irradiance during the Holocene”. In: *Geophysical Research Letters* 36.19. ISSN: 00948276. DOI: `10.1029/2009GL040142`.

Stroeve, J. C. et al. (2012). “Trends in Arctic sea ice extent from CMIP5, CMIP3 and observations”. In: *Geophysical Research Letters* 39.16. ISSN: 00948276. DOI: `10.1029/2012GL052676`.

The World Bank (2018). “World Development Indicators. total Population [Data File]”. `http://databank.worldbank.org/data/reports.aspx?source=2&series=SP.POP.TOTL`. (Visited on 09/05/2018).

U.S. Energy Information Administration (2017). “Electric Power Annual 2016”. `https://www.eia.gov/electricity/annual/pdf/epa.pdf`. (Visited on 09/05/2018).

Vatopoulos, K. et al. (2012). “Study on the state of play of energy efficiency of heat and electricity production technologies”. `https://setis.ec.europa.eu/related-jrc-activities/jrc-setis-reports/study-state-of-play-of-energy-efficiency-of-heat-and`. (Visited on 09/05/2018).

Vuuren, D. P. van and T. R. Carter (2014). “Climate and socio-economic scenarios for climate change research and assessment: Reconciling the new with the old”. In: *Climatic Change.* ISSN: 01650009. DOI: `10.1007/s10584-013-0974-2`.

Wilson, D. J. and J. Gea-Banacloche (2012). “Simple model to estimate the contribution of atmospheric CO2 to the Earth’s greenhouse effect”. In: *American Journal of Physics* 80.4, pp. 306–315. ISSN: 0002-9505. DOI: `10.1119/1.3681188`. URL: `http://aapt.scitation.org/doi/10.1119/1.3681188`.

Winkelmann, R. et al. (2015). “Combustion of available fossil fuel resources sufficient to eliminate the Antarctic Ice Sheet”. In: *Science Advances.* ISSN: 23752548. DOI: `10.1126/sciadv.1500589`.

World Nuclear Association (2018). “Nuclear Power Reactors”. `http://www.world-nuclear.org/information-library/nuclear-fuel-cycle/nuclear-power-reactors/nuclear-power-reactors.aspx`. (Visited on 09/05/2018).

Würfel, P. (2002). “Thermodynamic limitations to solar energy conversion”. In: *Physica E: Low-Dimensional Systems and Nanostructures.* Vol. 14. 1-2, pp. 18–26. ISBN: 1386-9477. DOI: `10.1016/S1386-9477(02)00355-7`.

Yang, W. et al. (2017). “Data Descriptor: A new global anthropogenic heat estimation based on high-resolution nighttime light data”. In: *Scientific Data.* ISSN: 20524463. DOI: `10.1038/sdata.2017.116`.

Zhang, G. J., M. Cai, and A. Hu (2013). “Energy consumption and the unexplained winter warming over northern Asia and North America”. In: *Nature Climate Change* 3.5, pp. 466–470. ISSN: 1758678X. DOI: `10.1038/nclimate1803`.

Zhang, X. and K. Caldeira (2015). “Time scales and ratios of climate forcing due to thermal versus carbon dioxide emissions from fossil fuels”. In: *Geophysical Research Letters* 42.11, pp. 4548–4555. ISSN: 1944-8007. DOI: `10.1002/2015GL063514`. URL: `http://dx.doi.org/10.1002/2015GL063514`.

Statement of Authorship

I hereby declare and confirm that this thesis is entirely the result of my own original work. Where other sources of information have been used, they have been indicated as such and properly acknowledged. I further declare that this or similar work has not been submitted for credit elsewhere.

Potsdam, 02.10.2018

Steiglechner

Peter Steiglechner

Acknowledgement

I am very grateful for the support of my both supervisors at the Potsdam Institute for Climate Impact Research (PIK): Maria Martin and Georg Feulner. They are responsible for many valuable ideas in this thesis, they reviewed my drafts, summaries or suggestions in numerous occasions and helped extensively to strengthen and enhance the arguments of this thesis. Also, thankfully, PIK provided me with the necessary facilities and tools to successfully pursue this master thesis.

Furthermore, I want to express great thanks to Jan Landwehrs, who spent several hours from working on his own master thesis trying to make my simulations run. I also thank Stefan Petri for his help in the modification of the CLIMBER-3α run. Highly appreciated, Jonas Schneider took the effort to provide me with helpful tips and critical review comments on my final draft.

Throughout my time at PIK, I have spent many enjoyable and insightful hours with the people from the 'copan' group lead by Jonathan Donges and Jobst Heitzig. I am grateful for the opportunity to have been able to take part in many discussions, presentations or workshops about various of the interdisciplinary research aspects. A special thanks is directed to my office colleague, Johannes Kassel, for the discussions not only about our specific fields of research but also politics, philosophy or climate research as well as for the great support throughout the year, in general.

Last but not least, I want to show my gratitude to my parents, who have not only supported me financially throughout my life but also provided me with extensive education both at home and throughout my academic career and supported, guided and criticised my decisions as best as possible.